공학박사 학위논문

# Versatile and cost-effective high-resolution patterning of carbon nanotube composite via soft-lithography

## 소프트 리소그래피를 통한 탄소나노튜브 복합체의 다목적 및 저비용의 고해상도 패터닝 방법

2023년 2월

서울대학교 융합과학기술대학원

융합과학부 나노융합전공

주 석 원

# Versatile and cost-effective high-resolution patterning of carbon nanotube composite via soft-lithography

지도 교수 : 송 윤 규

이 논문을 공학박사 학위논문으로 제출함
2022년 11월

서울대학교 융합과학기술대학원
융합과학부 나노융합전공
주 석 원

주석원의 공학박사 학위논문을 인준함
2023년 1월

위 원 장 _____ 이 재 규 _____ (인)

부위원장 _____ 송 윤 규 _____ (인)

위 원 _____ 박 원 철 _____ (인)

위 원 _____ 이 강 원 _____ (인)

위 원 _____ 김 주 형 _____ (인)

# Abstract

# Versatile and cost-effective high-resolution patterning of carbon nanotube composite via soft-lithography

Seokwon Joo

Program in Nano Science and Technology

Graduate School of Convergence Science & Technology

Seoul National University

Carbon nanotube (CNT) is a promising electronic material with superior properties such as high electrical conductance, mechanical strength, and environmental friendliness. Accordingly, studies for commercialization are being actively conducted for applying CNTs to various practical fields. Despite these excellent properties and the effort to use them, however, the commercialization of CNTs has been slow, and one of the reasons is the difficulty in patterning them. Numerous methods for patterning CNTs have been developed to overcome the problem, and many studies have been

reported to implement devices using them.

This dissertation deals with developing and applying the CNT patterning method. The developed method not only solves the problems of the conventional methods but also has differentiated advantages. CNT is prepared in composite by mixing with paraffin, an organic material, and patterned via soft-lithography techniques.

Therefore, the first chapter will explain the background of the two materials, CNT and paraffin, and their significance in this study. It also describes soft-lithography and related techniques, the patterning methods used. Moreover, It introduces challenges to be solved simultaneously with the conventional CNT patterning method and presents future directions.

The CNT patterning method and results are presented in detail in the second chapter. The employment of paraffin and soft-lithography offers several advantages in terms of cost and accessibility, as well as process and pattern properties. Significantly, the two most critical advantages are that high-resolution (<10 μm) patterning is possible and printing on various substrates. In addition, optical, electrical, thermal, and mechanical analyses introduce multiple characteristics of CNT composite patterns.

Meanwhile, the remaining CNT residues and paraffin in the pattern can have a negative effect, such as a short circuit. In addition, the transfer process could be difficult on substrates with very low surface energy. Thus, the following chapter discusses these issues and describes additional processes to

improve the quality and properties of the CNT composite pattern.

In the end, a high-performance, flexible, and miniaturized touch sensor and energy harvesting device were fabricated using the printed CNT composite pattern. By utilizing the advantages of high-resolution patterning and no restriction on the substrate, it was possible to manufacture devices with improved performance. It suggests that the CNT composite pattern can be applied to various fields. The fabrication and results of the device will be introduced in the last chapter.

Keywords: CNT/paraffin composite, soft-lithography, microtransfer molding, capacitive touch sensors, energy harvesters, electronic textiles

**Student Number: 2019-39958**

# Contents

# List of figures

# List of tables

# Chapter 1. Introduction

## 1.1. Characteristics of carbon nanotube (CNT)

Carbon nanotubes (CNTs) are cylindrical nanostructures consisting of carbon with a high aspect ratio[1]. It was discovered in 1991 by Iijima[2] and has been studied extensively due to its superior electrical, mechanical, and thermal properties and environmental friendliness[3–5]. For example, the electrical behavior of CNT can be tuned from semiconductor to metallic according to its tube axis (electric current density up to $10^9$ A $cm^{-2}$ in metallic), and it is the strongest material in terms of specific strength. In addition, CNTs can exist in several types depending on the number of walls and axis of the tube. It is called single-walled CNT (SWCNT) when the number of CNT walls is only one, and it is called multi-walled CNT (MWCNT) when there are more than two, as shown in Figure 1.1 (a). The two types have different properties; for example, in electrical properties, MWCNTs are similar to metallic materials, while SWCNTs can have semiconducting and metallic properties[6,7]. Meanwhile, Figure 1.1 (b) shows the chirality along the central axis of the tubes. The chirality of CNTs also significantly affects thermal, electrical, and mechanical properties[8]. Several types of CNTs with different features can be used in various roles in many fields (i.e., conductive additives in batteries[9,10], electrode material for flexible display[11], and materials additives for construction) because they give a wide range of selectivity. In

addition, π interaction is another prominent characteristic of CNTs. π interaction means a non-covalent bond in which two p orbitals form a molecular orbital and bond. A CNT carbon atom makes $sp^2$ bonds with three other carbon atoms, and the electrons of the remaining p orbitals interact with the electrons of the p orbitals of other atoms[12]. Although this π bond enables CNTs to have large electrical conductivity and strong mechanical properties, it also forms van der Waals forces between CNTs. Using the delocalization of electrons by this π interaction, it is also applied to biomedical and biotechnology fields such as drug delivery systems[13].

The primary material of this dissertation is CNT, and the subject is patterning it. The goal is to contribute to the commercialization of CNTs by developing a CNT patterning method that overcomes the existing patterning problems and applying CNT patterns to various fields. To this end, a composite was formed using paraffin as a sub-material and patterned through soft-lithography technology. The next chapter will follow the description of paraffin.

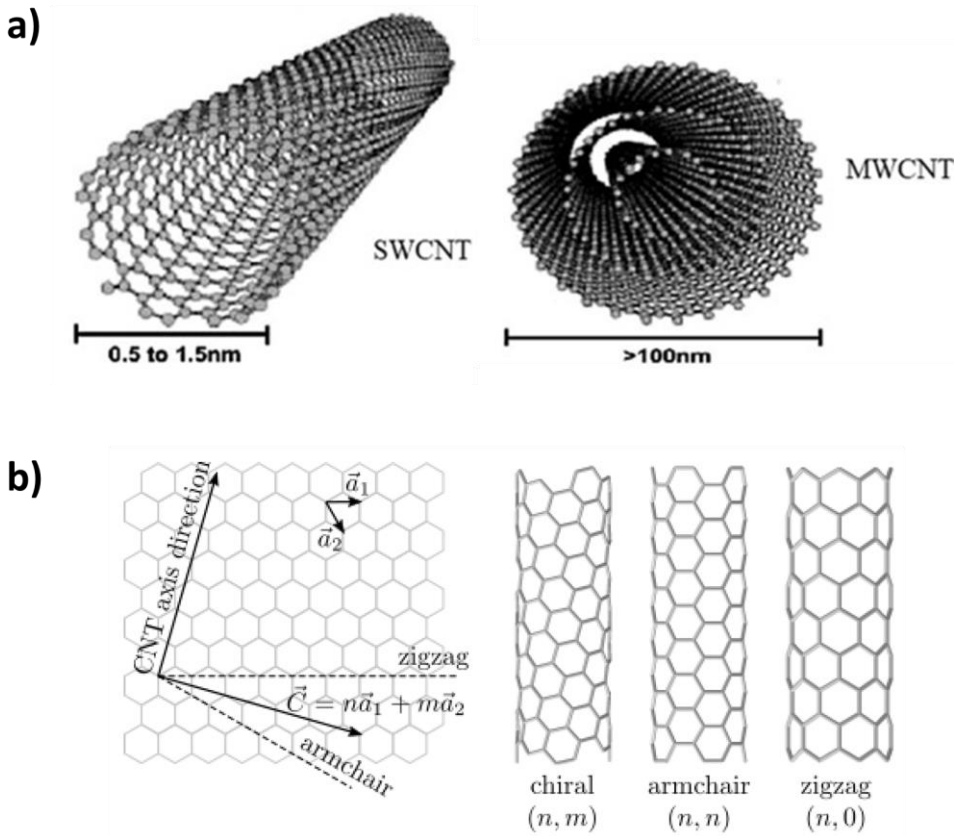


Figure 1.1. Different types of CNT.

(a) Single-walled and multi-walled CNT according to the number of walls. This image was modified from Arun, H et al., International Journal of Electronics and Communications, 2021[7]. (b) Chirality of the CNT according to the tube axis. This image was from Drissi-Habti, M et al., Journal of Composites Science, 2021[8].

## 1.2. Properties of paraffin wax

Paraffin wax is an oligomer with the chemical structure $C_nH_{2n+2}$, white, odorless, and has a low melting point of about 46-68 ℃ depending on the carbon chain length[14]. It is well-known as a phase change material (PCM) and widely applied to the energy storage field due to its high latent heat (168 kJ $kg^{-1}$)[15], so most studies on paraffin are focused on this application. Although paraffin is a promising energy storage material, low thermal conductivity is a challenge to overcome in energy storage applications[16]. PCM composites, which introduce carbon-based materials with high thermal conductivity, are one of the methods to solve this problem[17]. CNTs are preferential candidates due to their large surface area and high thermal conductivity. It has been reported that adding about 2 wt% of MWCNTs can increase the thermal conductivity of paraffin up to 40%[18]. Therefore, there has been much research on the mixture of CNT and paraffin in energy storage.

On the other hand, paraffin was introduced for CNT patterning in this thesis. Paraffin is not only an excellent energy storage material but also can be applied to material patterning because it can be patterned by itself, as shown in Figure 1.2. Many following advantages of paraffin let it suitable for patterning methods, especially in soft-lithography techniques and CNT patterning: (1) inexpensive, harmless[19], and easy to access such that the difficulty of the process can be reduced, (2) low melting point ($T_m$) (53-58 ℃) shortens process time and lowers hurdles, (3) high CNT dispersity compared

to other conventional solvents (i.e., water and NMP) for the solution process, (4) low surface tension (25.1 mJ $m^{-2}$) leading to increase adhesion by conformal contact with the substrate can expand the range of substrate materials, (5) does not swell the stamp unlike organic solvents, (6) phase changing maintains the volume of material in the intaglio space making it easier to implement high thickness.

Paraffin forms a CNT/paraffin composite slurry as a solvent for CNT in a liquid state. After being patterned through soft-lithography, it solidifies and serves as a matrix supporting the CNT core. Paraffin not only makes soft-lithography technology easy to available but also gives pattern and process unique properties that differ from materials used in conventional CNT patterning. The soft-lithography and related techniques will be introduced in next chapter 1.3.

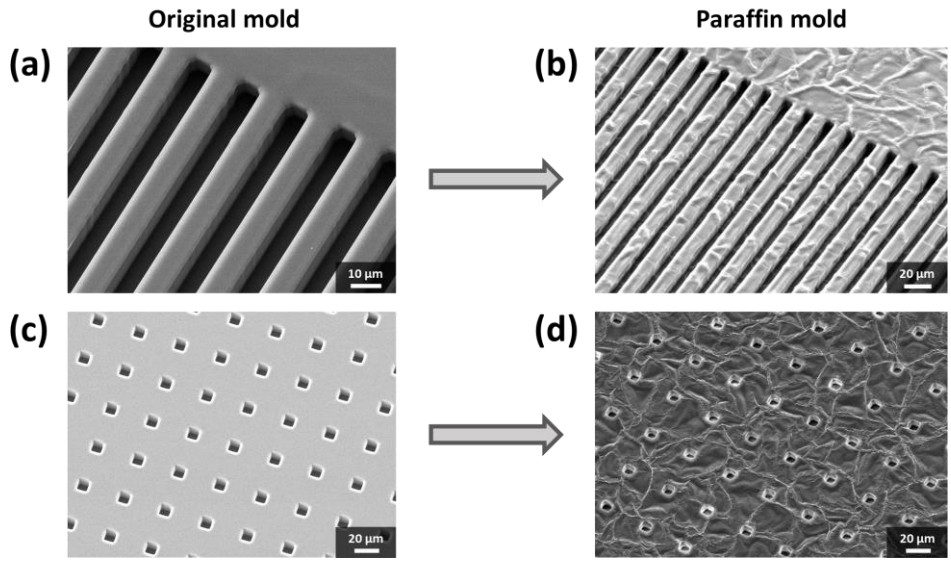


Figure 1.2. Patterning ability of paraffin to replicate micro-patterns through micromolding.

(a,c) SU-8 master mold with 10 μm width line pattern and square pattern. (b,d) Paraffin pattern replicated from the original mold.

## 1.3. Soft-lithography and transfer printing

Soft-lithography is a technology for fabricating structures or patterns, which was introduced by G. M. Whitesides[20]. It uses elastomeric stamps (e.g., poly(dimethylsiloxane) (PDMS)) with a patterned structure on the surface based on printing and molding. Figure 1.3 shows many techniques in soft-lithography, such as microcontact printing (μCP), replica molding (REM), microtransfer molding (μTM), and micromolding in capillaries (MIMIC). Soft-lithography has advantages over conventional photolithography, such as low cost, simple process, enabling the pattern on non-planar surfaces, and using various materials and surface chemistries. Owing to these many advantages, soft-lithography has been studied and applied in copious fields such as micro-electro-mechanical systems (MEMS), sensors, and optics[20].

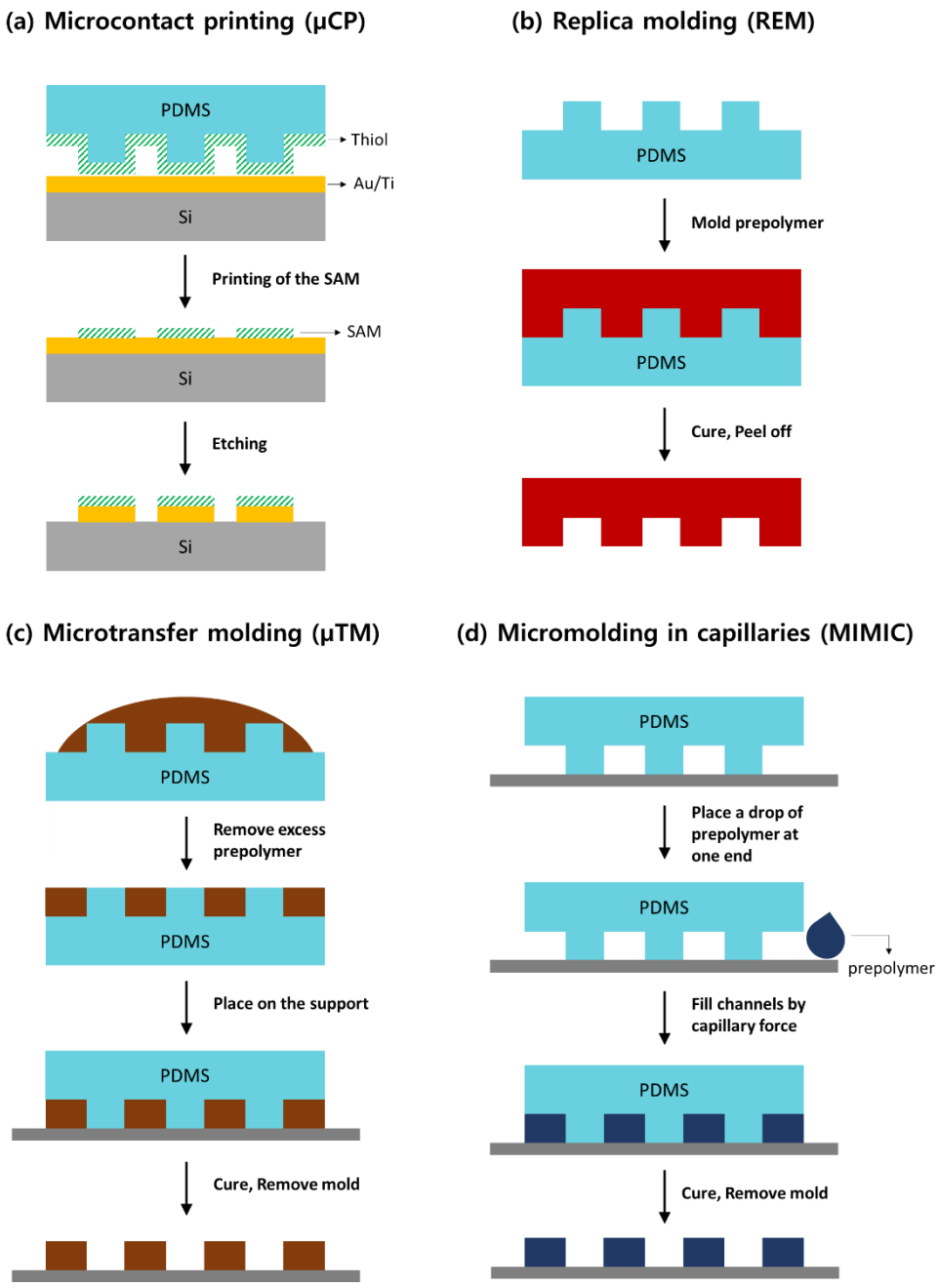


Figure 1.3. Representative methods of soft-lithography.

This image was modified from Y. Xia and G. M. Whitesides et al., *Angewandte Chemie International Edition*, 1998[20].

Among them, μTM of soft-lithography we used is a method of patterning using the negative space of PDMS. Compared to the μCP method, which is the most popular technique in soft-lithography and uses the 2D area of the positive part of the PDMS, it is favorable to control the thickness and shape of the pattern due to the use of 3D space. It would be a double-edged sword, however, because it is challenging to transfer the material filled into the negative space without loss due to the contact area of the inner space. In the case of polymers, they are transferred by the adhesive force generated by curing, but other materials that do not have adhesion require an additional material (e.g., tape)[21] or additional force (e.g., capillary force)[22] to pull out from the intaglio space.

Our study solved this problem by introducing paraffin and transfer skills. The low surface tension of the paraffin causes conformal contact with the substrate, where the solidified paraffin will enhance mechanical anchoring to increase adhesion. In addition, the pattern transfer can be further reinforced by adjusting transfer conditions such as stamp detaching speed or bending radius. Various conditions in the transfer process will be further explained in this chapter, and the detailed procedure (i.e., 'minimize bending radius detachment method') to solve the transfer problem of our study will be described in Chapter 3.2.

The residues on the positive region of the stamp are another chronic problem of the μTM technique. μTM method is inevitably more affected by

residues than μCP that form patterns through the embossing of PDMS stamps. During the transfer of the materials in the negative space of the stamp, the positive parts of the stamp come into contact with the substrate. Then, the materials on the embossing part placed while injecting materials into the intaglio space of the stamp are transferred together. The residues on the substrate distort the pattern and adversely affect the performance of the device made through the pattern. Therefore, studies employing μTM remove residues in various ways (i.e., tape removal[21] and wet-and-drag removal using a blade[23]), as shown in Figure 1.4. However, those methods may remove material in the intaglio or damage the embossed region of the stamp in the process of removing the residue.

Our process also suffered from this residue problem because we used μTM. CNT residues that are not removed from the embossed region of the stamp may transfer together and cause problems such as electrical shorts. This problem could be solved through the 'paraffin cleaning process'. This process uses paraffin drops to wash away the embossed CNTs. It is significant because it does not damage the stamp and uses the same material as the intaglio material. This process removed the CNT residue on the stamp embossing cleanly and will be introduced in detail in Chapter 3.1.

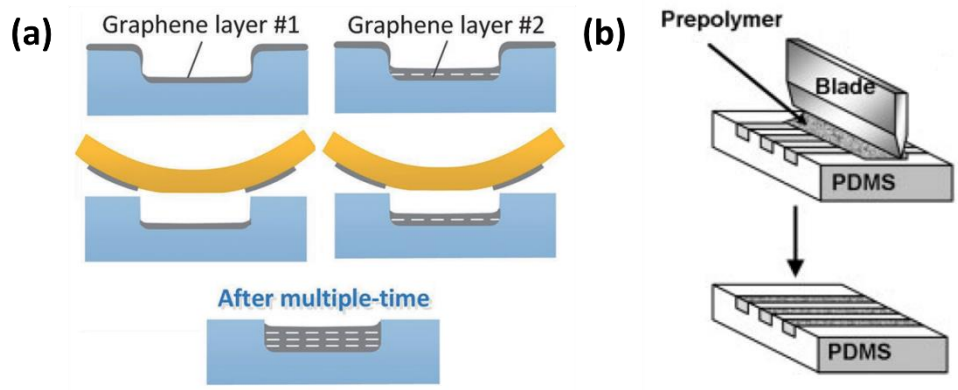


Figure 1.4. Schematics of the methods for removing residues in the μTM. (a) Using tape to remove residues from the embossed surface. This image was from Oren, S et al., *Adv Mater Technol*, 2017[21]. (b) Removing the residue from the embossed regions using a prepolymer and a blade. This image was from Lee, J. H et al., *Journal of the American Oil Chemists' Society*, 2005[23].

Transfer printing is essential for printing materials (e.g., chips, self-assembled monolayers, and polymer films) in processes such as wafer bonding, pick-and-place technology, and soft-lithography[24]. In particular, It is imperative to μTM of soft-lithography because transferring the material in the intaglio space of the stamp to the substrate is essential. Many factors (e.g., peeling speed rate and bending radius of the stamp) are involved in the transfer of material from the transfer stamp (referred to as the donor) to the final substrate (referred to as the receiver).

Figure 1.5 illustrates the transfer printing depending on the peeling speed rate[25]. The peeling speed can determine whether the material adheres to the donor (i.e., pick) or to the receiver (i.e., place). Figure 1.6 (a) shows the effect of the exfoliation rate on energy transfer experimentally[25]. In the experiment, a steel cylinder rolls down an inclined PDMS rubber slab, and gravity separates the steel and PDMS at the rear end of the contact area. The loss of gravitational potential is taken as the adhesion energy hysteresis, $G$, at the measured rolling or separation speed, $v$. The graph in Figure 1.6 (b) describes the relation between $G$ and $v$. It can be shown that $G$ is dependent strongly on the $v$ due to the viscous behavior of PDMS, and the $G$ can be referred to as separation energy[26].

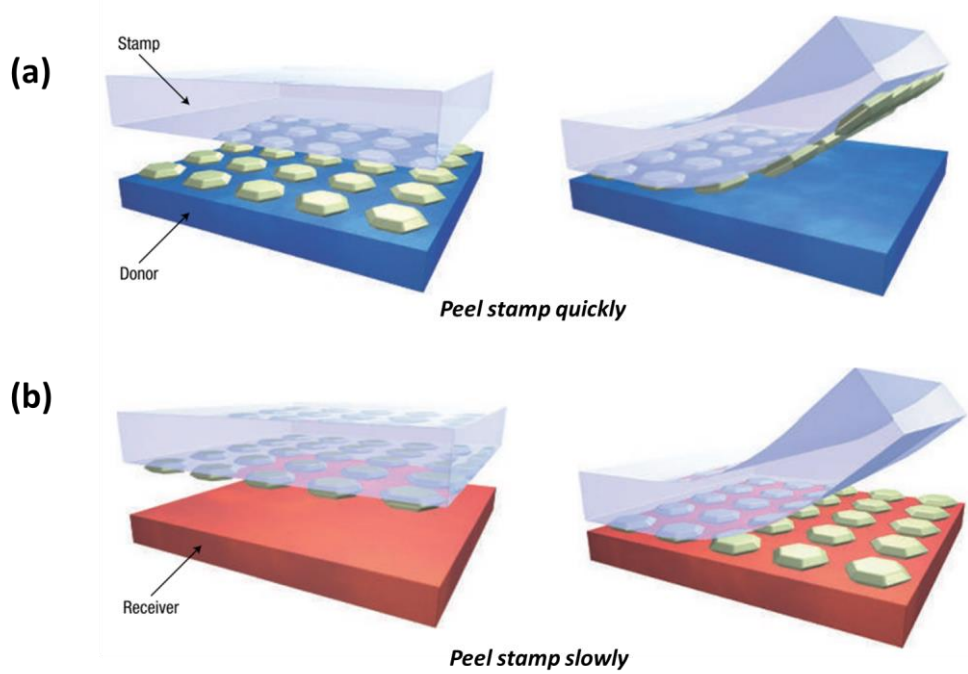


Figure 1.5. Scheme showing transfer printing depending on the peeling speed rate.

This image was modified from Meitl, M. A et al., *Nat Mater*, 2006[25].

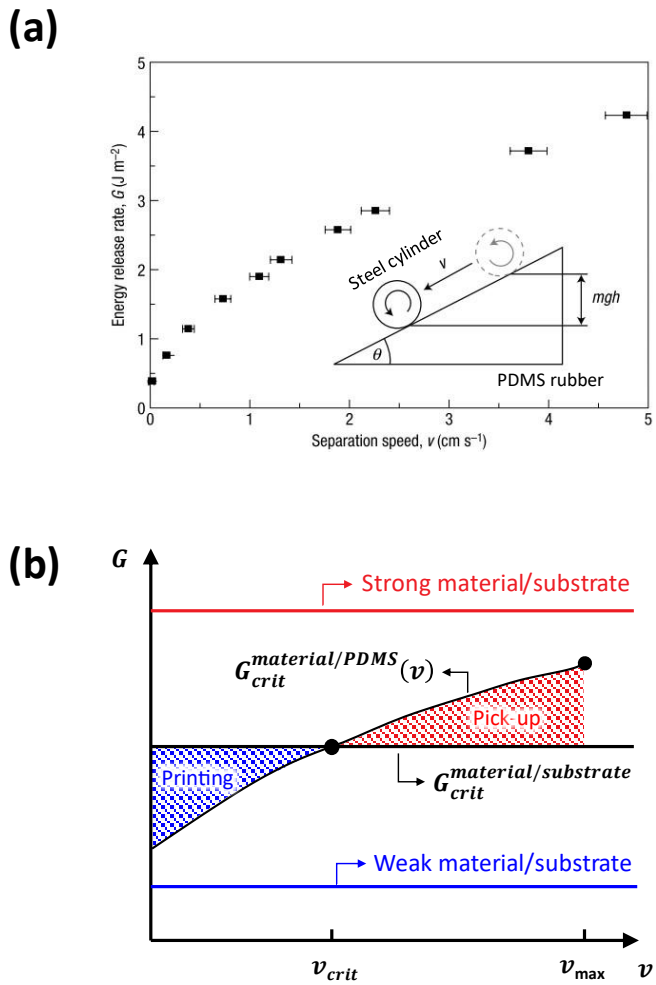


Figure 1.6. The relationship between energy release rate, *G*, and peeling speed rate, *v*.

(a) Experimental scheme showing the energy release rate in terms of the speed of the steel rod going down the PDMS slope. This image was modified from Meitl, M. A et al., *Nat Mater*, 2006[25]. (b) The graph of the relationship between *G* and *v*. This image was modified from Zhang, L et al., *Micromachines*, 2021[27].

Therefore, the relationship between transfer and peeling speed can be summarized in the following equation:

$$G_{PDMS-material}(1 + \emptyset(v)) = G_{receiver-material}$$

where $G_{PDMS-material}$, $G_{receiver-material}$, and $\emptyset$ represent the separation energy between PDMS-material and receiver-material, and the increasing function of $v$, respectively[25]. This equation shows that a lower speed is advantageous for transferring the material from the donor to the receiver. However, in our experiment, the peeling rate was 1-2 cm $s^{-1}$ of high speed, which was one order of magnitude higher than in other studies[28]. The reason for the fast peeling speed is the adhesion between the paraffin and the substrate, i.e., the high $G_{receiver-material}$. High peeling speed is a critical factor that can dramatically increase the speed of the process.

On the other hand, the curvature of the peeling substrate is also essential in the transfer process. Figure 1.7 shows images of the change in adhesive force according to the bending curvature when the peeling process[29]. It can be seen that as the bending curvature of the donor (i.e., PDMS substrate) increases, the area of the peeling zone increases. It means an increase in adhesion between the substance and the donor (i.e., $G_{PDMS-material}$). Therefore, reducing the radius of curvature of the bending during the peeling process can facilitate the transfer.

Despite the increased adhesion due to the mechanical anchoring of paraffin, there may be situations when transfer becomes difficult due to the characteristic of the μTM, which pulls out the material from the intaglio space. For example, when the substrate's surface energy is very low, or the pattern's size is small, the stamp's contact area is very large compared to the contact area with the substrate. By adjusting the conditions in the transfer printing described above to facilitate a transfer, the problem of μTM can be solved more easily.

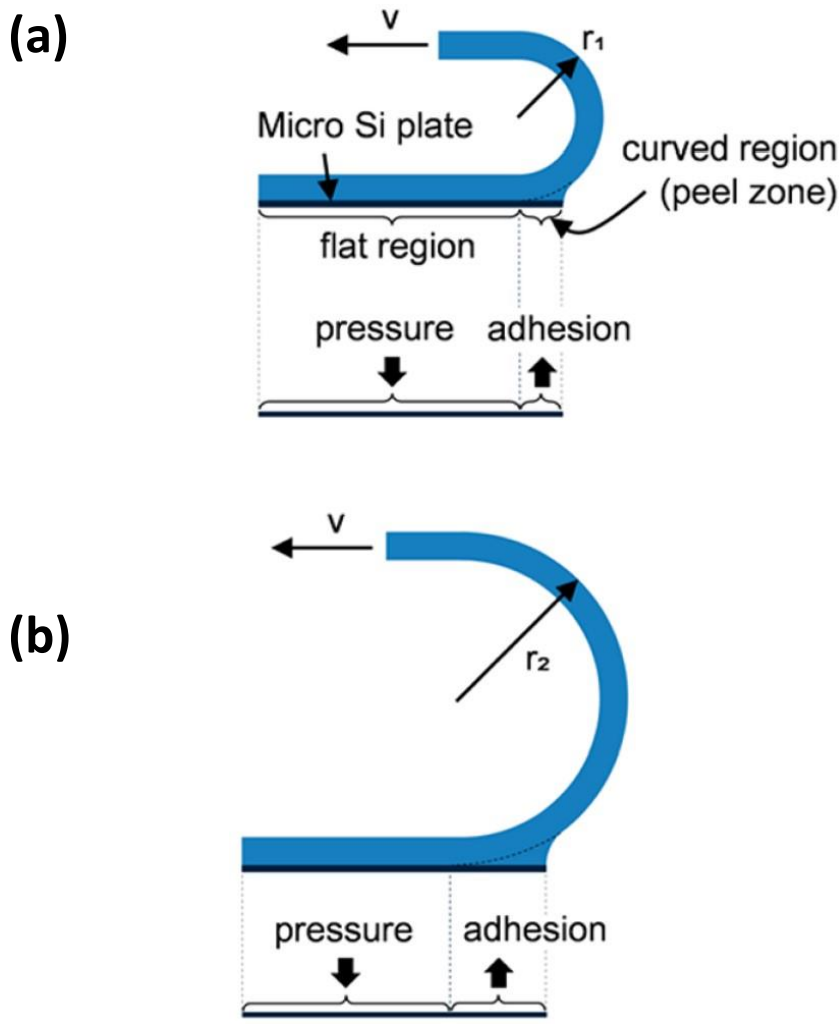


Figure 1.7. Schemes showing the effect of the radius of bending curvature during the transfer process.

This image was from Cho, S et al., *Langmuir*, 2016[29].

## 1.4. Patterning method of CNT

Despite the superior properties of the CNT, there have been many limitations to the practical application of CNTs. Obstacles to commercializing CNTs include production cost, mass and uniform production, and many substitutes. Among them, patterning is one of the representative challenges for CNT commercialization. For CNT to be applied to electronic devices, patterning is required. In the patterning process, the advantages of CNTs maintained in the results, as well as the throughput and cost, should be considered. The conventional CNT patterning method has pros and cons, which will be introduced in this chapter.

The conventional CNT patterning method can be divided into two types, as shown in Figure 1.8. One is pre- or post-growth CNT patterning combined with photolithography, which uses a technique of growing CNTs on transition metals. CNTs are grown on a pre-patterned transition metal through photolithography in pre-growth patterning. On the other hand, in the post-growth method, a CNT thin film is developed on a transition metal, and then the CNT is directly patterned through a photolithography process. Since it is grown directly on the substrate, a high-quality and well-aligned CNT layer can be obtained, and high-resolution patterns can also be achieved using photolithography[30–32]. However, since the chemical vapor deposition (CVD) process for CNT film growth is performed at a high temperature of 500-600 ℃, the type of substrate is limited (i.e., difficult to use a flexible

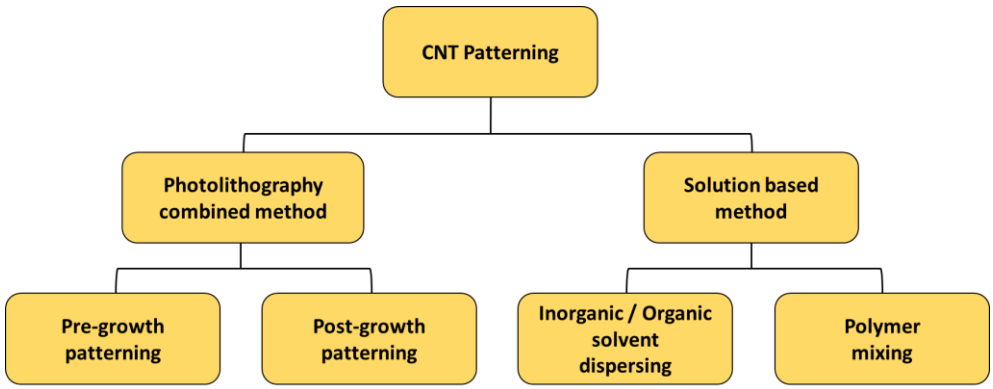


Figure 1.8. Conventional patterning methods of CNTs.

substrate)[33]. In addition, photolithography may have disadvantages, such as cost, time, environmental pollution, and chemical exposure to materials.

Another type of patterning method, dispersing CNT in a solution, and printing in various ways, can overcome these disadvantages. This method uses different printing methods such as inkjet printing[34], spray coating[35,36], and screen printing[37] after dispersing CNT in multiple solvents such as water and 1-methyl-2-pyrrolidinone (NMP), so there is a wide range of choices depending on the situation. These printing techniques are usually advantageous in terms of time and cost compared to methods based on photolithography. In addition, there are no substrate restrictions, such as using a flexible substrate based on a polymer that is weak to heat because it is not exposed to high temperatures as in the CVD process. This method, which has many advantages, also has disadvantages, one of which is that CNTs are difficult to disperse in solution. The strong van der Waals force between CNTs resulting from the strong intermolecular π interaction makes it hard for the CNTs to be dispersed in the solvent[38]. To disperse CNTs well in a solvent, it is necessary for treatment, such as undergoing strong acid[39], ultrasonic treatment for a long time[40], and surface functionalization treatment[41], which is the biggest obstacle to the commercialization of this solution-based method.

A mixture with a polymer instead of a solvent has been reported to overcome this dispersion problem. Since long molecular chains surround CNTs and weaken van der Waals forces between them, they are easier to

disperse CNTs than inorganic or organic solvents[42]. CNT/polymer composites can be patterned more easily by techniques such as inkjet printing and screen printing. It also has a drawback that a decrease in electrical conductivity is unavoidable due to the polymer molecules between the CNT networks[43], and it is usually in a trade-off relationship with the amount of polymer. In addition, a solvent for dissolving polymer can occur the swelling problem of the elastomeric stamp in soft-lithography. However, this method not only overcomes the disadvantages of other patterning methods (i.e., high thermal temperature process and CNT dispersion) but also has the advantage that various properties of the polymer (i.e., electrical conductivity[44], flexibility[45–47], UV curability[48], optical properties[49], etc.) can be imparted to the CNT composite material depending on which polymer is mixed.

Herein, we performed the CNT patterning by mixing CNTs with paraffin and employing soft-lithography. This method solves conventional problems of CNT patterning (i.e., high-temperature process, CNT dispersion, and elastomeric stamp swelling) while allowing it to have several unique characteristics that come from paraffin (e.g., thermal recovery and high thickness pattern). In terms of CNT patterning, CNT/paraffin composites can present a unique vision comparable to CNT/polymer composites.

# Chapter 2. Patterning of CNT/paraffin composite via soft-lithography

## 2.1. Introduction

We prepare a CNT/paraffin composite and pattern it through the μTM method of soft-lithography technology. By introducing paraffin, which exhibits high compatibility with CNTs[50], the CNT composite and the process can have multiple merits. CNTs are more dispersed in paraffin than in other solvents because paraffin oligomer molecules weaken the van der Waals forces between CNTs, as shown in Figure 2.1. In other solvents, CNTs form clusters and then cause massive aggregation. In contrast, in paraffin, clusters spread, which allows the process to be fast and straightforward without pre- or post-treatment (e.g., strong acid treatment or long-time ultrasonication). Also, the low surface tension of paraffin (see Figure 2.2) leads to increase adhesion between the pattern and substrate by conformal contact, which can expand the range of substrate materials.

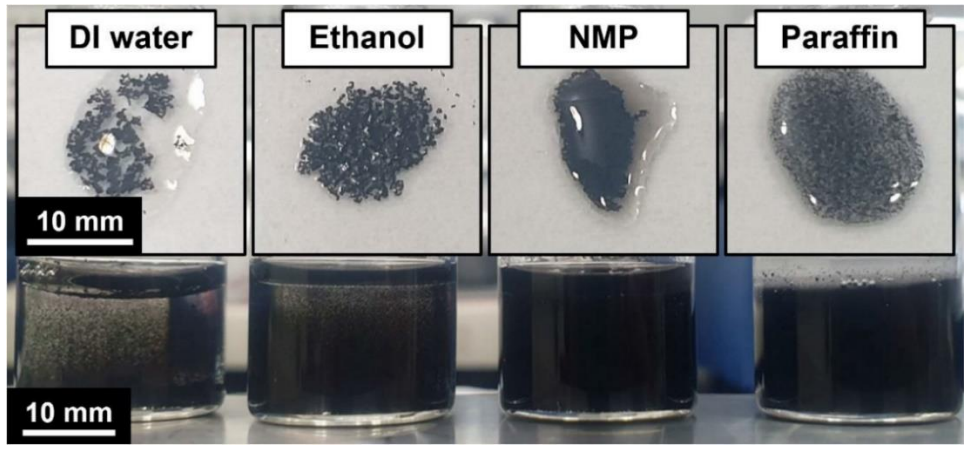


Figure 2.1. Photographs of CNTs dispersed in various solvents without any additives or additional processes.

This image was from S. Joo et al., *Small*, 2022[51]. The reuse permission was not required.

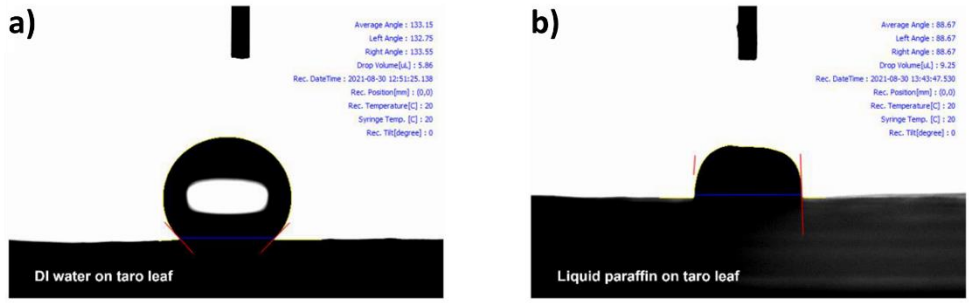


Figure 2.2. Contact angle measurements on taro leaf.

a) DI water and b) liquid paraffin on Colocasia esculenta (taro) leave with a rough surface. The contact angles were measured to be ~133° and ~89° for water and paraffin, respectively. This image was from S. Joo et al., *Small*, 2022[51]. The reuse permission was not required.

## 2.2. Experiments

### 2.2.1. Sample preparation

PDMS (Sylgard 184, DOW) was prepared by mixing a base and a curing agent in a ratio of 10:1. Then, poured the mixture into the preferentially engraved photoresist layer and cured at 60 ℃ for 12 h to replicate the elastic stamp.

The overall processes of the CNT/paraffin composite patterning are illustrated in Figure 2.3. Paraffin wax ($T_m$ 53-58 ℃, Sigma-Aldrich) was initially melted onto the hotplate at 70 ℃ (i.e., higher than the $T_m$ of paraffin, and the higher the temperature, the faster the process), and then multi-walled CNTs (C-Tube 120; average diameter 20 nm; length 20-100 μm, CNT Co., Ltd.) were added 5 wt% of the composite. A slurry of CNT/paraffin composite could be prepared simply by gentle stirring for 30 s with a spatula.

At this time, composites with different CNT mixing ratios were also prepared. However, due to the very low density of CNTs (~2.1 g $cm^{-3}$)[52], the state of the slurry significantly changed as the CNT concentration was changed. For example, a CNT concentration of 4 wt% makes the fluidity of the slurry too high to form CNT blocks in the negative space of the stamp. Thus, the CNTs could not aggregate in the space and came out of the stamp with excessive paraffin. Conversely, at a CNT concentration of 6 wt%, the slurry becomes a clay-like state, and the excess slurry cannot be squeezed out of the stamp. Therefore, 5 wt% of the CNT mixture was most suitable for

patterning due to the characteristics of the μTM process, as shown in Figure 2.4. The negative space is not sufficiently filled with CNT blocks at 4 wt%, and excess CNT residues cover the positive region at 6 wt%. It is of note that, however, CNT and paraffin can be phase-separated easily in this process because CNTs are not mono-dispersed. This means the CNT concentration of the local region could be changed in real-time, leading to the concentration change of the CNT composite pattern, as shown in Chapter 2.3.3.

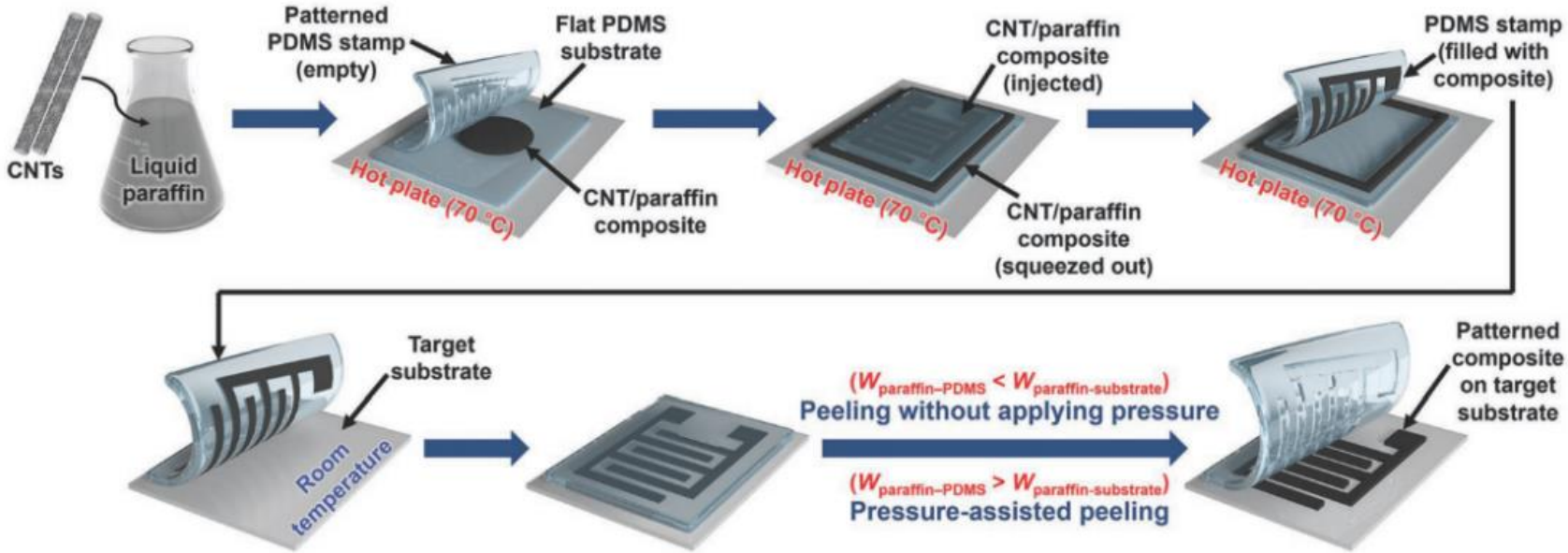


Figure 2.3. Schematic of patterning CNT/paraffin composite via μTM method.

This image was from S. Joo et al., *Small*, 2022[51]. The reuse permission was not required.

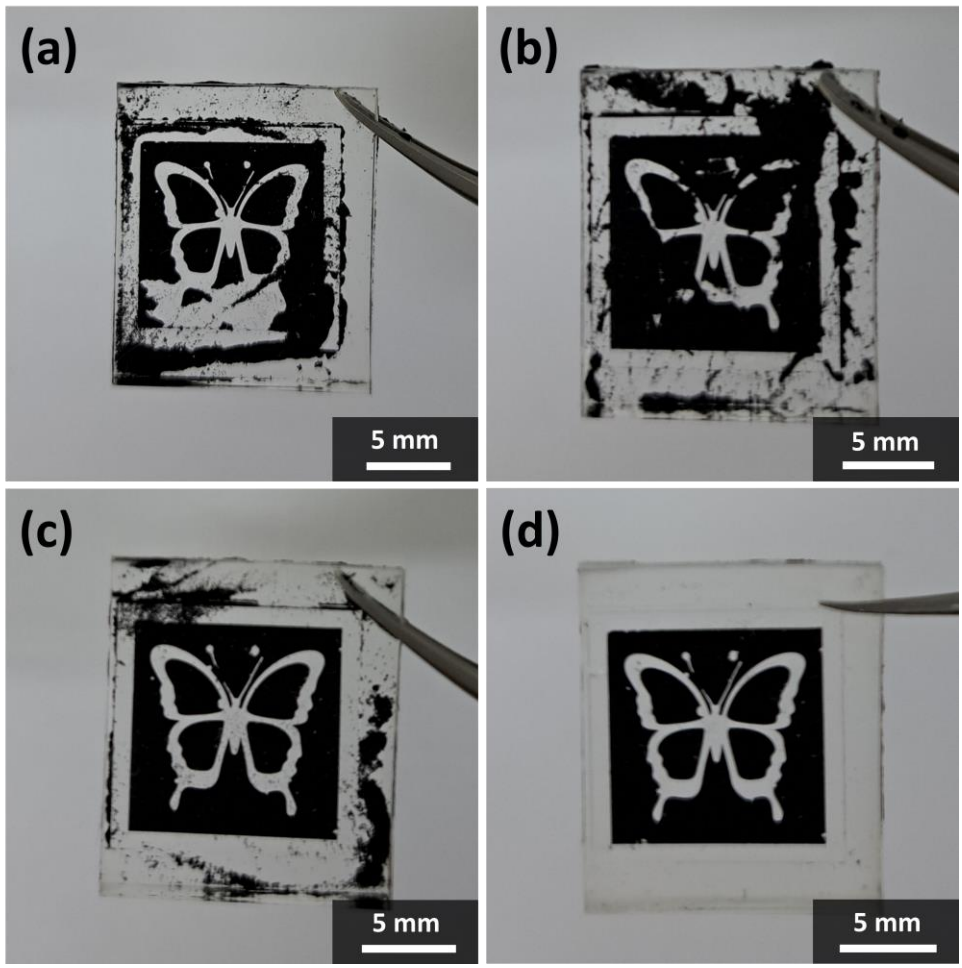


Figure 2.4. The trend of injecting slurry to the negative space of the stamp according to the CNT concentration in the composite.

(a) 4 wt%, (b) 6 wt%, (c) 5 wt% of CNT concentration, and (d) 5 wt% CNT concentration after the paraffin cleaning process.

### 2.2.2. Patterning process of the CNT/paraffin composite

The CNT/paraffin composite slurry was put onto the bare PDMS substrate heated above the $T_m$ of paraffin on a hot plate and then covered the composite slurry with a PDMS stamp. Subsequently, to place the slurry into the intaglio space, press and rub the stamp. Because the surface energy of PDMS (19.8 mJ $m^{-2}$) is lower than that of the paraffin (25.1 mJ $m^{-2}$), only with a weak pressure of the finger, the slurry was filled into the negative space, and excess paraffin was easily squeezed out of the stamp. In this process, CNT in the composite aggregated to form a block in the intaglio space of the stamp. Then the composite slurry-filled PDMS stamp was put onto the desired substrate with maintaining the temperature over the paraffin $T_m$. After that, the slurry-filled PDMS in contact with the substrate was cooled to below the $T_m$ of paraffin by resting at ambient temperature for several seconds to solidify the slurry. In the end, the PDMS stamp was peeled off carefully, and the CNT/paraffin composite pattern was transferred to the substrate.

### 2.2.3. Characterization of the composite

The basis of this patterning method is the formation of the block by aggregation of CNTs in the intaglio space of the PDMS stamp. The basis of this patterning method is the formation of the block by aggregation of CNTs in the intaglio space of the PDMS stamp. At this time, the noteworthy point is that the CNT mixed in paraffin solution is in a state of aggregation because it has not performed any treatment for mono-dispersion, and Figure 2.5 shows an expected model of the aggregated CNT clusters in paraffin. The CNT cluster must be smaller than the pattern width to enter into the negative space of the stamp and form a block, which means that the aggregate size of CNT in paraffin has a decisive influence on the resolution limit of this patterning method. Accordingly, the size of CNT clusters in paraffin solution was confirmed through dynamic light scattering (DLS) (SZ-100V2, HORIBA Scientific) at 65 ℃, as shown in Figure 2.6. The graph shows a Gaussian distribution between about 1 and 10 μm, which can be inferred that the patterning method may have a patterning resolution limit within a few micrometers.

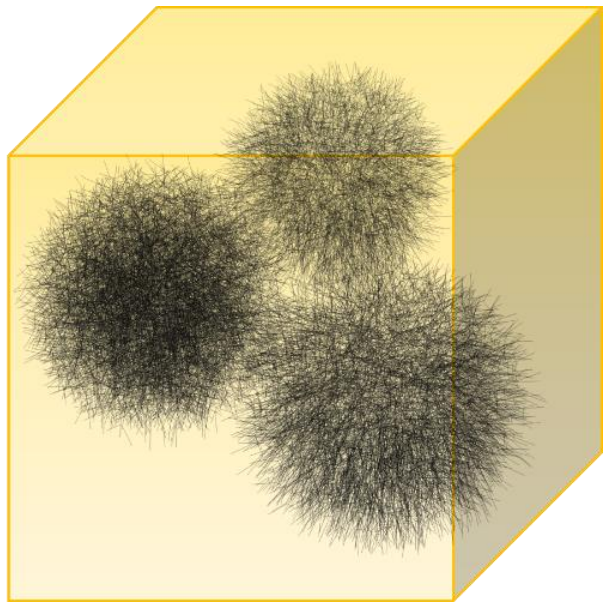

Figure 2.5. An expected model of the CNT clusters aggregated in paraffin solution.

This image was from S. Joo et al., *Small*, 2022[51]. The reuse permission was not required.

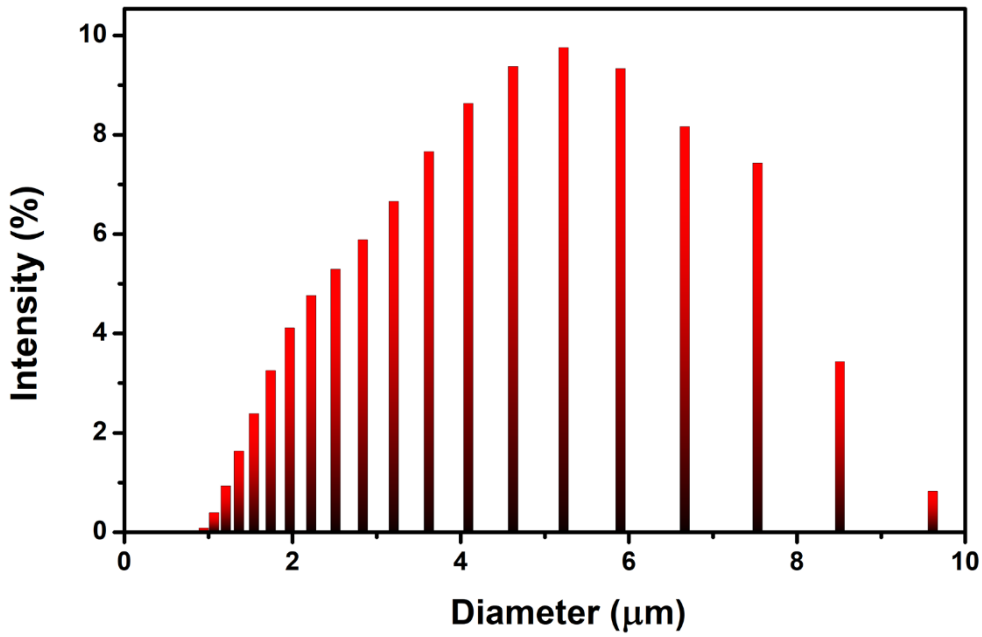


Figure 2.6. DLS analysis showing the diameter of the aggregated CNT clusters in paraffin solution.

This image was from S. Joo et al., *Small*, 2022[51]. The reuse permission was not required.

Meanwhile, differential scanning calorimetry (DSC) (TGA/DSC1, Mettler Toledo) analysis was performed to compare the thermal properties of paraffin and CNT/paraffin composite, as shown in Figure 2.7. Pure paraffin shows the onset of the transition temperature ($T_t$) at 33.7 ℃ and the onset of the $T_m$ at 51.0 ℃. Also, it has -12.01 J $g^{-1}$ of latent heat of the solid-solid transition and -84.46 J $g^{-1}$ of solid-liquid transition. In the case of the CNT/paraffin composite, the onset of the $T_t$ is 33.8 ℃, and the $T_m$ is 49.1 ℃. The latent heat of the composite is -12.12 J $g^{-1}$ in solid-solid transition and -84.42 J $g^{-1}$ in solid-liquid transition. As a result, there are no significant differences in thermal properties between the pure paraffin wax and the CNT/paraffin composite, indicating no chemical reaction between paraffin and CNT[53,54].

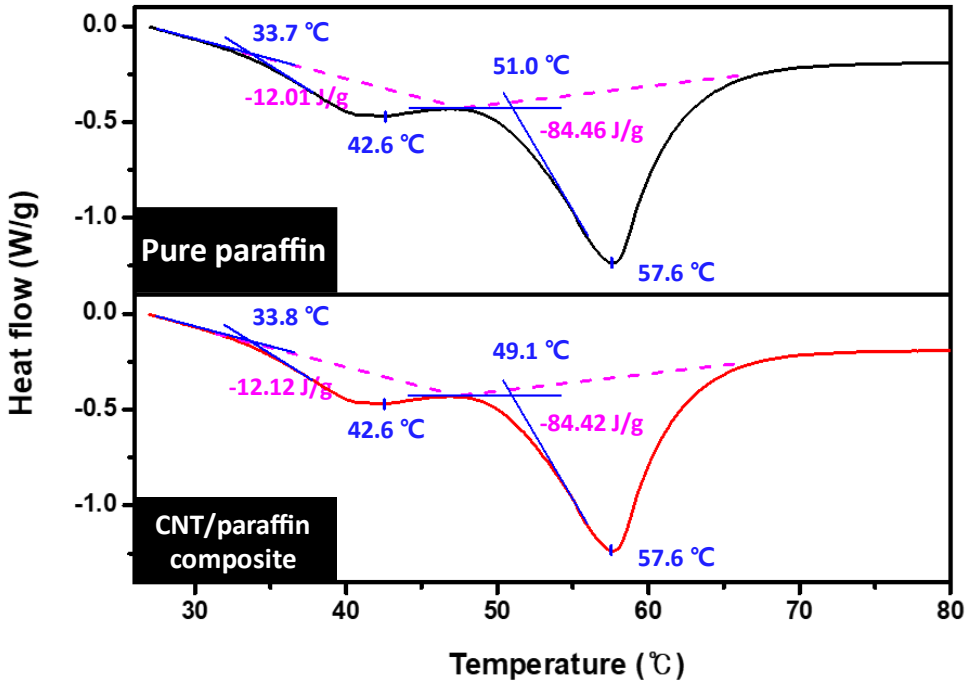


Figure 2.7. DSC data showing the thermal properties of pure paraffin and CNT/paraffin composite.

## 2.3. Results

### 2.3.1. Optical measurements

The optical measurements of the printed CNT composite pattern are introduced in Figure 2.8. Figure 2.8 (a,b) shows the line patterns with widths of 10 and 7 μm and heights of 11 and 5 μm, respectively, measured by optical microscopy. Notably, 7 μm line width is the experimentation resolution limit, similar to the analysis in Chapter 2.2.3. If the pattern width becomes smaller than this, the aggregated CNT clusters cannot enter the inside space of the PDMS stamp, and CNT cluster blocks are not formed.

On the other hand, not only the limit of the minimum size of this process but also the width and height of the large size were measured. Figure 2.8 (c) shows a sufficiently large line pattern with a width and height of 1 mm. These data demonstrate the differentiating advantage of the μTM printing method. Because it is challenging to implement a pattern with a large-scale height in other ways, such as μCP, which uses the embossing part of the stamp. It presents the possibility of controlling the electrical conductivity by adjusting the height of the pattern. Also, Figure 2.8 (d) shows the image of the field-emission scanning electron microscope (SEM) (JSM-7500F, JEOL), indicating that the pattern can be printed with high accuracy and sharpness since the inner space of the stamp was duplicated.

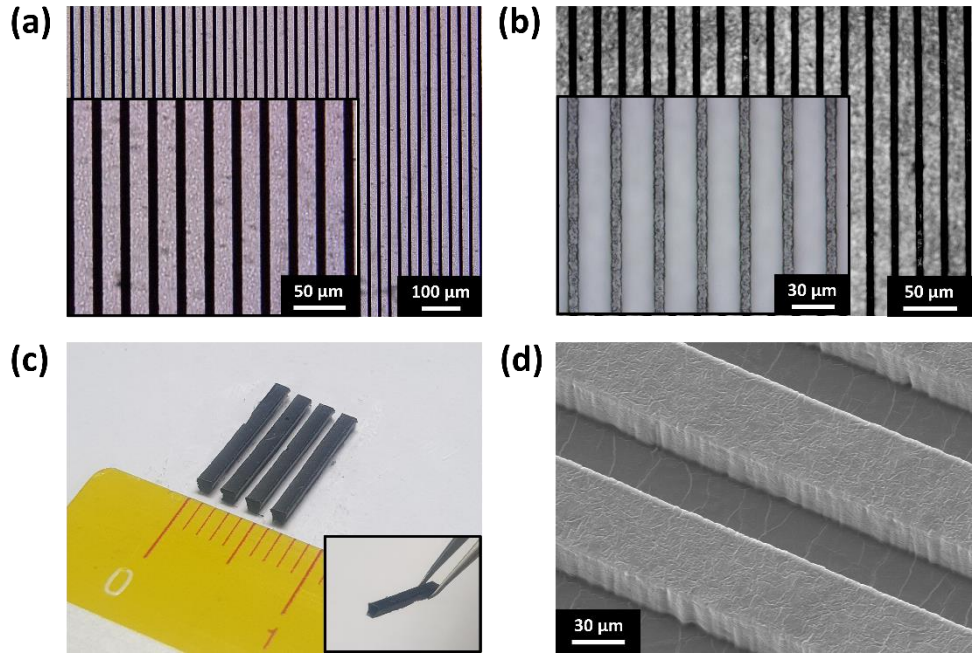


Figure 2.8. Optical measurements of the CNT/paraffin composite printed with line patterns.

(a) 10 µm and (b) 7 µm line width measured by optical microscope, respectively. (c) Photo image of the CNT/paraffin composite line block with 1 mm width and height. (d) SEM image of the 50 µm width line pattern. This image was modified from S. Joo et al., *Small*, 2022[51]. The reuse permission was not required.

Figure 2.9 shows the CNT/paraffin composite printed with various patterns on the different substrates. The μTM method allows high-resolution and sophisticated patterns to be easily printed. Interestingly, patterns can be printed on substrates with high roughness (i.e., paper, leaves, and skin) as well as common substrates (i.e., glass and polyethylene terephthalate (PET)). It results from the low surface tension of paraffin. In a transfer process, the high wettability of the liquid state paraffin makes conformal contact between the printed pattern and substrate after the solidification. This mechanical anchoring facilitates transfer processing by strengthening the adhesive force of the pattern to the substrate. However, it is hard to transfer patterns only with mechanical anchoring to the substrates with very low surface energy, such as perfluoroalkoxyalkane (PFA). In addition, as the pattern size becomes smaller, the adhesive force ratio of the pattern-stamp to the pattern-substrate increases, making transfer difficult. Therefore, on a substrate with low surface energy, especially when the pattern is small, an additional PDMS removal technique was introduced to ensure the quality of the pattern. This peeling technique will be introduced in Chapter 3.2.

Figure 2.10 shows the SEM images of the inside and surface of the CNT pattern. It can be shown that the aggregated CNT clusters with the random networks are surrounded by paraffin, and there are CNTs protruding slightly outside the pattern.

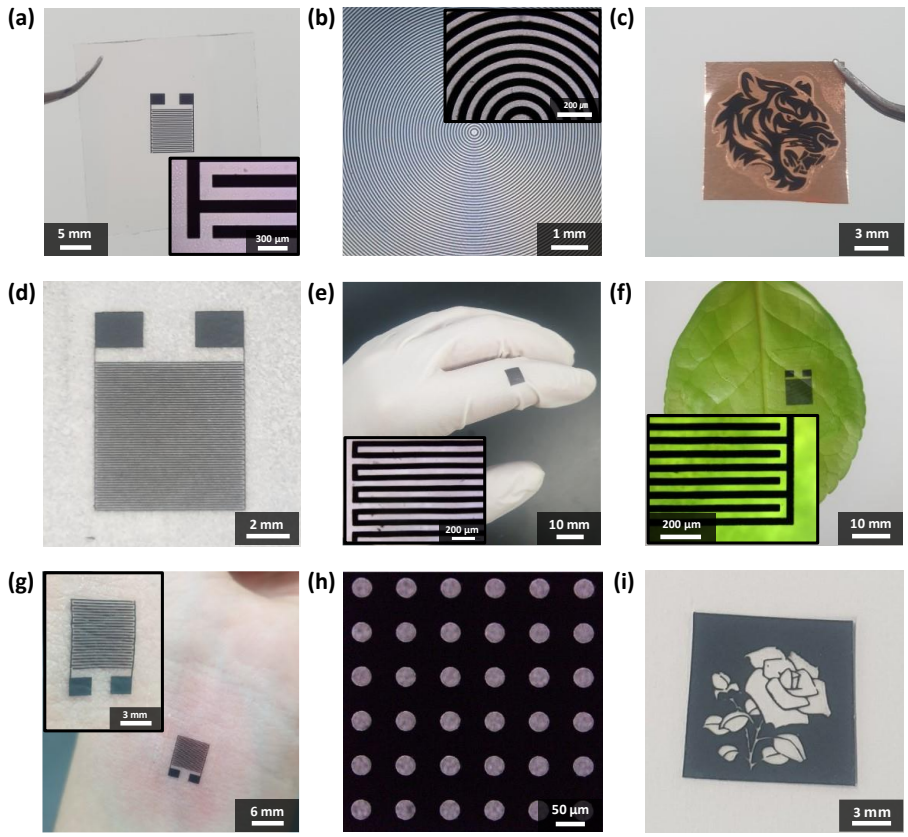


Figure 2.9. Optical measurements of the CNT/paraffin composite printed with a variety of patterns on the various substrates.

(a) Interdigitated pattern with 125 μm width on the glass substrate. (b) Concentric circle pattern with 50 μm width on the PET substrate. (c) The graphic pattern on the copper foil. (d) Interdigitated pattern with 50 μm width on the A4 paper. (e) Serpentine pattern with 50 μm width on the latex glove. (f) Interdigitated pattern with 50 μm width on the leaf. (g) Interdigitated pattern with 125 μm on the human skin. (h) Hole pattern with 35 μm diameter on the PFA film. (i) Graphical pattern on the PET film. This image was modified from S. Joo et al., *Small*, 2022[51]. The reuse permission was not required.

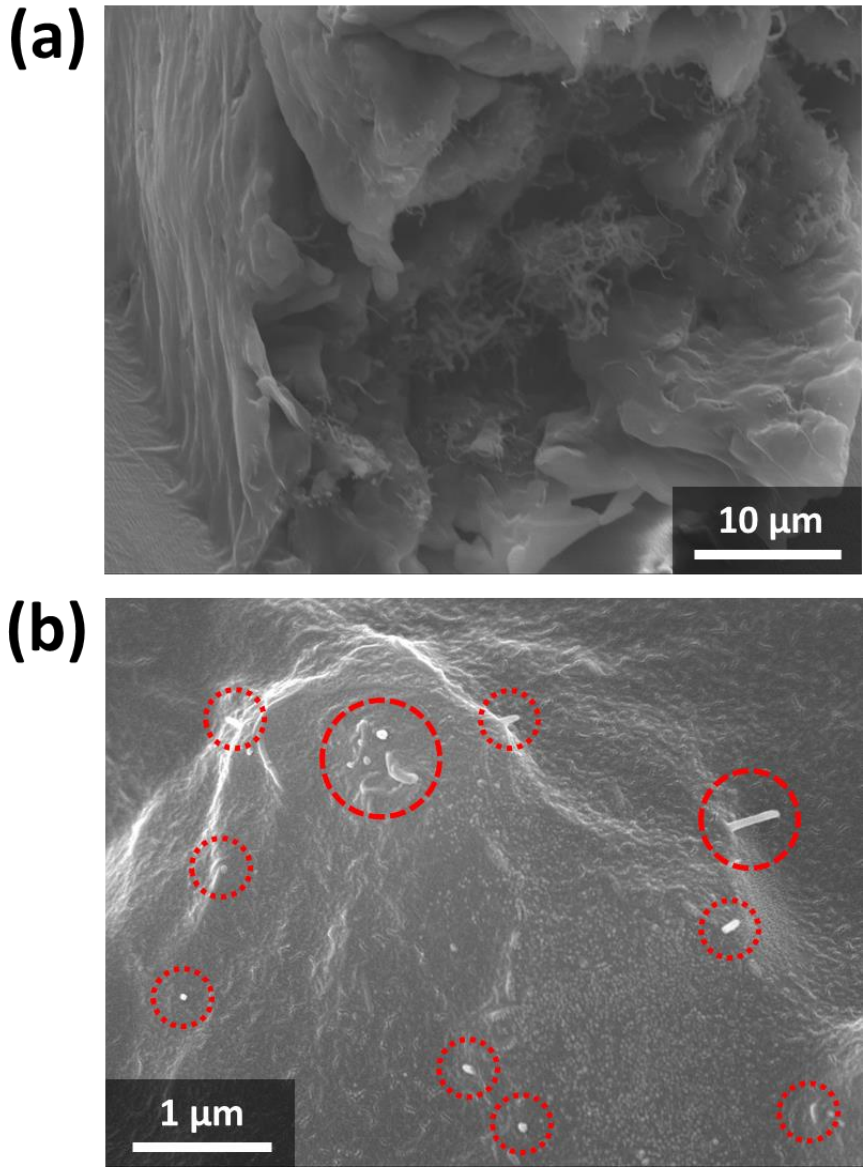


Figure 2.10. SEM image of the printed CNT/paraffin patterns.

(a) Inside and (b) outside of the patterns. Red circles mark the CNT protruding from the paraffin surface. This image was modified from S. Joo et al., *Small*, 2022[51]. The reuse permission was not required.

### 2.3.2. Electrical measurement

The electrical resistivity of the CNT/paraffin composite was measured by a four-point sheet resistivity meter (BX53F2, OLYMPUS). The resistivity can be calculated by using the following equation:

$$\rho = R_s \times d$$

where $\rho$, $R_s$, and $d$ represent the resistivity, sheet resistance, and thickness of the film, respectively. The average $R_s$ of the CNT/paraffin composite was 3.10 kΩ $sq^{-1}$. The thickness of the film was measured by using an alpha-step profiler (ASIQ3, KLA-Tencor), and the average $d$ was 46 μm (depth of employed stamp was about 50 μm). According to the equation, the calculated $\rho$ of the CNT/paraffin composite pattern was 14.6 ± 2.8 Ω cm. Figure 2.11 shows the electrical resistivity of CNT/polymer composites from another research using different matrix materials (i.e., acrylic resin) and methods (i.e., μCP)[48]. Our study has better electrical conductivity (red star mark) than that of using the μCP method; one of the reasons for this is the denser CNT networks occurring in the process. A high degree of CNT percolation will be formed during the formation of dense CNT blocks in the negative space of the stamp and the release of excess liquid paraffin[55]. However, this means that the CNT concentration mixed at an initial 5 wt% may change after patterning, and this phenomenon will be introduced in detail in Chapter 2.3.3.

It is of note that CNT composite could have chronic electrical problems because the matrix material in the composite (i.e., paraffin) can disturb the

network of CNTs. In these terms, the μTM method may be more suitable for patterning CNT composites than the μCP method because it can easily tune the electrical conductance by controlling film thickness and implementing a high thickness.

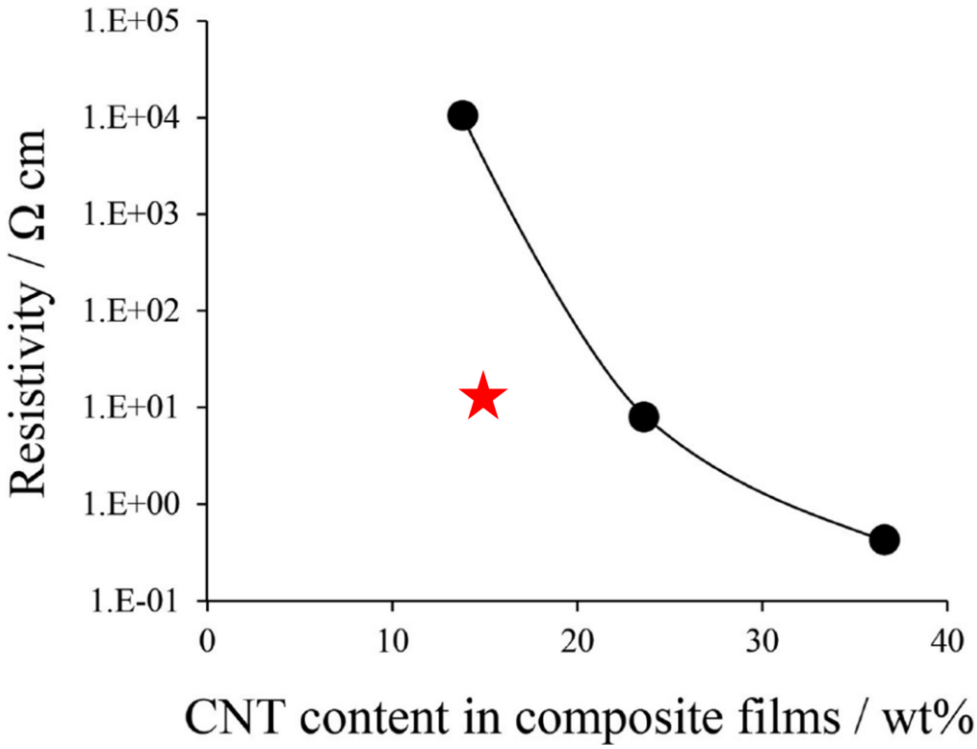


Figure 2.11. The graph of the electrical resistivity of CNT composite according to the CNT concentration.

This image was modified from Ogihara, H et al., *ACS Appl Mater Interfaces*, 2012[48]. Mark (red star) indicates the electrical resistivity of our work.

### 2.3.3. Thermogravimetric analysis (TGA)

The concentration ratio of the printed CNT/paraffin complex pattern was measured using thermogravimetric analysis (TGA) (TGA/DSC1, Mettler Toledo). Figure 2.12 shows the TGA graph measured at a heating rate of 10 ℃ $min^{-1}$ under ambient conditions. Both CNT and pure paraffin tend to single-step decomposition. CNT (blue line) was decomposed at around 600 ℃. Distinctively, the decomposition of the pure paraffin occurred in the range between 200-300 ℃. However, the CNT/paraffin composite has a three-step decomposition, and the first step is the decomposition of the paraffin in the matrix, which is outside the CNT. After a steep decrease in the first step, a range of 200-300 ℃, there is a slight mass loss from 300 to 600 ℃. It is due to the decomposition of paraffin inside the CNT networks, which require more energy to decompose[17]. The final CNT decomposition step occurs at 600 °C, indicating that the CNT weight ratio of the CNT/paraffin composite pattern is 15%. The change in the CNT concentration in the composite occurs during the filling of the composite slurry in the negative space of the stamp, as described in Chapter 2.2.1. The biggest drawback of this patterning method is the inability to control this process and the initial CNT mixing ratio.

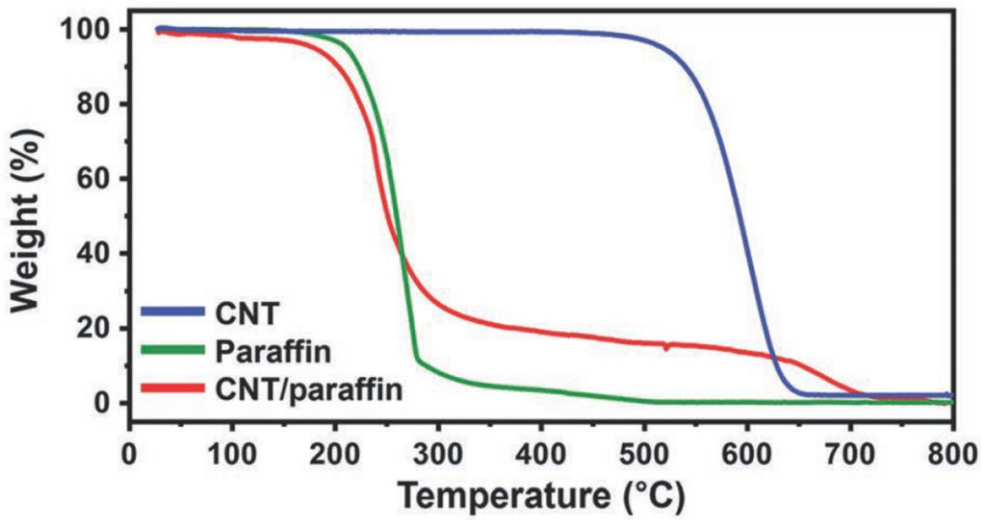


Figure 2.12. TGA analysis of the CNT (blue), pure paraffin (green), and printed CNT/paraffin composite (red).

This image was from S. Joo et al., *Small*, 2022[51]. The reuse permission was not required.

### 2.3.4. Mechanical & healing properties measurement

The bending test was performed to verify the mechanical property of the CNT/paraffin pattern. For the bending test, a sample printed with a long line pattern (width of 500 μm, thickness of 150 μm, and length of 45 mm) on a PET substrate was prepared, as shown in Figure 2.13. Continuous bending was applied to the sample at a bending radius and corresponding angles of about 10 mm and 210°, respectively. The banding frequency was 8 Hz, and electrical resistance was measured after every 2,000 cycles of bending and relaxation. Figure 2.14 shows the resistance change ratio during the bending test. The change of the resistance was less than 10% until 10,000 cycles. However, electrical resistance steeply increased after 10,000 cycles; eventually, the pattern was broken at 12,000 cycles due to fatigue integration.

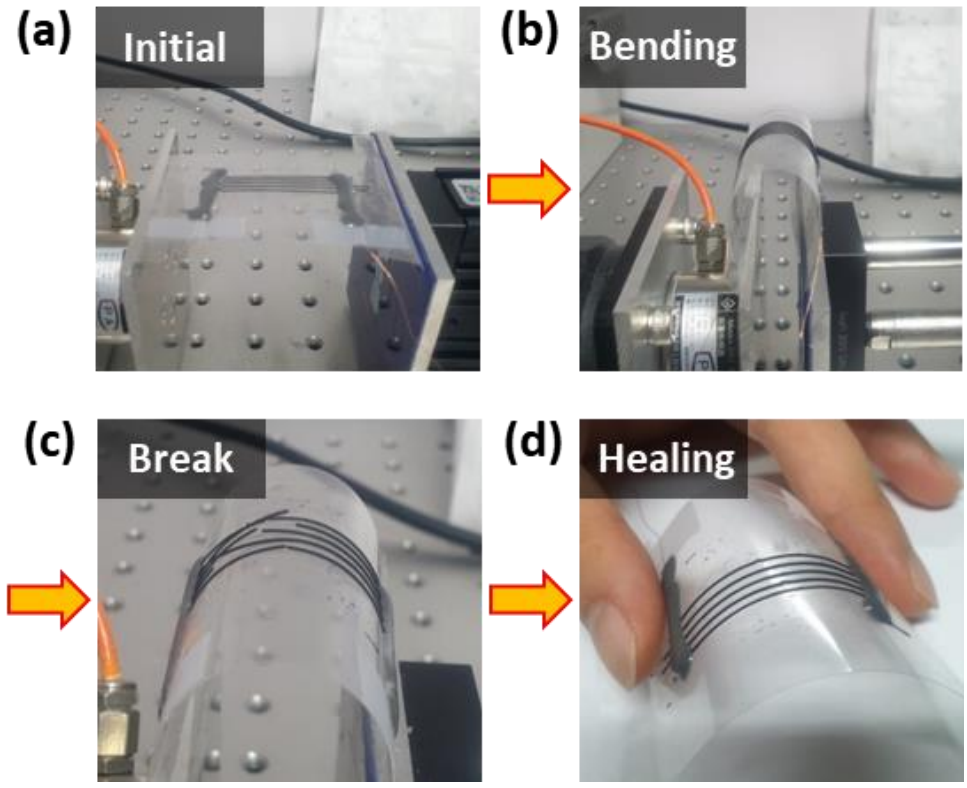


Figure 2.13. Photographs of bending and relaxation cycles and healing process.

This image was from S. Joo et al., *Small*, 2022[51]. The reuse permission was not required.

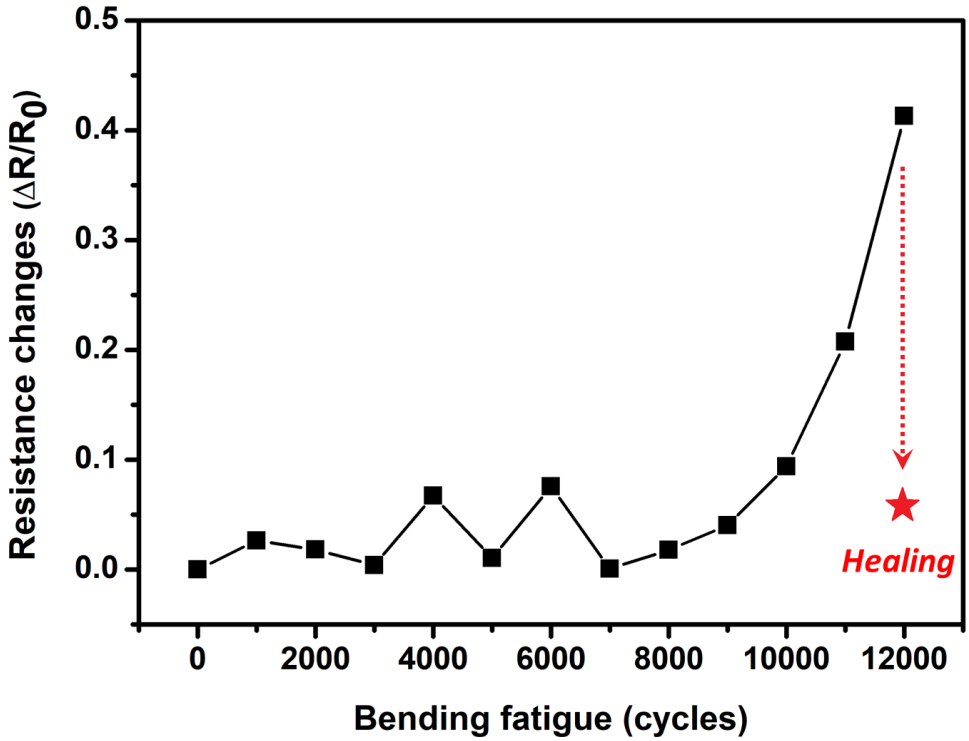


Figure 2.14. The graph of resistance change ratio according to the bending cycles.

The red star marks the resistance changes after the recovery process. This image was from S. Joo et al., *Small*, 2022[51]. The reuse permission was not required.

Interestingly, the broken patterns could be cured by applying heat, as shown in Figure 2.13 (d). Because of the properties of the paraffin constituting the composite, the pattern was cured within a few seconds at a temperature above the paraffin Tm (53-58 ℃), and the resistance was also restored to the initial value as indicated by the red star in the graph. It is of note that bending durability can be improved by lowering the thickness of the pattern. Figure 2.15 (a) shows the SEM image of a 50 μm thickness line pattern (75 μm width). This pattern did not break even after 20,000 cycles of bending; it was folded and broken randomly. The broken pattern was restored by heat treatment at 130 ℃ for 2 s. The pattern recovered the electrical resistance together with cracks and broken, although the edges melted, as seen in Figure 2.15 (b).

On the other hand, Figure 2.16 shows the point to pay attention to during the thermal recovery of the pattern. It is affected by misalignment when the pattern is completely broken and attached, and incorrect bonding could occur, as shown in Figure 2.16 (b). This misalignment may cause problems such as short circuits when the gap between the patterns is decreased.

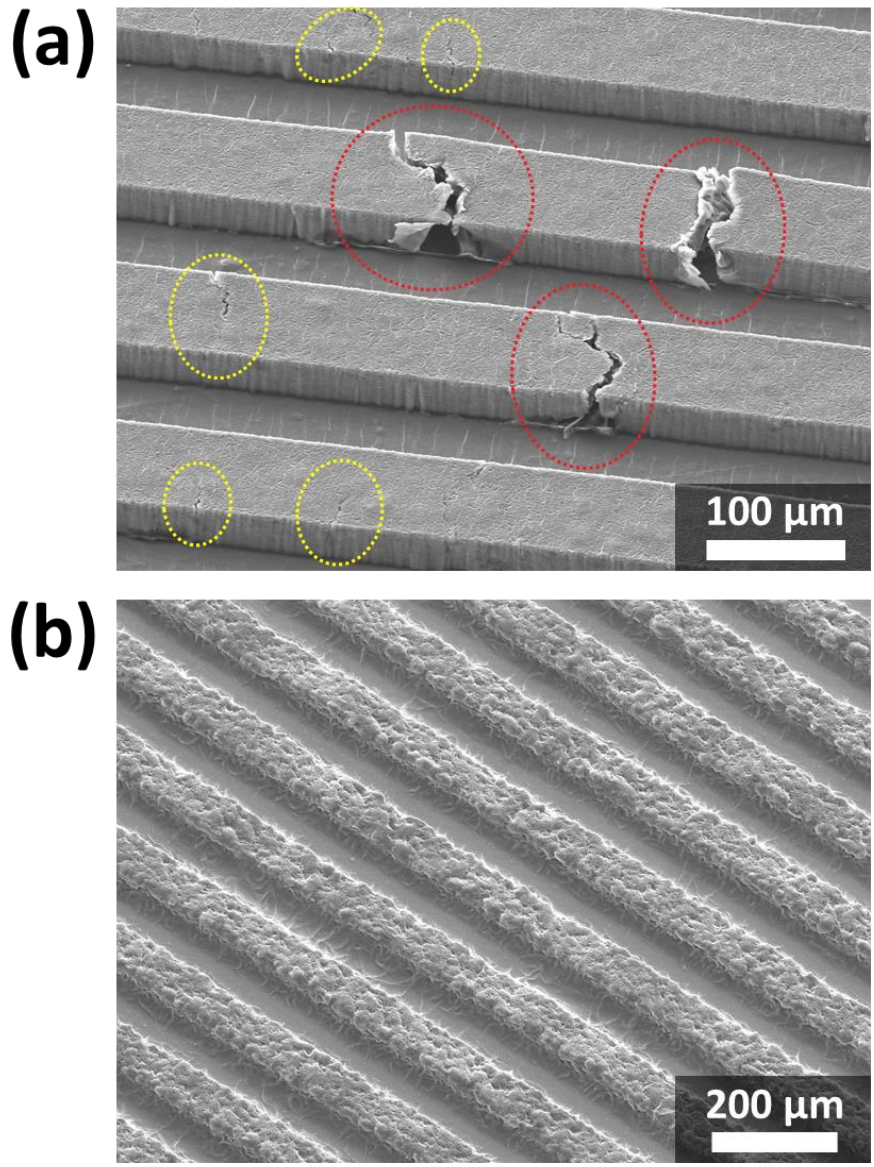


Figure 2.15. SEM images before and after the thermal recovery process. (a) Broken and (b) recovered 50 µm thick line patterns. Yellow and red marks indicate the crack and fully broken part, respectively. This image was from S. Joo et al., *Small*, 2022[51]. The reuse permission was not required.

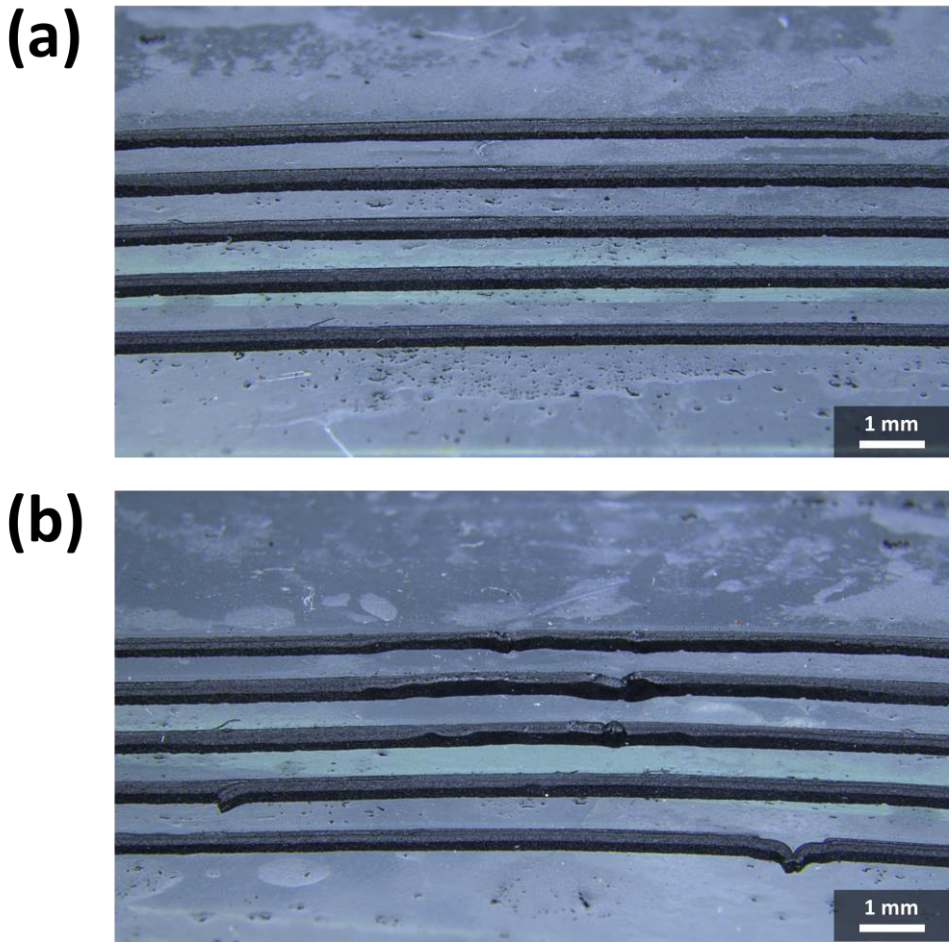


Figure 2.16. Optical images showing recovered patterns with misalignment. (a) As-printed line patterns without breaking. (b) Recovered line patterns with misalignment after the broken.

The surface energy of the substrate was also considered in the thermal recovery process. In the case of a substrate with low surface energy, such as fluorinated ethylene propylene (FEP) (significantly, when lower than the surface energy of the paraffin), adjacent patterns could be bonded due to the de-wetting of molten paraffin (the surface energy of the substrates used in this experiment can be referred to in Table 1 in Chapter 3.2). This core CNT network's shift can cause problems with electrical short. Therefore, it is crucial to overcome this problem to increase the mechanical durability as well as the thermal stability of the device employing the CNT composite pattern. Figure 2.17 (a) shows a 50 μm gap (50 μm width) line pattern printed on the FEP film fused after heat treatment at 130 ℃ for 2 s. This problem was solved by depositing the upper layer that holds the pattern in place. A thin layer of PDMS was spin-coated onto the pattern at 1500 rpm for 30 s, and cured in a vacuum oven at 45 ℃ for 2 d. It should be noted that the curing temperature of the PDMS should not be over the $T_m$ of paraffin, which could be a factor in slowing the processing speed. Figure 2.17 (b) shows optical images before and after the thermal recovery process after applying a PDMS layer to fix the pattern. It can be seen obviously that the protective layer on the pattern perfectly solves the pattern displacement problem in the thermal recovery process.

However, it could not withstand stretching forces due to the brittleness of paraffin wax. For a wide range of applications, increasing the resistance to

stretching is necessary. The brittleness of the pattern could be reduced, and elongation properties can be imparted by tuning the length and structure of the paraffin molecule chain or adding additives such as paraffin oil[56].

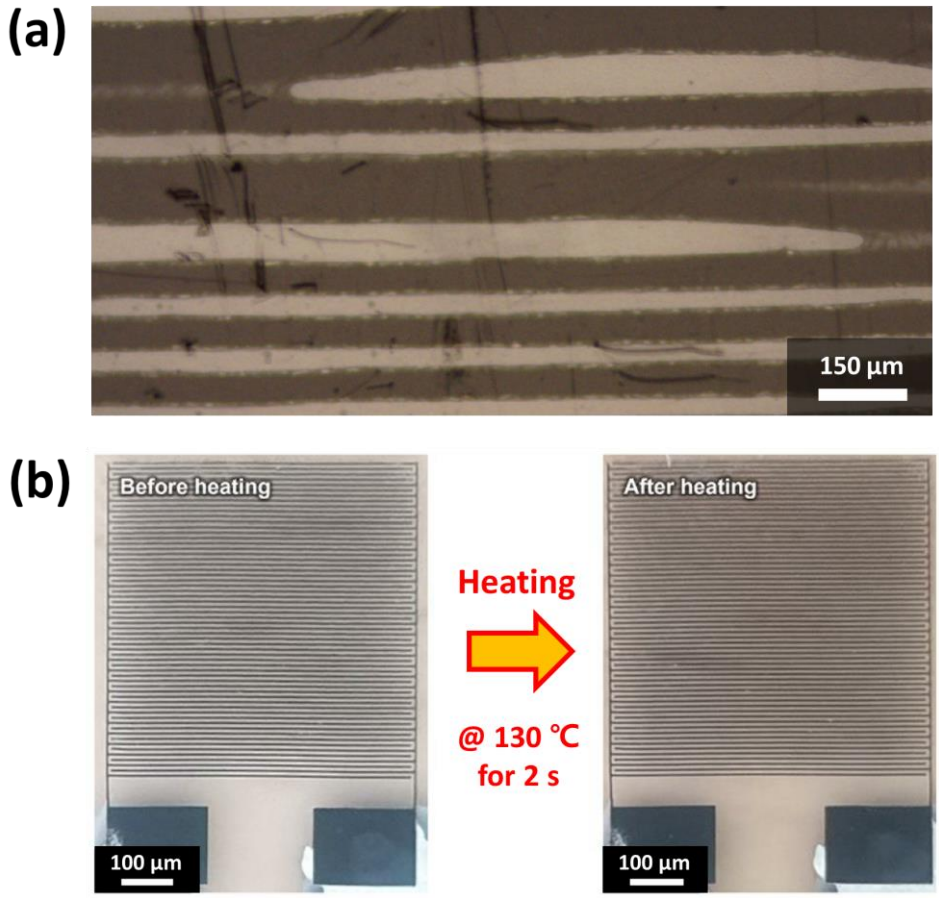


Figure 2.17. Optical images showing a pattern displacement problem in heating the 50 µm gap line pattern printed on the FEP film.

(a) The neighboring patterns fused due to the de-wetting of molten paraffin. (b) CNT/paraffin composite interdigitated pattern with 50 µm gap and width printed on the FEP film. The PDMS layer perfectly protected pattern displacement when the heat was applied. This image was from S. Joo et al., *Small*, 2022[51]. The reuse permission was not required.

## 2.4. Summary

This chapter introduced the method of patterning the CNT composite. The paraffin wax, an oligomer, was employed as a dispersion solvent for CNTs as well as also acted as a matrix in the pattern. The CNT/paraffin composite slurry sample was prepared simply by mixing and stirring. Sequentially, patterning of the CNT complex was performed by the μTM method of soft-lithography. The use of paraffin imparted a variety of advantages to the composite pattern and patterning method. For example, the threshold of the process was lowered due to the properties of paraffin (i.e., cheap, harmless, easy to access, and low $T_m$). Also, the low surface tension of paraffin enhances the adhesion to the substrate by mechanical anchoring, so transferring the pattern from the PDMS stamp to the substrate becomes easier. The CNT composite pattern employing paraffin and μTM method had two big strong points: high-resolution pattern (<10 μm) and unrestricted on the substrate. The applications fabricated using these advantages will be introduced in Chapter 4. The example of substrate type is not only the common substrate like glass, PET, and metal but also the unusual substrates (i.e., high surface roughness such as paper, leaves, and skin or low surface energy such as PFA). However, In the case of the substrate having lower surface energy than the paraffin or the pattern size becoming smaller (<100 μm), it is not sufficient to perfect transfer only with mechanical anchoring of paraffin. Therefore, an additional process was carried out to overcome this problem, which will be

introduced in Chapter 3.2.

Subsequently, the electrical characteristic of the printed CNT composite was measured by a four-point probe and stylus profiler. The calculated resistivity was ≈14.6 Ω cm, a higher value than the other research using the μCP method, which is the most used technique in soft-lithography. The reason is that the dense CNT network is composed during the patterning process. Also, it is straightforward to fabricate high-thickness patterns and control the thickness in detail in the μTM compared to the μCP method. Although these advantages exist, there are also problems to overcome. The following chapter will introduce a method to solve the problems encountered during the CNT/paraffin composite patterning using the μTM technique.

# Chapter 3. Improving the CNT/paraffin pattern

## 3.1. Paraffin cleaning process for residue removing

In our study, the excess paraffin was squeezed out from the PDMS stamp during the injection of the slurry into the negative space of the stamp. At this time, the CNT dispersed in the paraffin could be placed on the embossing of the stamp and transferred together with the pattern to the substrate. Figure 3.1 shows a printed pattern with a CNT residue, which distorts the pattern and causes electrical problems, such as short circuits, in severe cases.

To solve the problem of CNT residue, we employed an additional process, 'the paraffin cleaning process'. Figure 3.2 depicts the paraffin cleaning process. The bare PDMS was prepared on the hot plate and preheated over the $T_m$ of paraffin. Place a drop of liquid paraffin on top as a cleaning agent. Then, A composite slurry-filled PDMS stamp is placed over the drop, gently rubbed, and released. This action can be repeated a few times to remove any residue on the embossing of the stamp completely. CNTs in the inner space of the PDMS stamp are not removed as they form blocks in a dense state. What is noteworthy here is that paraffin, which acts as a dispersant in the composite, is used without other additional materials. Figure 3.3 shows the optical and SEM images of 50 μm width interdigitated patterns before and after the

paraffin cleaning process. In the image before the process, CNT residues were seen outside the pattern, and these residues connected the patterns and caused a short circuit. On the other hand, it can be seen that all residues are clearly removed after the paraffin cleaning process. Therefore, this paraffin cleaning process was carried out for every pattern after filling the slurry into the stamp and transferring it.


Figure 3.1. Photograph of the graphical pattern of CNT/paraffin composite with CNT residues.

Red circles mark the CNT residues.

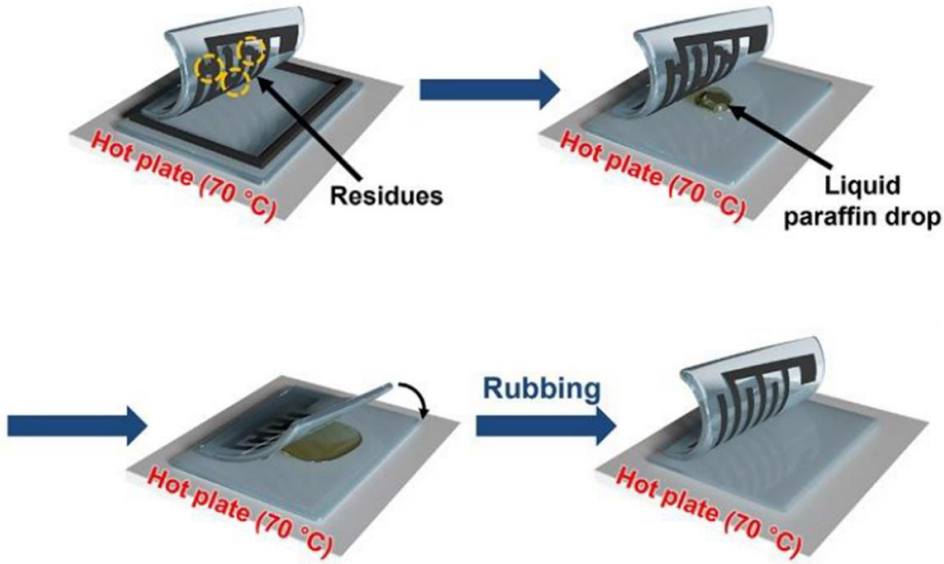


Figure 3.2. Schematic of the paraffin cleaning process for removing CNT residues on the PDMS stamp.

This image was modified from S. Joo et al., *Small*, 2022[51]. The reuse permission was not required.

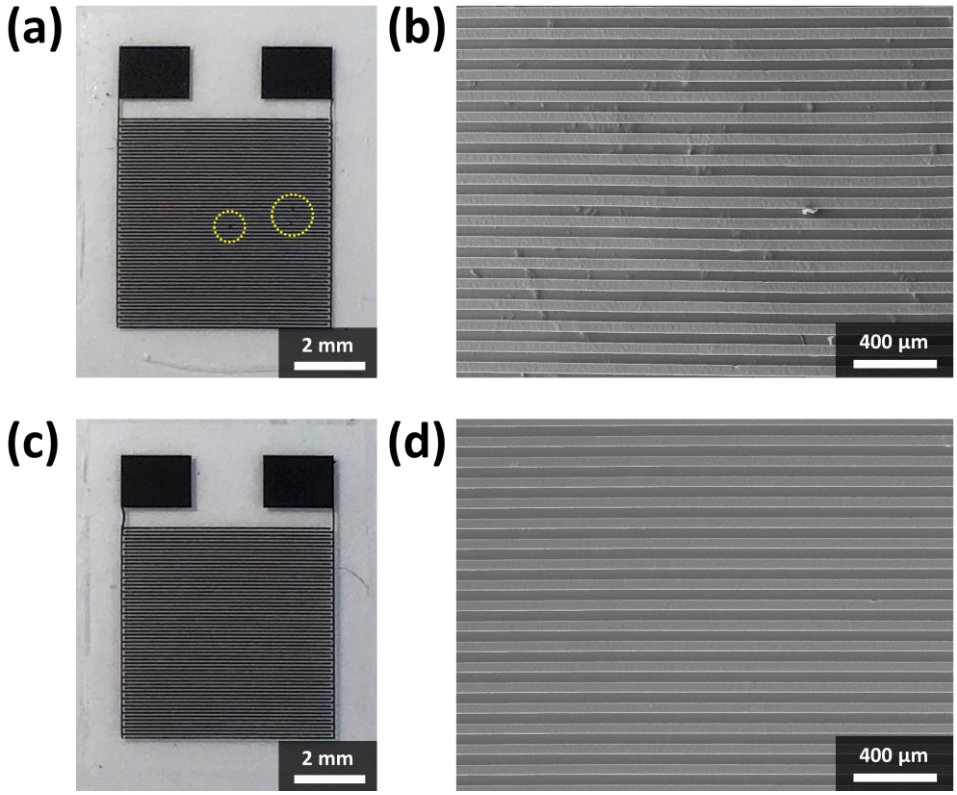


Figure 3.3. Optical measurement of 50 µm width interdigitated pattern before and after the paraffin cleaning process.

(a) Photograph of a pattern before the cleaning process. Circle marks the CNT residues. (b) SEM image of a pattern before the cleaning process. (c) Photograph of a pattern after the cleaning process. (d) SEM image of a pattern after the cleaning process. This image was modified from S. Joo et al., *Small*, 2022[51]. The reuse permission was not required.

## 3.2. Minimize bending radius peeling method

Paraffin allows the pattern of conformal contact to the substrate based on the low surface tension. It increases the pattern adhesion to the substrate, and this mechanical anchoring dramatically affects the process of transferring the pattern from the PDMS stamp (donor) to the substrate (receiver). Patterning could be efficiently performed on various substrates by this property, especially on surfaces with high roughness, such as leaves, paper, and skin. However, a transfer problem could arise under two conditions: the pattern size becomes smaller, and the receiver has a lower surface energy than the paraffin.

As the pattern width decreases, the ratio of the pattern-PDMS stamp's contact area to the pattern-substrate's contact area increases. In the experiment, for line patterns that are 50 μm height, transfer problems started to occur when narrowed to less than 50 μm width. Figure 3.4 shows the SEM image of the 50 μm width interdigitated pattern that the finger is delaminated from the substrate in the peeling process.

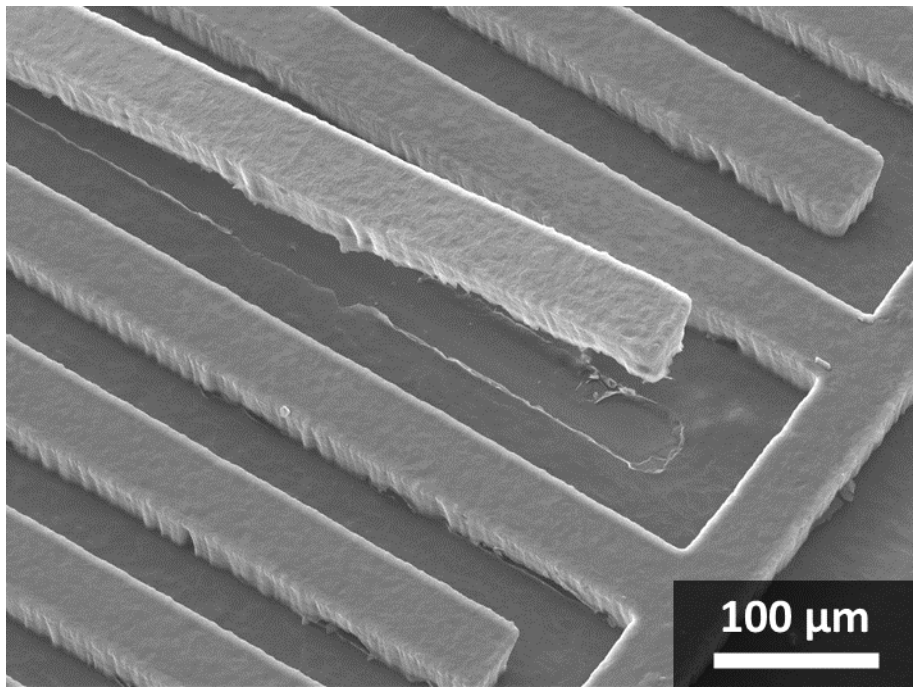


Figure 3.4. SEM image showing 50 µm width interdigitated pattern delaminated from the substrate during the transfer process.

In addition, transfer difficulties occur even on substrates such as PFA and FEP film, which are less affected by the mechanical anchoring of paraffin due to their low surface energy. Table 1 shows the surface energy of the materials used in the experiment, including paraffin. The adhesion force between two materials, A and B ($W_{A-B}$) can be calculated by the following equation based on the surface energy:[57]

$$W_{A-B} = 4\left(\frac{\gamma_A^d \gamma_B^d}{\gamma_A^d + \gamma_B^d} + \frac{\gamma_A^p \gamma_B^p}{\gamma_A^p + \gamma_B^p}\right)$$

where $\gamma^d$ and $\gamma^p$ represent the dispersive and polar components of the surface energy, respectively. On most substrates, such as PET, glass, and copper, $W_{\text{paraffin}-\text{substrate}}$ is larger than $W_{\text{paraffin}-\text{PDMS}}$, so transfer to the receiver occurs easily. On the other hand, a substrate made of a fluoropolymer such as FEP or PFA has very low surface energy, so the pattern adhesion is also low, making it difficult to transfer.

| Material | Surface energy (mJ m$^{-2}$) | | | Work of adhesion for paraffin (mJ m$^{-2}$) | Ref |
|---|---|---|---|---|---|
| | $\gamma^d$ | $\gamma^p$ | $\gamma$ | | |
| **Paraffin** | 25.1 | 0 | 25.1 | - | [58] |
| **FEP** | 15.0 | 0.2 | 15.1 | 37.6 | [59] |
| **PFA** | 15.0 | 0.5 | 15.4 | 37.6 | [59] |
| **PDMS** | 19.0 | 0.8 | 19.8 | 43.2 | [60] |
| **Latex** | 25.3 | 2.8 | 28.1 | 50.4 | [61] |
| **Leaf** | 26.2 | 3.4 | 29.6 | 51.3 | [62] |
| **Paper** | 33.5 | 0 | 33.5 | 57.4 | [63] |
| **PET** | 37.0 | 5.3 | 44.2 | 59.8 | [58] |
| **Nylon** | 30.5 | 16.0 | 46.5 | 55.1 | [64] |
| **Glass** | 28.2 | 35.6 | 63.9 | 53.1 | [65] |
| **Cu** | N/A | N/A | 1830 | N/A | [66] |

Table 1. The surface energy of the substrate materials employed in the experiment and calculated work of adhesion for paraffin.

$\gamma^d$ and $\gamma^p$ are the dispersive and polar components of the surface energy $\gamma$. It has a relationship of $\gamma^d + \gamma^p = \gamma$. This table was from S. Joo et al., *Small*, 2022[51]. The reuse permission was not required.

To solve that problem, we employed the peeling technique, 'minimize bending radius peeling method'. Figure 3.5 illustrates moments of the peeling process. The radius of curvature was controlled by wrapping and peeling the PDMS stamp on a thin rod. Roll the bar in the peeling direction and simultaneously apply force in the downward direction. As shown in Figure 3.5 (a,c), competition between $W_{\text{paraffin}-\text{PDMS}}$ and composite cohesion ($W_{\text{paraffin}-\text{paraffin}}$) occurs in the peeling of the lateral area of the pattern. Fortunately, the cohesion value of paraffin is sufficiently more significant than $W_{\text{paraffin}-\text{PDMS}}$ [67]. Additionally, since CNTs increase the mechanical strength of the matrix, the pattern can be peeled off without damaging it[68]. In Figure 3.5 (b), there is no issue in the non-patterned region because the competition between $W_{\text{substrate}-\text{PDMS}}$ and the $W_{\text{substrate}-\text{substrate}}$ is meaningless. The transfer problem is likely to occur when the upper side of the pattern is peeled off from the PDMS, as shown in Figure 3.5 (d). As mentioned earlier, the decrease in the pattern width or the low surface energy of the substrate makes $W_{\text{paraffin}-\text{PDMS}}$ more significant than that of the $W_{\text{paraffin}-\text{substrate}}$, which is the reason for the transfer failure. An enormous amount of pressure applied by pressing the bar with the finger ($P_{ext}$) was added to the $W_{\text{paraffin}-\text{substrate}}$ to solve the problem. At the same time, reducing the peeling zone with the small radius of bending curvature. After all, it causes detachment in a small region while the pattern is attached to the substrate, so the $W_{\text{paraffin}-\text{PDMS}}$ competes with the cohesion of the pattern,

and the transfer occurs stably. This peeling technique instantaneously strengthens the pattern adhesion to the substrate, overcoming the problems of the previous transfer process.

As a result, patterns could be printed down to a few micrometers (i.e., 7 μm width line), considered as resolution limit, and were able to be transferred to substrates with very low surface energy (i.e., FEP and PFA film).

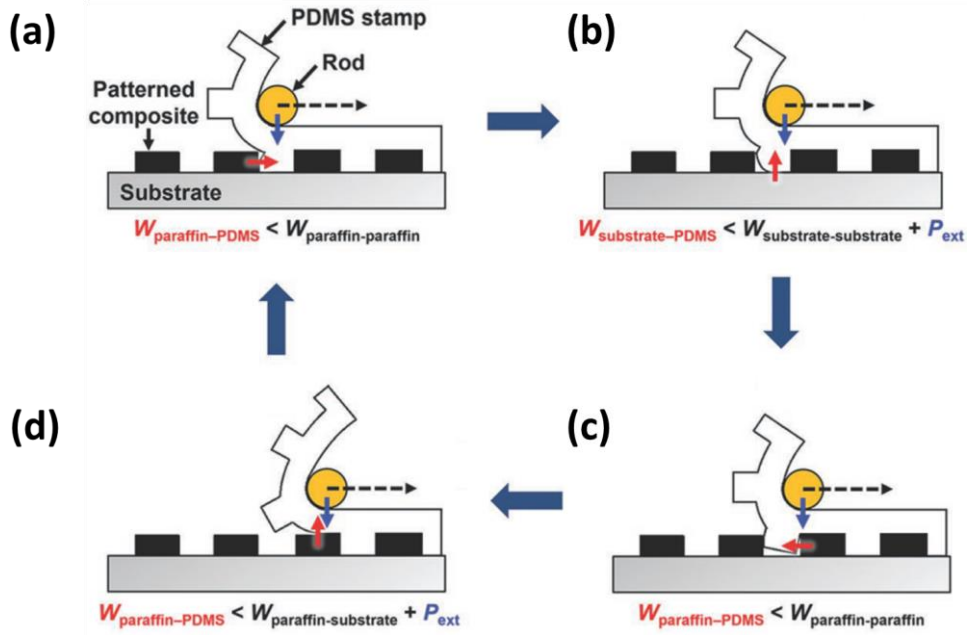


Figure 3.5. Schemes of minimize bending radius detachment method.

This image was from S. Joo et al., *Small*, 2022[51]. The reuse permission was not required.

## 3.3. Paraffin removal process

As described in the previous chapters, paraffin offers several merits in terms of processing methods and patterns. When considering the application of the pattern later, however, paraffin can be a hindrance. For example, when the pattern is applied to a battery, ions in the electrolyte cannot pass through the paraffin matrix and react electrochemically with the CNTs[69]. Therefore, it is challenging to use applications requiring a reaction in direct contact with CNT. Considering the application after the CNT/paraffin composite pattern has been printed, there is a need to remove paraffin from the pattern.

There are two main methods for removing paraffin: heat treatment and chemical treatment. Considering the TGA data of Figure 2.12 in the case of heat treatment, heat over 300 ℃ should be applied to remove paraffin. It is not a preferential method because it could damage the polymer substrate. The chemical method treats the pattern in a solvent capable of dissolving paraffin. The pattern was immersed in hexane, a non-polar organic solvent that dissolves paraffin, and properties according to hexane treatment time were investigated.

Figure 3.6 (a) shows the change in the thickness of the pattern according to the hexane treatment time. At 30 seconds of hexane treatment, the thickness sharply decreased by over 30% and gradually decreased after that. Figure 3.6 (b) shows the change in resistivity and conductivity. The resistivity was calculated using the formula in Chapter 2.3.2., and the conductivity was

calculated using the following equation:[70]

$$\sigma = \frac{1}{\rho}$$

where $\sigma$ and $\rho$ are conductivity and resistivity, respectively. Most resistivity changes occurred during the initial 30 seconds treatment, with a resistivity reduction of about 80%. After that, however, there was no noticeable change.

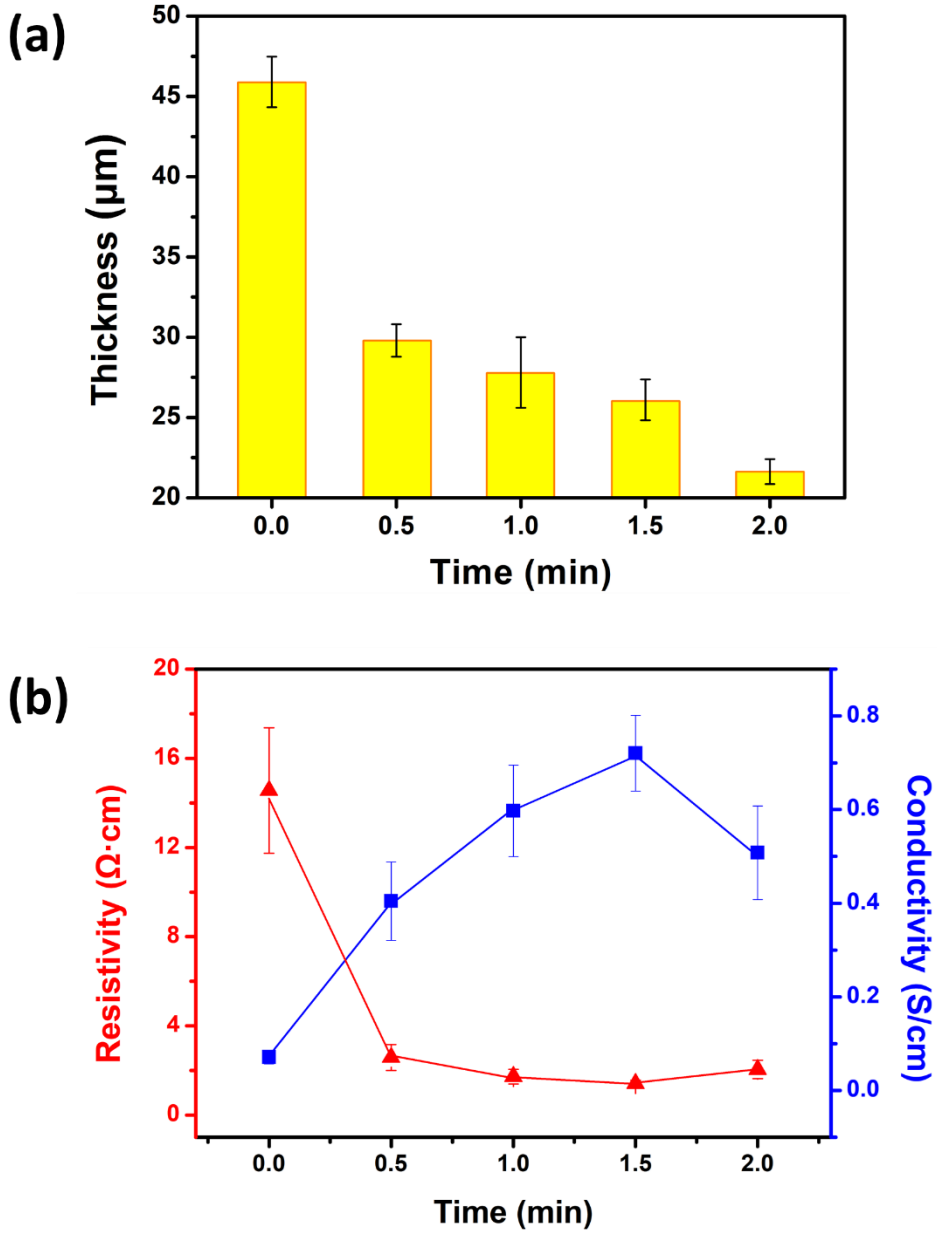


Figure 3.6. The graph of the change of physical properties by hexane treatment.

(a) Thickness and (b) electrical properties change the CNT/paraffin composite pattern according to the time of hexane treatment.

Figure 3.7 shows an optical image of a serpentine pattern with a line width of 250 μm according to the hexane treatment time. A remarkable change was observed at the processing time of 1 minute, and it can be seen that the pattern was peeled off from the substrate from this time. Peeling occurs gradually, and it suffers critical damage after 2 minutes, and cracks also occur in this process. This is because the adhesive strength is reduced due to the removal of paraffin, which was responsible for the adhesion between the pattern and the substrate. It should be noted that the delamination phenomenon during the paraffin removal could vary according to the pattern shape, size, and type of substrate.

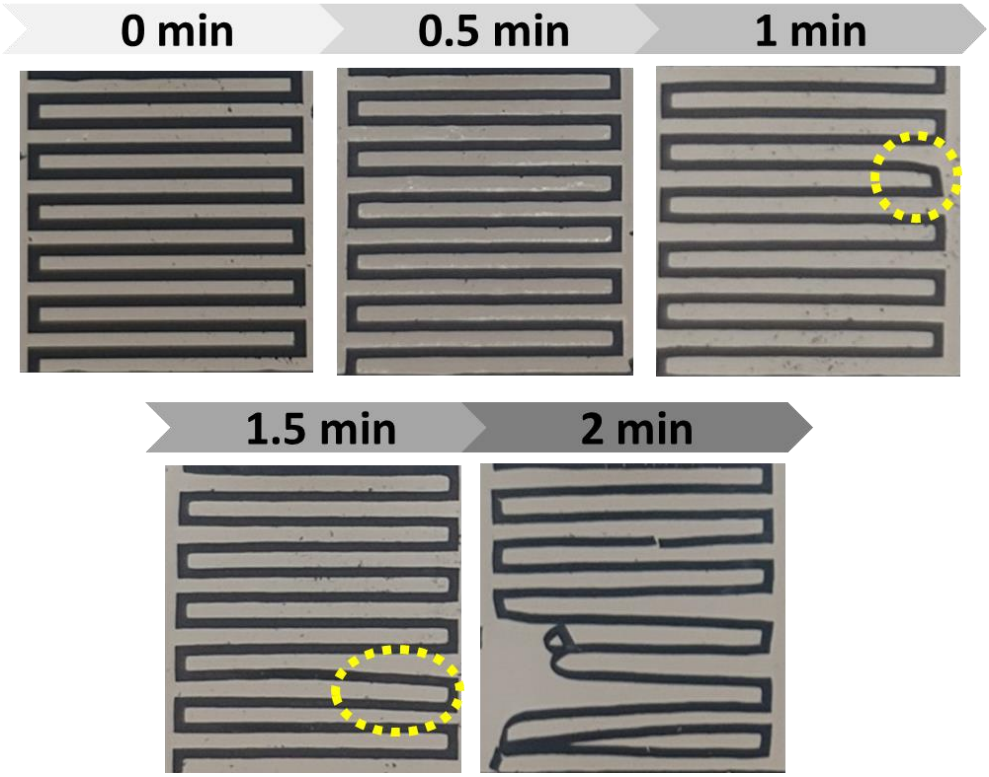


Figure 3.7. Photographs of the CNT/paraffin composite pattern according to the time of hexane treatment.

Circle marks indicate the delamination from the substrates.

Figure 3.8 shows the magnified patterned surface of a 75 μm width pattern. As it was exposed to hexane, it could be seen that the surface of the pattern was gradually eroded, and eventually, a hole was formed. This phenomenon means the possibility that the CNT core surrounded by paraffin can be exposed and reacts with foreign substances. The formation of the channel through which the CNT core is connected to the outside is crucial for electrochemical applications because it must interact with outer substances. The as-printed CNT/paraffin is not suitable for applications such as electrochemical energy storage devices or sensors because the CNT core is surrounded by paraffin and cannot react with ions. However, since the pores created by hexane can cause a direct reaction between the CNT core and ions, the hexane treatment process will enable broader applications of CNT/paraffin patterns.

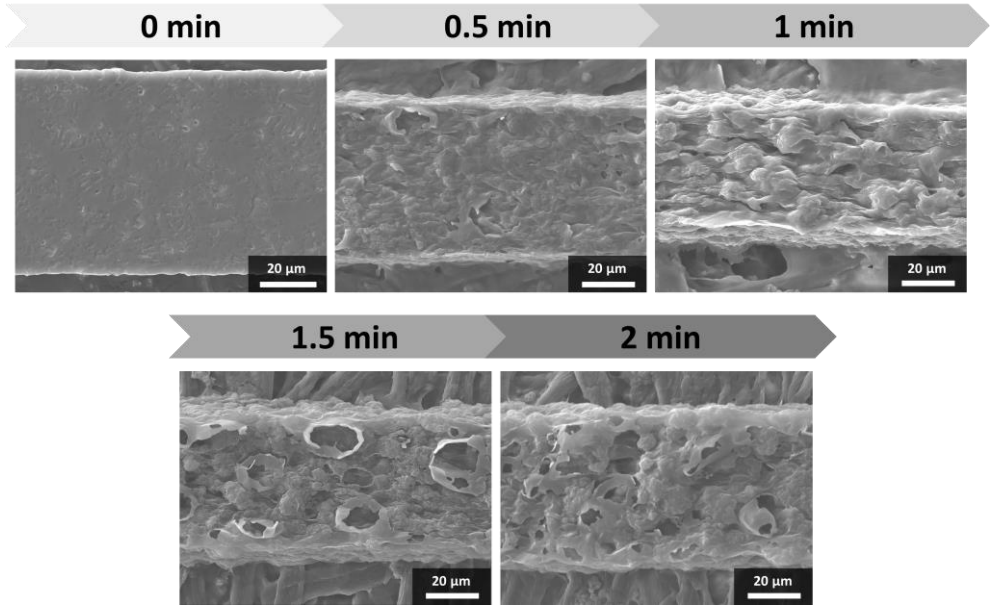


Figure 3.8. SEM images of the surface of the CNT/paraffin composite pattern according to the time of hexane treatment.

## 3.4. Summary

This chapter described how to improve processes and patterns. Residues in the printed pattern are an inherent problem with μTM. Our 'paraffin cleaning process' removes CNT residues that can cause various problems. CNT residues outside the pattern could be removed entirely, and it is encouraging that paraffin was used without using any additional material.

In addition, in the process, there arises a point at which transfer becomes difficult despite the adhesive strength of paraffin. The 'minimize bending radius peeling method' was employed to compensate for this problem. As a result, it was possible to print patterns up to a width of 7 μm, and the transfer was possible even on substrates with low surface energy (i.e., FEP and PFA film).

Meanwhile, the paraffin in the printed pattern may need to be removed, if necessary, despite its many advantages. Therefore, a selective 'paraffin removal process' was performed by treating the pattern in an organic solvent capable of dissolving paraffin. This process gives the possibility of exposure and reaction of the CNT core with an increase in conductivity but also the critical problem of delamination from the substrate. As it is a method that can expand the versatility of the pattern, more research is required.

# Chapter 4. Applications

## 4.1. Capacitive touch sensor

### 4.1.1. Introduction

Recently, demand for various sensor technologies has been increasing as the Internet of things (IoT) era approaches. Among them, the touch sensor is closely related to our daily life, from the touch screen of a smartphone or tablet PC to the next-generation wearable display[71]. Therefore, the touch sensor has been significantly studied since it was invented by E. A. Johnson in 1965 and is widely used in various fields. Many types of modern touch sensors exist, such as resistive, capacitive, piezoelectric[72,73], surface acoustic wave[74], and infrared[75]. Among them, the capacitive touch sensor is widely used due to its superior performance compared to other methods, such as excellent sensitivity and multi-touch function[76]. In this Chapter 4.1, we will introduce the fabrication and performance of a capacitive touch sensor using a CNT/paraffin composite pattern.

The driving principle of the capacitive touch sensor is to measure the change in the electric field caused by the voltage applied to the two electrodes[77]. Figure 4.1 shows a schematic diagram of a coplanar-type capacitive touch sensor. The touch sensor can measure in two modes: contact and non-contact. In the contact mode, an object (i.e., a finger) presses on the sensing area (6 mm × 6 mm), causing a physical deformation of the

elastomeric dielectric layer, and changing the capacitance between the two electrodes. On the other hand, the non-contact mode uses the fringe effect to detect disturbances in the surrounding area, allowing it to recognize an approaching object without making complete contact with the detection area[78]. In this case, the capacitance can be calculated by the following equation:[79]

$$C = n \cdot l(C_{IDE} + C_{substrate} + C_{sensor})$$

where $n$, $l$, $C_{IDE}$, $C_{substrate}$, and $C_{sensor}$ represent the number of interdigitated electrode pairs, the overlapping length between the electrode, the line capacitance without surrounding dielectrics, the line capacitance with a dielectric substrate, and the sensing capacitance, respectively. It can be seen from the equation that is increasing the number of electrode pairs engaged in the same area while maintaining a constant overlapping length makes the change in the total capacitance larger. It suggests that printing finer patterns improve sensitivity. Therefore, we increased the sensitivity of the sensor by reducing the size of the pattern by taking advantage of its ability to perform fine patterning.

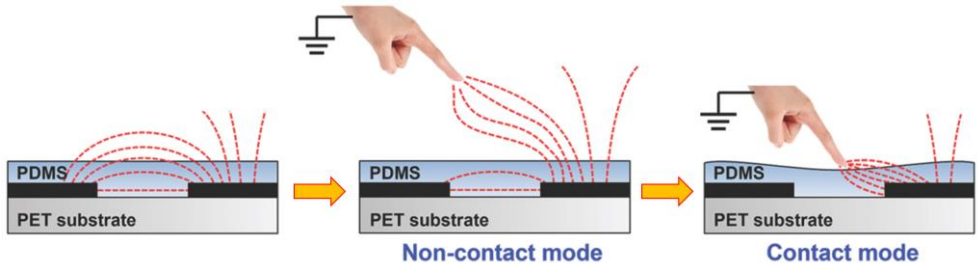


Figure 4.1. Scheme of the working mechanism of the coplanar-type capacitive touch sensor.

This image was from S. Joo et al., *Small*, 2022[51]. The reuse permission was not required.

### 4.1.2. Device fabrication

We printed a CNT/paraffin composite in an interdigitated pattern and fabricated a capacitive touch sensor. PET was used as a substrate to realize a flexible device. PDMS acting as a pattern protection and dielectric layer, was prepared by mixing the base and curing agent in a ratio of 10:1. It was spin-coated on the pattern at 1500 rpm for 30 s and was cured in an oven at 45 °C for 2 d. The profile of the PDMS coating measured by the stylus profiler is shown in Figure 4.2. PDMS filled the gaps between the patterns and was coated with a thickness of about 10 μm on it. Following the shape of the pattern, the surface is wavy, which will increase the surface area and make it more sensitive in contact mode.

Figure 4.3 shows a coplanar-type capacitive touch sensor made using a CNT/paraffin composite printed with an interdigitated pattern. Figure 4.3 (a) shows the structure of the touch sensor. It has a flexible property due to using polymers (i.e., PET and PDMS) for the substrate and dielectric layer. Figure 4.3 (b) shows optical images of interdigitated patterns with line widths of 125, 75, and 50 μm. As the line width decreases within the same area, the number of electrodes increases (the gap width coincides with the line width, so it decreases together). The number of electrodes in the interdigitated pattern with 125, 75, and 50 μm line widths is 24, 40, and 60, respectively.

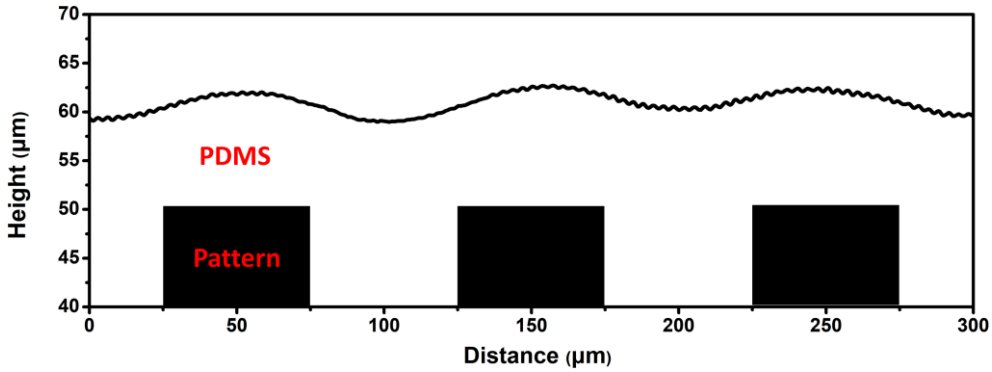


Figure 4.2. The surface profile of the PDMS-coated interdigitated pattern with 50 μm width and height.

This image was modified from S. Joo et al., *Small*, 2022[51]. The reuse permission was not required.

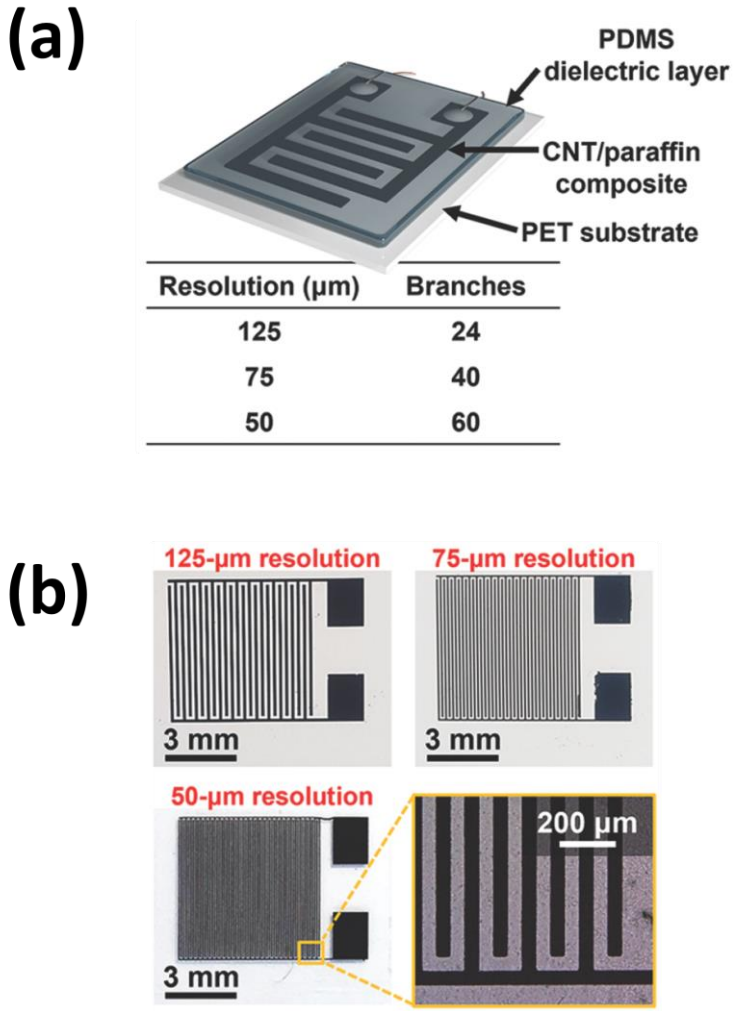


Figure 4.3. Coplanar-type capacitive touch sensor with an interdigitated pattern of CNT/paraffin composite.

(a) Scheme of the touch sensor and electrode number in pattern width 125, 75, and 50 μm. (b) Optical image of the interdigitated pattern with line widths 125, 75, and 50 μm. This image was from S. Joo et al., *Small*, 2022[51]. The reuse permission was not required.

### 4.1.3. Results

The real-time capacitance variation of the coplanar-type capacitive touch sensor with an interdigitated pattern of CNT/paraffin composite was measured by the LCR meter (E4908A, Agilent). The sample was measured in the condition of 1 V alternating voltage with a frequency of 30 kHz. Figure 4.4 shows the capacitance characteristics during the operation of the touch sensor. Figure 4.4 (a) shows the capacitance according to the driving of a touch sensor having an interdigitated line width of 50, 75, and 125 μm, respectively. The non-contact capacitance value decreased when the finger touched the PDMS sensing area (the upper part of the interdigitated pattern electrode), and the average arrival time of the finger was 0.2 s. At this time, in the non-contact state, it was far away so as not to disturb the fringe field, and in the contact state, a force was not applied to prevent the deformation of the PDMS. Figure 4.4 (b) shows the initial capacitance values along each pattern width. It can be seen that the initial capacitance values of 50, 75, and 125 μm increase as the line width and width interval of the interdigitated pattern decrease. Next, Figure 4.4 (c) is a change in the capacitance calculated from (a). As can be seen from this graph, the amount of change in capacitance also increases as the pattern becomes smaller, just like the initial capacitance. Figure 4.4 (d) shows the difference in non-contact mode depending on the width of the pattern. Note that the reference point is 2 mm from the sensing area. There was a capacitance decrease of about 0.8 pF from the far distance

that did not affect the fringe field to the point 2 mm away, and there was no noticeable difference according to the width of the pattern. Since the difference according to the width started to be seen from less than 2 mm, the amount of change in capacitance between 2 mm and 0 mm (i.e., when in contact with the sensing area) was measured using this as a reference point. The decrease in the pattern width increased the capacitance change both in the non-contact and contact modes.

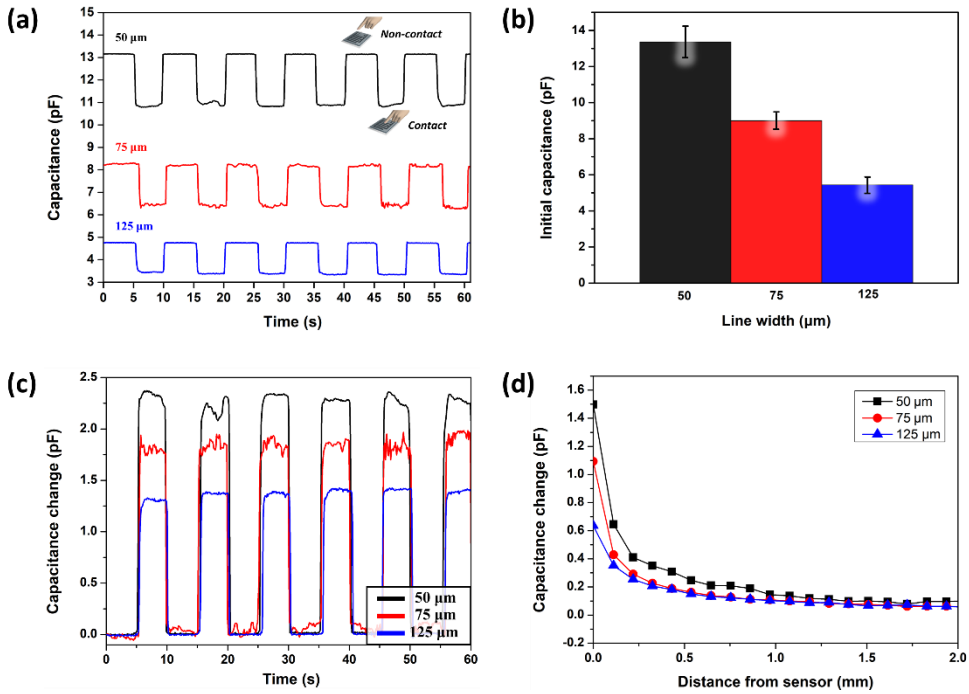


Figure 4.4. Performance of the capacitive touch sensor.

(a) Real-time capacitance variation of the touch sensor with 50, 75, and 125 μm. The capacitance decreased when it touched. (b) The bar graph of the Initial capacitance according to the line width. (c) The graph of the capacitance changes according to the line width. (d) The capacitance variation of the non-contact mode of the touch sensor in response to an approaching finger. This image was modified from S. Joo et al., *Small*, 2022[51]. The reuse permission was not required.

A bending test and heating treatment were applied to further investigate the properties of the touch sensor. For the bending durability test, the touch sensor was bent with the bending radius and corresponding angle at ≈10 mm and ≈210°, respectively, the same conditions in Chapter 2.3.4. Figure 4.5 (a) shows the change in capacitance after 20,000 bending and relaxation cycles; there's no noticeable difference compared to Figure 4.4 (c). To test the performance after heating, the touch sensor was heat treated at 130 °C for 2 s, the same as the heat recovery conditions in Chapter 2.3.4. As shown in Figure 2.16, the PDMS layer protected the pattern, so there was no risk of thermal damage such as displacement or fuse. Figure 4.5 (b) shows the change in capacitance after heat treatment, with no noticeable degradation in performance as in the banding test. Those results mean that the capacitive flexible touch sensor made of the CNT/paraffin composite was resistant to bending and heat.

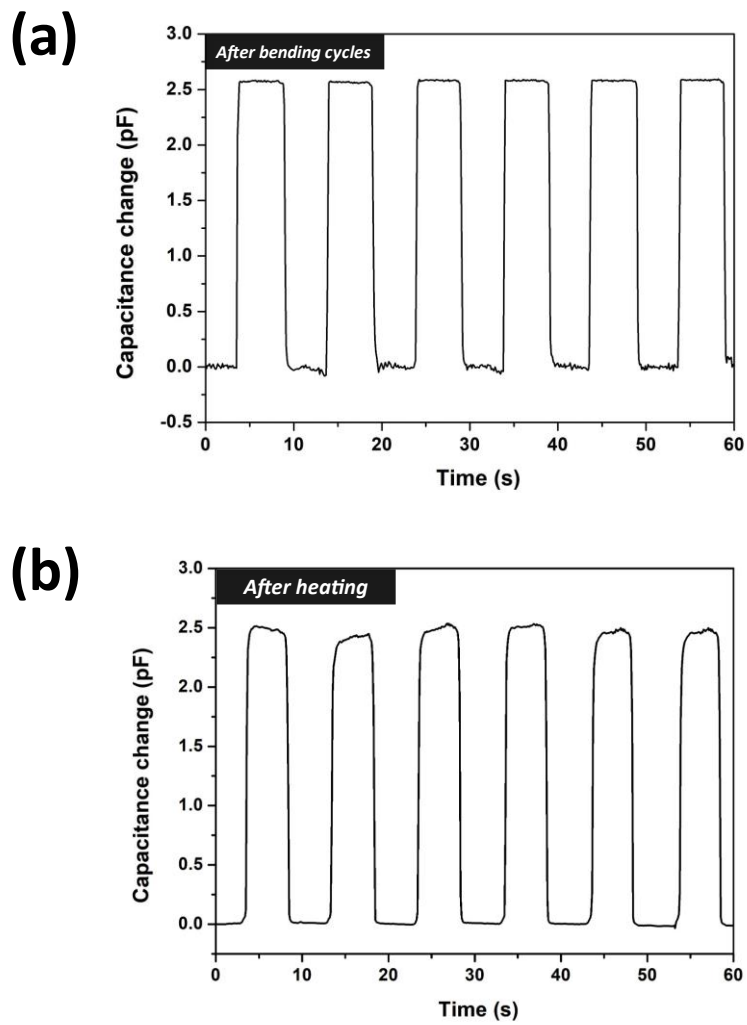


Figure 4.5. The capacitance variation after the bending test and heat treatment. (a) The graph of the capacitance change after the 20,000 bending cycles with bending radius and the corresponding angle at ≈10 mm and ≈210°, respectively. (b) The graph of the capacitance changes after heating at 130 ℃ for 2 s.

## 4.2. Water-drop energy harvesting

### 4.2.1. Introduction

In recent years, the demand for energy sources required for ultra-low-power devices has been increasing along with the development of IoT. Batteries have mainly used in small appliances' energy supply, but some problems cannot be solved with batteries alone. One of them is that the environmental pollution and cost problems are too significant to meet all energy demands with batteries. This is because millions of tons of secondary batteries are produced annually, leading to massive waste batteries[80,81]. It can be a hazardous waste for soil and water. In addition, in the case of applications closely related to our bodies, such as wearable electronics, there is a safety issue[82]. During continuous charging and discharging, dendrites generated from the cathode of the battery penetrate the separator and cause a short circuit[83]. These phenomena can lead to fire or explosion, which is fatal to safety.

Energy harvesting devices can replace batteries in specific applications because these problems are few. Among them, the triboelectric nanogenerator (TENG) reported by Wang Group in 2012 is attracting attention as a promising substitute[84]. It is an energy harvester that produces electrical energy from mechanical energy based on the mechanism of triboelectrification and electrostatic induction[85]. Unlike other energy harvesters (e.g., piezoelectric devices) and batteries, TENG can be made of

eco-friendly materials[86–90] and edible materials[91,92]. In addition, it is relatively easy to manufacture because of its simple structure. Figure 4.6 shows the operating principle of TENG. When two objects come into contact, electrons move from a relative donor to an acceptor due to the difference in electron affinity, called triboelectrification. Afterward, when two objects move away from each other by physical energy, their electrodes are charged to balance the potential. In this process, electrons move between the electrodes through an external circuit, and this causes an electric current. This phenomenon is called electrostatic induction.

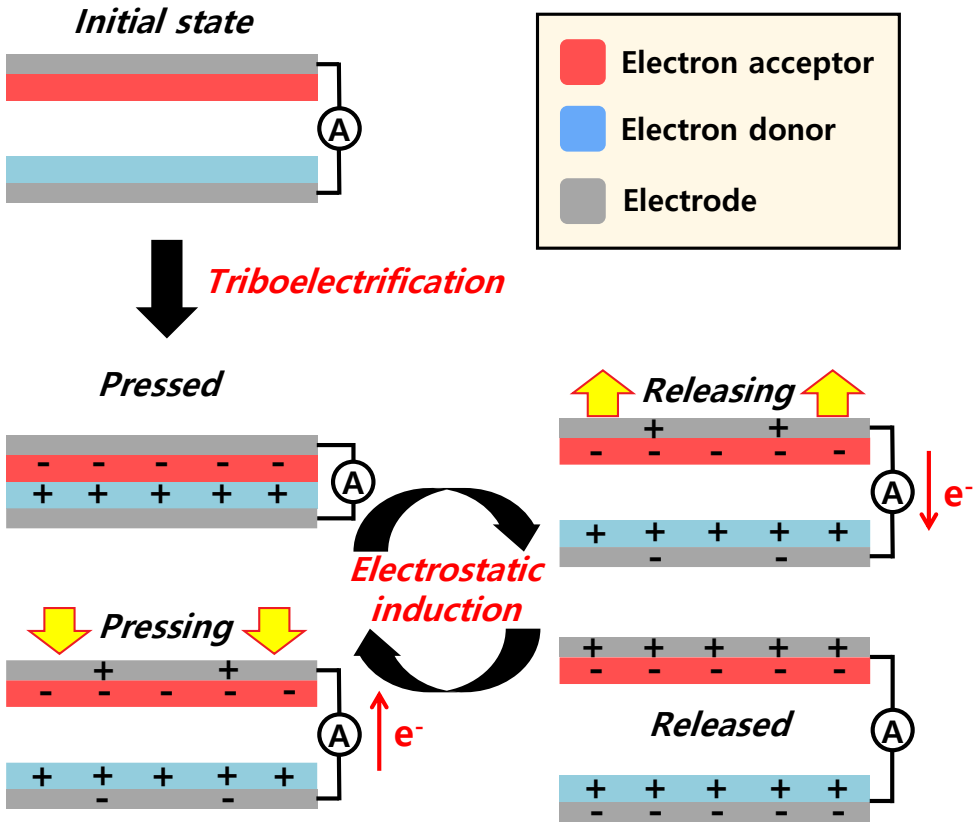


Figure 4.6. The working principle of the contact-separation mode triboelectric nanogenerator.

As two objects contact and separate, electrical energy is generated by triboelectrification and electrostatic induction.

Based on two principles, electrical energy is produced when two objects come into contact and separate repeatedly. Figure 4.7 shows the electronic energy levels of the donor and acceptor. Due to the difference in work function, the probability of electron transfer from donor to acceptor increases when contact[93]. The open-circuit voltage ($V_{oc}$) generated by the TENG operation is given as:[94]

$$(V_{oc})_{max} = \frac{Qx_{max}}{A\varepsilon_0} = \frac{C(\emptyset_1 - \emptyset_2)x_{max}}{eA\varepsilon_0}$$

where $Q$, $x_{max}$, $A$, $\varepsilon_0$, $C$, $\emptyset$ represent the amount of charges on the surface, maximum distance between donor and acceptor, effective surface area, vacuum permittivity, effective capacitance, and work function of the material, respectively. This equation shows that various factors, such as the work function and surface area of the material, determine the output value of TENG. Due to these characteristics, it is suitable for IoT, such as wearable electronics, because it can produce energy continuously from routine, repetitive energy (e.g., opening and closing doors or tires of cars) or essential physical activities (e.g., walking, blinking, and heartbeats).

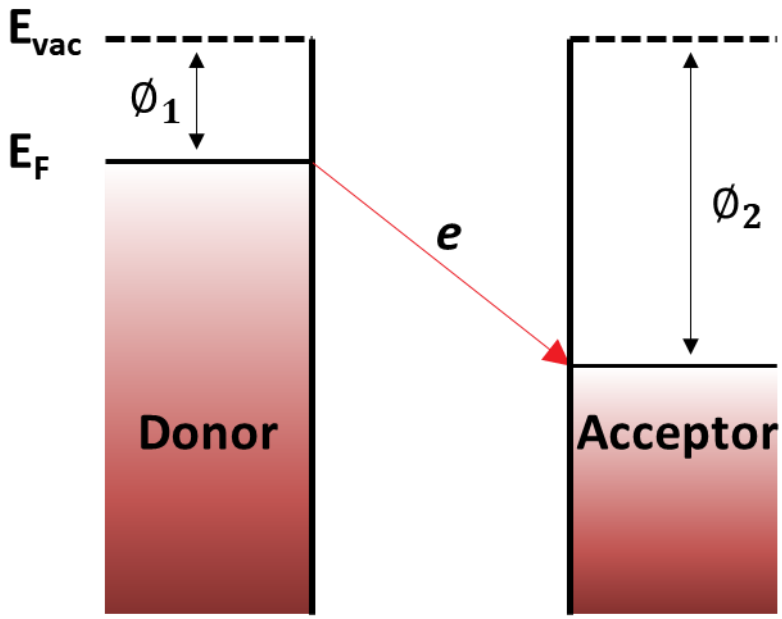


Figure 4.7. Schematic diagram showing the electron transfer between donor and acceptor in TENG based on the work function.

This image was modified from Singh, H. H et al., *Appl Phys Lett*, 2021[93].

In this chapter 4.2, a TENG device that can obtain energy from falling water droplets was fabricated using the CNT/paraffin composite pattern. The patterns were printed on the FEP film with very low surface energy (15.1 mJ $m^{-2}$) by taking advantage of not having any restrictions on the substrate. Figure 4.8 is a triboelectric series showing the charge affinity of various materials, including the materials used in this paper[95–97]. It can be seen that FEP has a higher negative charge affinity (-190 nC $J^{-1}$) than any other material. For this reason, using the FEP film creates a significant potential difference during friction, making it possible to obtain high TENG output[98]. The device that harvests the energy of the water droplet is driven by the droplet falling on the opposite side where the CNT/paraffin composite pattern is printed.

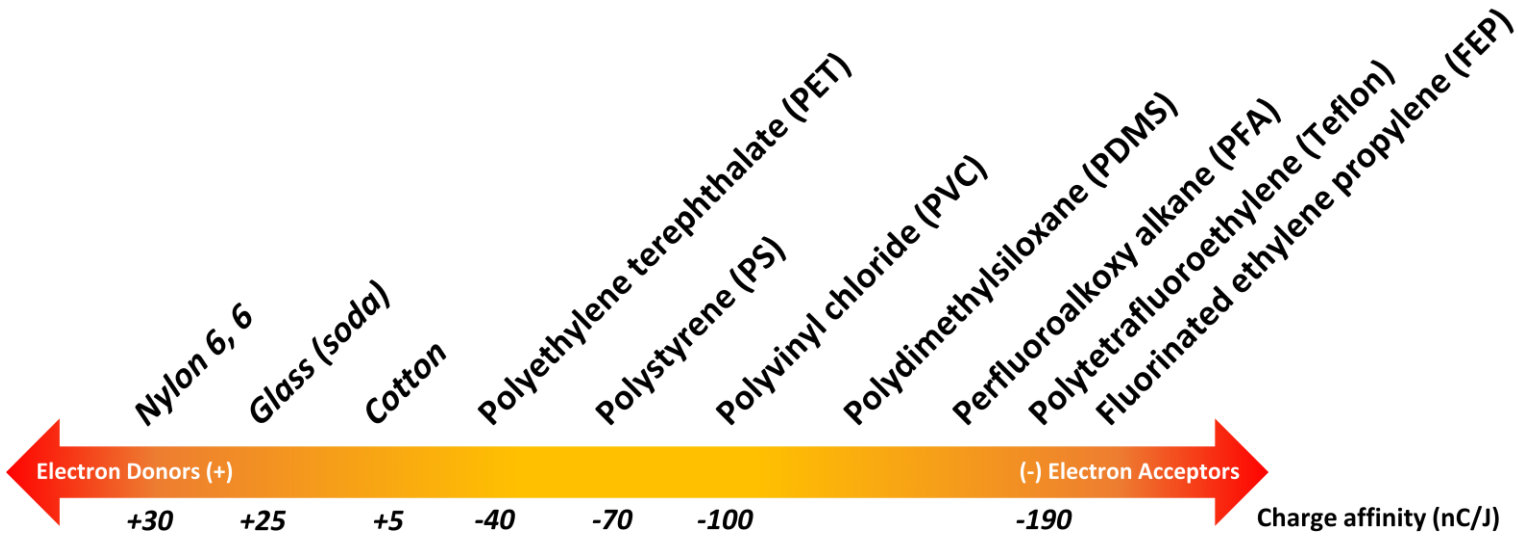


Figure 4.8. Triboelectric series of various materials, including the materials used in this application.

### 4.2.2. Device fabrication

The CNT/paraffin composite was printed directly on the FEP film (thickness 125 μm) in an interdigital pattern to fabricate the water-drop energy harvesting device. In addition, for comparison with the TENG output performances on the FEP film, the CNT/paraffin composite was also printed on the nylon film (CNH02, KOLON INDUSTRIES, INC.) and the PET film (thickness 100 μm, A-TECH). The glass fixed the pattern-printed polymeric films. For voltage and current measurements of water-drop energy harvesting, electrodes of the interdigitated pattern were connected to an oscilloscope (DS1104, Rigol) with a probe resistance of 10 MΩ and an amperemeter (6514, Keithley).

Figure 4.9 shows the operating conditions of water-drop energy harvesting. Tap water was dropped (6 mm × 6 mm) on the active area of the device through a burette, and the dropping period and the angle of the device were fixed at 3 Hz and 60°, respectively. The distances between the burette and the active area of the device were varied to 5, 10, and 15 cm.

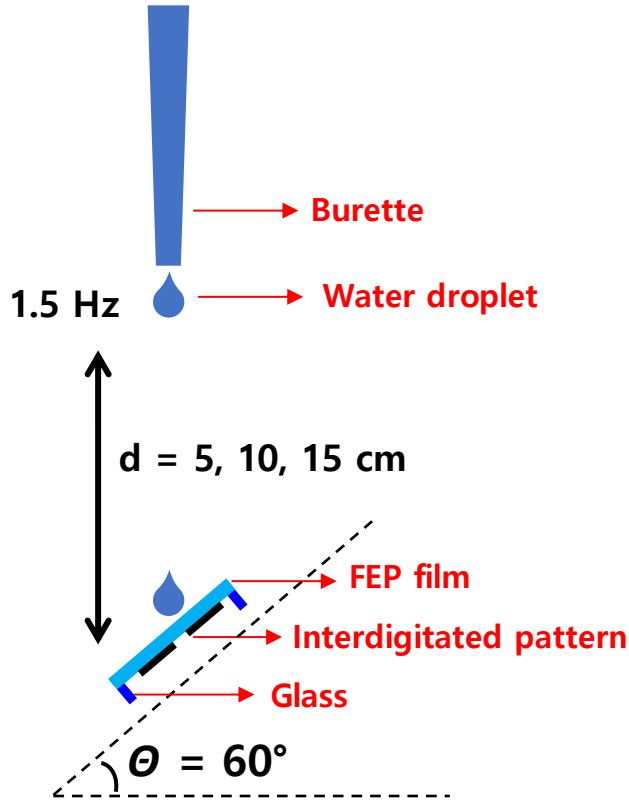


Figure 4.9. The scheme of the operating conditions of the water-drop energy harvesting device.

### 4.2.3. Results

Figure 4.10 is a schematic diagram showing the driving principle of water-drop energy harvesting. The water droplets are positively charged due to friction with the air while falling from the burette, collide with the surface of the FEP film soon, and spread widely[99,100]. At this time, due to the high negative charge affinity of the FEP, electrons move from the water droplet to the surface of the FEP to negatively charge the FEP film, which is triboelectrification. The positively charged water droplet slides along the inclined FEP hydrophobic surface and passes sequentially through the fingers of the two electrodes, causing an imbalance of charge[101–103]. Electrons move through the connected external electrode to balance the charge of both electrodes, which is electrostatic induction. Afterward, positively charged water droplets fall continuously (3 Hz) and produce an electric current.

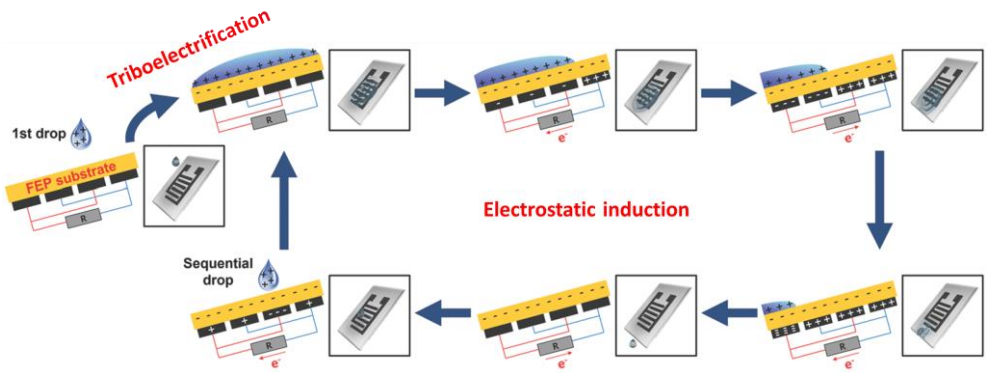


Figure 4.10. The schematic of the working principle of water-drop energy harvesting.

This image was from S. Joo et al., *Small*, 2022[51]. The reuse permission was not required.

Figure 4.11 shows the output performances of water-drop energy harvesting influenced by the advantages of patterning, high-resolution, and various substrate availability. The distance between the burette and substrate was fixed at 15 cm, and the substrate angle was 60°. Figure 4.11 (a,b) shows that the output voltage and current increase as the width of the electrode pattern decrease. Based on previous studies, it can be seen that as the number of fingers of the interdigital electrode increases, the output value enhances due to the increase of the accumulated charge[101]. Therefore, obtaining more output voltage and current was possible by printing more electrodes in the same area while reducing the pattern size through sophisticated patterning.

Meanwhile, the substrate is of note because the contact material plays a crucial role in TENG. Since the substrate contact with the positively charged water droplet, the greater the negative charge affinity, the greater the output value. When referring to the triboelectric series of Figure 4.8, it is expected that substrates such as FEP or PFA, which have low surface energy due to the functionalization of fluorine on the surface, will be advantageous for output. We printed an interdigitated pattern with a width of 50 μm on three types of polymer substrates, nylon, PET, and FEP films. Figure 4.11 (c, d) shows the output values of the water-drop harvesting device using each polymer film. As expected through the triboelectric series, the maximum open-circuit voltages and short-circuit currents of about 8.6 V and 90 nA were obtained on the FEP substrate, respectively. On the other hand, no output values were

produced on the other substrates.

To investigate the output value according to the setup, it was measured under various conditions. Figure 4.12 shows the output voltage and current while adjusting the distance between the burette and the substrate and the angle of the substrate. Water droplets falling from a high distance are spread wider after hitting the substrate, showing great output due to the increased contact area. Also, as the angle of the substrate increases, water droplets on the substrate roll down faster and pass more electrodes per unit of time, generating greater output. However, if the two conditions become too large, causing abnormalities in the motion of water droplets that collide, spread, and roll, adversely affecting the output.

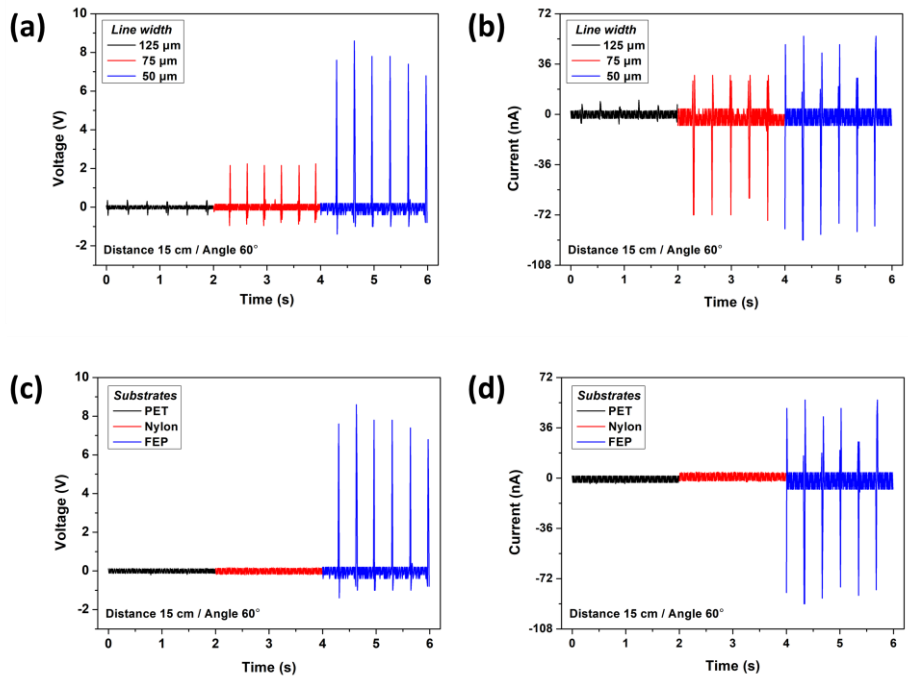


Figure 4.11. The output performance of the water-drop energy harvesting devices affected by patterning characteristics.

The output (a) voltage and (b) current according to the line width of the electrode. The output (c) voltage and (d) current according to the substrate of the electrode. This image was from S. Joo et al., *Small*, 2022[51]. The reuse permission was not required.

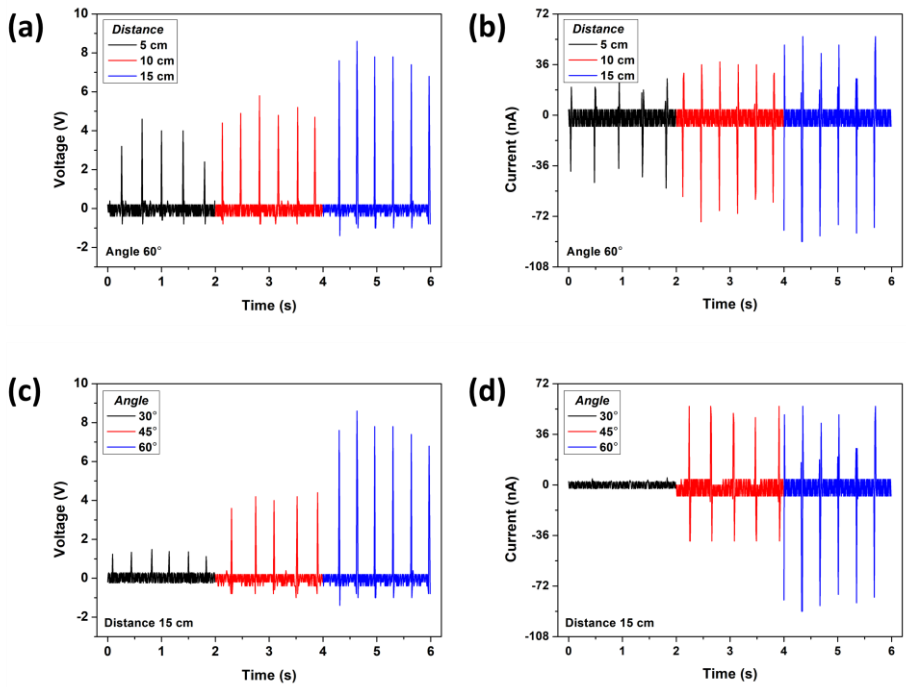


Figure 4.12. The output performance of the water-drop energy harvesting devices affected by the experimental setup.

The output (a) voltage and (b) current according to the distance between the burette and substrate. The output (c) voltage and (d) current according to the angle of the substrate. This image was from S. Joo et al., *Small*, 2022[51]. The reuse permission was not required.

## 4.3. E-textile for wearable electronics

### 4.3.1. Introduction

Electronic textiles (e-textiles) have been attended for decades due to the great potential of wearable technology. It has a wide range of applications as it can be applied in a variety of forms throughout the human body for various purposes such as human-machine interaction, energy harvesting, and healthcare[104–107]. To realize it, many studies have been conducted with various methods. Table 2 shows a variety of ways to implement e-textiles. The most widely studied method in recent years is to impart functions to the fibers and weave them. Functional fibers can be obtained by sequentially coating the fibers with various materials (i.e., carbon nanotube, silver nanowire, and polyvinylidene fluoride)[108–110] or by spinning technique (i.e., wet spinning[111] and electrospinning[112]). Textiles woven with functional fibers can make clothes, which are high-performance electronic devices on their own[113]. It is also possible to customize the cloth by controlling it from the fiber unit, however, it is usually hard to make clothes due to difficulties in weaving[114].

In contrast, other studies focus on using commercial textiles directly. Commercial textiles are given functionalities through various techniques such as carbonization[115], sputtering[116], screen printing[117], laser ablation[118], and inkjet printing[119,120]. It is a generally simple process, and the appropriate method can be chosen depending on the applications and materials, but it can be irreversible, damage the textiles, or not be easy to repair. Meanwhile, other

researchers attach electronic components to textiles through soldering[121], cilia structures with PDMS adhesive[122], and thermal lamination with thermoplastic films[123], which can solve those problems.

| E-textile | | |
|---|---|---|
| **Method** | **Techniques** | **Ref** |
| **Material** | Coating fiber | 108 |
| | Wet spinning | 111,113 |
| | Electrospinning | 112 |
| **Modification** | Carbonization | 115 |
| | Sputtering | 116 |
| | Screen printing | 117 |
| | Laser ablation | 118 |
| | Inkjet printing | 119,120 |
| **Sticking** | Soldering | 121 |
| | Micro-cilia | 122 |
| | Lamination | 123 |
| | Knitting, Weaving, Sewing | 114,124 |

Table 2 . Various methods for implementing e-textiles.

We describe a method for printing the CNT composite patches on clothes for e-textiles in this Chapter 4.3. Unlike other sticking methods, our CNT patches do not require any extra adhesive or processes for attachment due to the adhesion of paraffin in the composite. In the attaching process, the melted paraffin is absorbed on the surface of the textile and hardens again, thereby improving adhesion. The CNT patch has a different adhesive force depending on the applied pressure, and it can have two types: a 'sticker type' for temporary attachment and transfer and a 'printing type' for continuous attachment. In the sticker type, the CNT patch can be easily attached to the textile by low pressure with heat. It can also be neatly detached from the textile and be freestanding by carefully peeling off, which means that the inherent problem of the electronic fabric is free to wash[125]. The freestanding CNT patch can be stored on PFA film, which has the advantage of being easily transferred to other textiles due to the low surface energy of the PFA film (15.4 mJ $m^{-2}$). The patch could be transferred several times, with each transfer reducing the amount of paraffin remaining on the textiles. It indicates adhesion gradually decreases; the life of the patch is about 5 times transfers. In this form, it breaks when folded, but it can be healed easily by heat. On the other hand, the printing type made with a stronger pressure cannot transfer but can stick to the textile with a stronger adhesive force and is resistant to folding.

The CNT patches attached to the textile were applied to the single-electrode mode TENG as an electrode. Figure 4.13 shows the four working modes of the TENG: vertical contact-separation mode, single-electrode mode, lateral-sliding mode, and freestanding triboelectric-layer mode[98]. In particular, the single-electrode mode does not require connecting electrodes to moving parts, unlike other modes of TENG, reduces system limitations and complexity, and increases flexibility[126]. Single-electrode mode TENG is fabricated by attaching CNT patches to the textile and friction on another side with PFA film. The TENG output value can vary depending on the type of textile due to the different charge affinity. A triboelectric series, including the employed fabrics, can be seen in Figure 4.14. Estimating from the triboelectric series, the TENG output values of fabrics using counter materials as PFA films will be more significant in the order of positive charge affinity: nylon, cotton, and polyester. Considering the practical application, however, PFA polymeric film should change to cloth, so nylon textile is adopted as to counter layer. In this case, fluorine was spray-coated on the counter nylon layer to impart a difference in charge affinity. As a result, the TENG output voltage increased about 8-fold compared to that of pristine. Lastly, the CNT patches are reliably applied to commercial clothes, which can be used as wearable electronics.

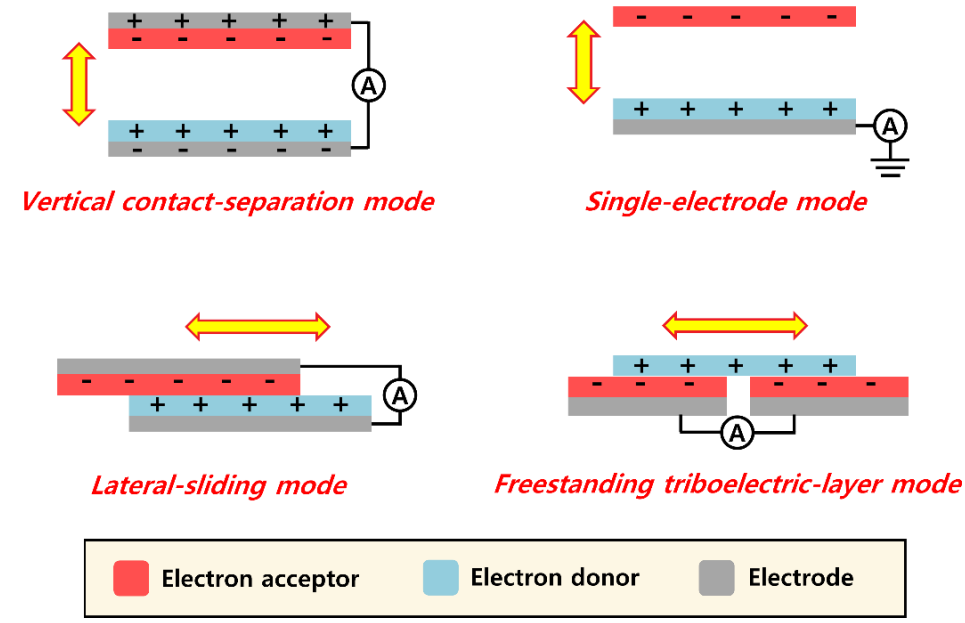


Figure 4.13. Four working modes of TENG.

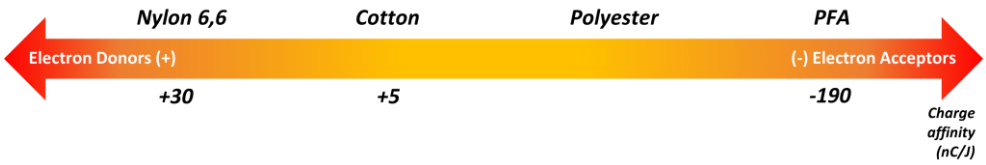


Figure 4.14. A triboelectric series including fabrics: nylon, cotton, polyester.

### 4.3.2. Device fabrication

To implement e-textile for wearable energy harvesting, CNT/paraffin composite was printed on the textile. Figure 4.15 describes the patterning process of the CNT/paraffin composite on a textile. The patterning process is the same as that described in Figure 2.4. Because wearable devices are close to our lives, design parts are also important when considering practicality, so we chose a graphical pattern with an area of 254 $mm^2$ [127].

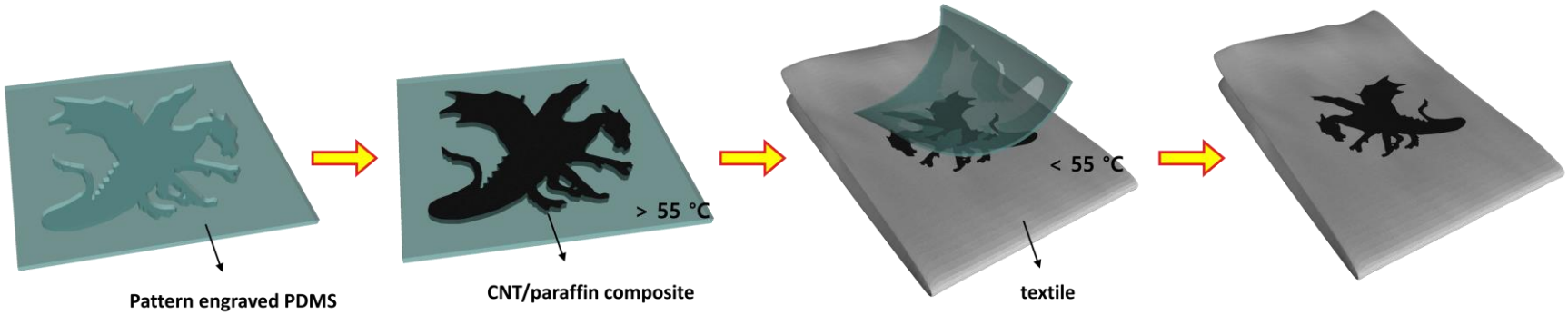


Figure 4.15. The schematic of the CNT composite patterning process on the textile.

### 4.3.3. Results

The graphical CNT patch printed on the textile can be seen in Figure 4.16. In the process of transferring the CNT patch from the PDMS to the textile, liquid paraffin permeates into the surface of the textile and hardens, increasing adhesion. The topography of the CNT patch surface after peeling off from the nylon textile indicates that it was attached stable through conformal contact between the paraffin and the textile, as shown in Figure 4.16 (e). Therefore, CNT patches can be printed on textiles such as nylon, cotton, and polyester. It can be detached clearly from the textile by carefully peeling and re-attaching.

Figure 4.17 show multiple attach-detach processes of the CNT patches to nylon textile. When the CNT patch was re-attached, it was placed on the textile and heated at 120 °C for 5 s. Paraffin residues were observed on the nylon textile after peeling the patch. The removed CNT patch was freestanding and easy to handle. In addition, it was attached to the PFA film for storage. The PFA film has a low surface energy (15.4 mJ $m^{-2}$), so it can be easily peeled off or transferred directly to a textile. It can be seen that the amount of paraffin residues on the textile decreases as the process of attaching-detaching the CNT patch is repeated. As the process progresses, the paraffin concentration of the CNT patch decreases, and the adhesion strength decreases. In the end, the CNT patch attached to the nylon textile of Figure 4.17 (h) for the fifth time had very weak adhesion, indicating the transfer life

of the CNT patch. To quantify the adhesion of the CNT patch to the textile by the number of transfers, a lap shear adhesion test was performed. As shown in Figure 4.18, the printed CNT patch on a 4 cm × 9 cm nylon textile was covered with another same nylon fabric and attached by treatment at 120 °C for 5 s. Figure 4.17 (i) shows that the adhesion of the CNT patch decreases due to the loss of paraffin in every transfer process. After 4 transfers, the adhesion was reduced by more than half compared to the pristine. The type of the CNT patch that can be attached-detached with such weak adhesion was named 'sticker type'.

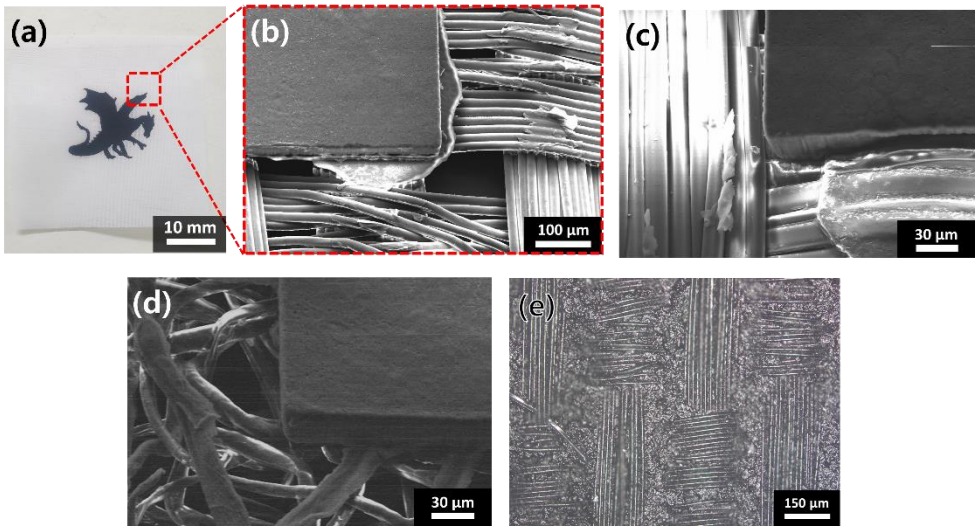


Figure 4.16. The CNT/paraffin composite pattern printed on the textile.

(a) Photograph of the 254 $mm^2$ area pattern on the nylon textile. SEM image of pattern printed on the (b) nylon, (c) polyester, (d) cotton cloth. (e) The surface of the CNT patch after peeling from the nylon textile.

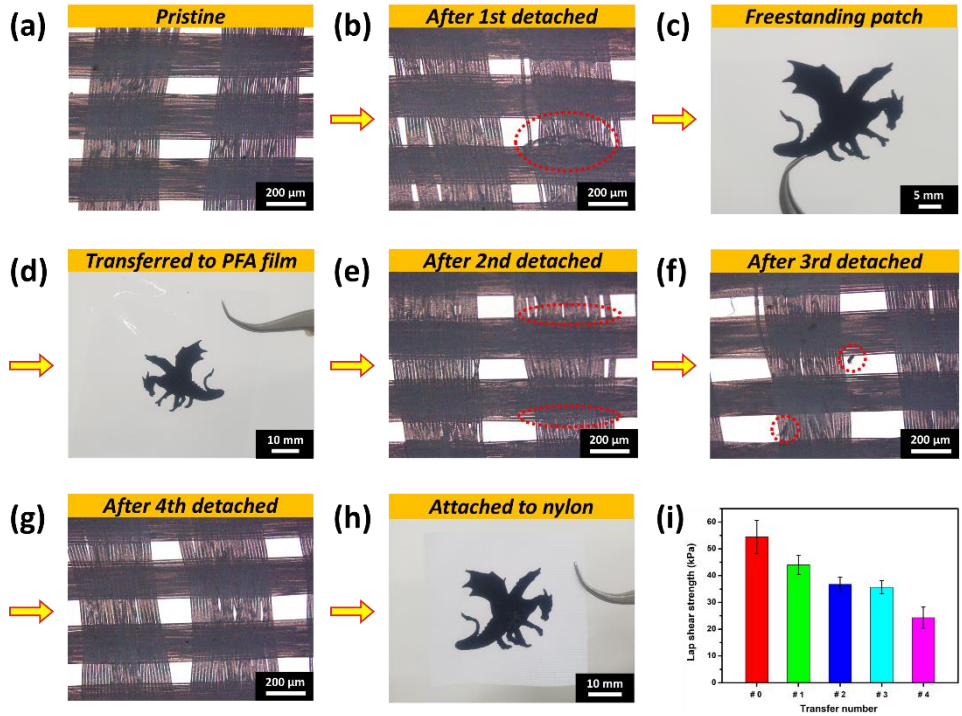


Figure 4.17. Optical images of the multiple CNT patch transfer process.

(a) Pristine nylon textile without residues. (b) Nylon textile after detaching the CNT patch the first time. Red marks indicate the paraffin residues on the textile. (c) Freestanding CNT patch carefully peeled from nylon textile. (d) CNT patch attached to PFA film for storing. (e-g) Nylon textile after detaching the CNT patch second, third, and fourth time, respectively. (h) CNT patch attached to nylon after detached four times. (i) Lap shear adhesion test of a CNT patch according to the number of transfers.

On the other hand, the adhesion of the CNT patch to the textile increased by applying additional pressure, assuming the actual ironing situation. The samples were heated at 120 °C for 5 s and then solidified at room temperature while pressing at 5, 20, and 40 kPa, respectively. Figure 4.19 shows an SEM cross-sectional image of the pressed CNT patch. The printed CNT composite patch was pressed into the textile as pressure was applied. Under the pressure of 5, 20, and 40 kPa, the thickness of the CNT patch on the textile was 72, 37, and 16 μm, respectively (the thickness of the textile was about 90 μm). Figure 4.20 (a) shows the lap shear strength of the CNT patch according to pressures of 5, 20, and 40 kPa. 5 kPa is similar to the initial pressure when transferring from the PDMS stamp to the substrate. Therefore, it has a similar degree of adhesion to #0 (i.e., initial adhesion before transfer) in Figure 4.17 (i). The stronger the pressure, the more the patch enters the textile and the stronger the adhesion, and the sheet resistance also changes as in Figure 4.20 (b).

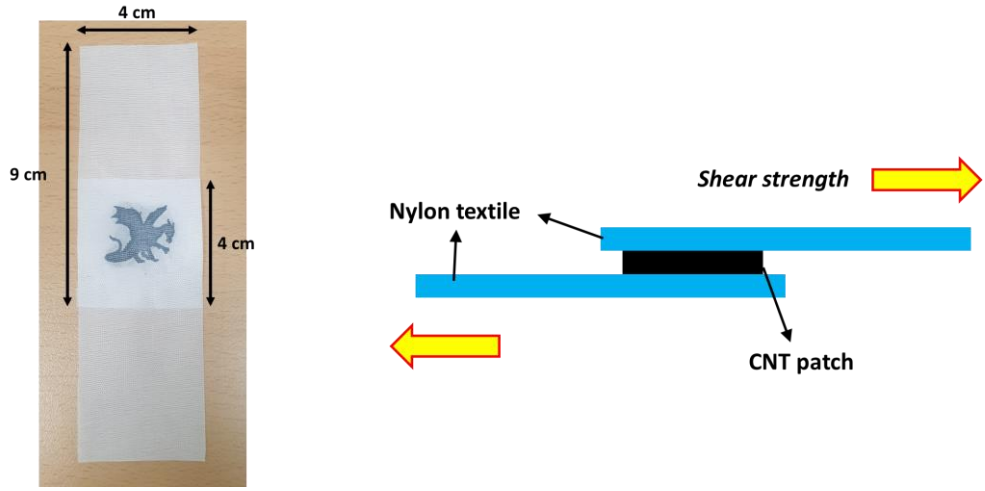


Figure 4.18. The sample of the CNT patch between the two nylon textiles for the lap shear strength test.

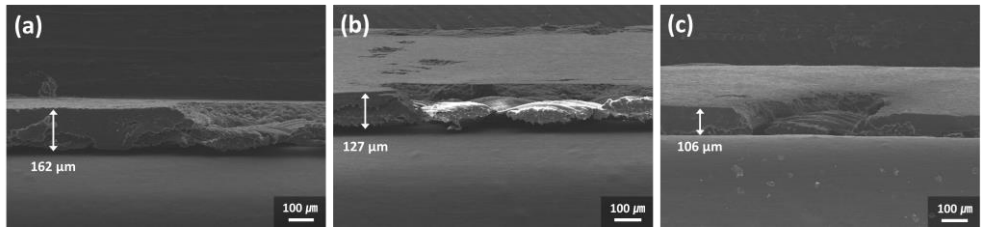


Figure 4.19. SEM cross-section of the pressed CNT patch attached textile. The pressure is (a) 5 kPa, (b) 20 kPa, and (c) 40 kPa.

It is noteworthy that it shows a different aspect from the sticker type above a certain pressure (about 20 kPa) and is named a print type. In the print type, since the adhesion between the patch and textile is greater than the cohesion of the CNT/paraffin composite, the patch cannot be peeled off without damaging the patch. Instead of losing detachable properties, the bending stability is increased due to the textile backbone supporting the patch from the inside. Figure 4.21 shows a bending test of printing type. 11,000 cycles of bending-relaxation were performed with a bending radius of 10 mm. During the bending test, the change in resistance was measured in two states, bending and relaxation. Although the resistance change in the bending state gradually increases due to the accumulation of stress in repeated bending, resistance change in the relaxation state improved compared to Figure 2.14 (the bending test of the CNT pattern printed on the PET film), and can endure even when folding as well.

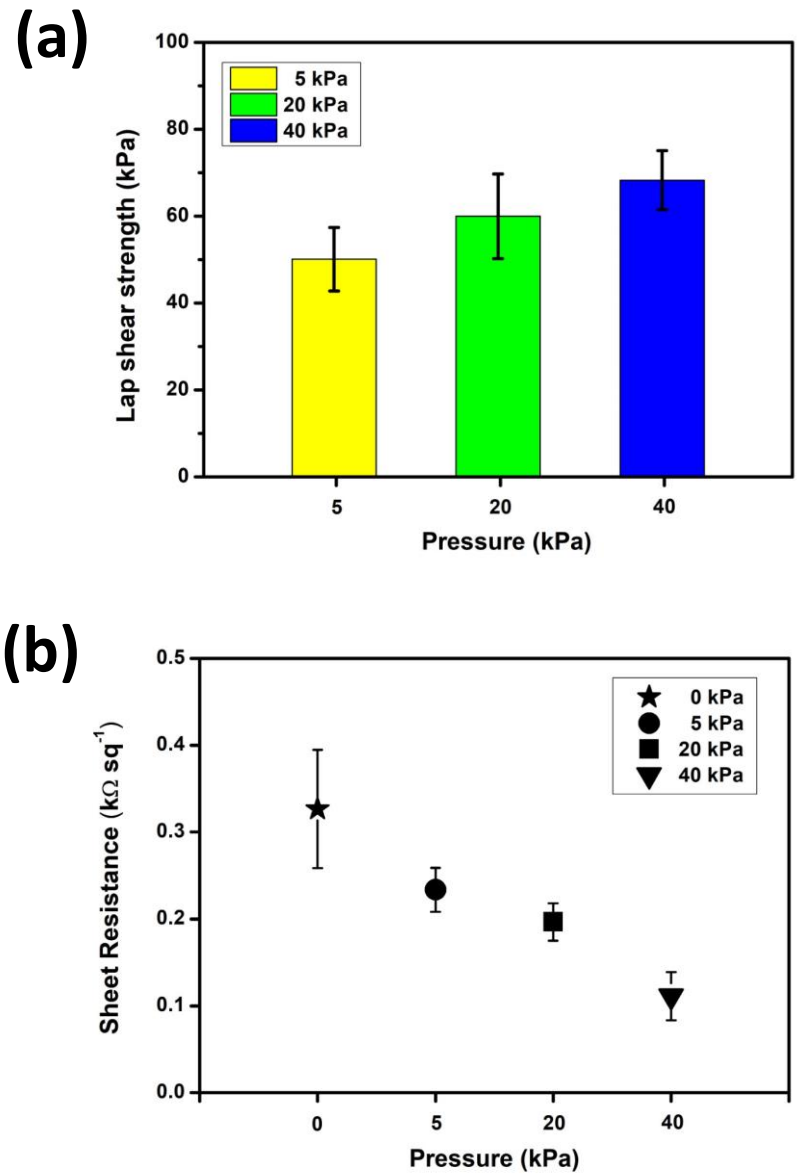


Figure 4.20. Property changing of CNT patch according to the various pressure.

(a) Lap shear strength and (b) sheet resistance of the CNT patch.

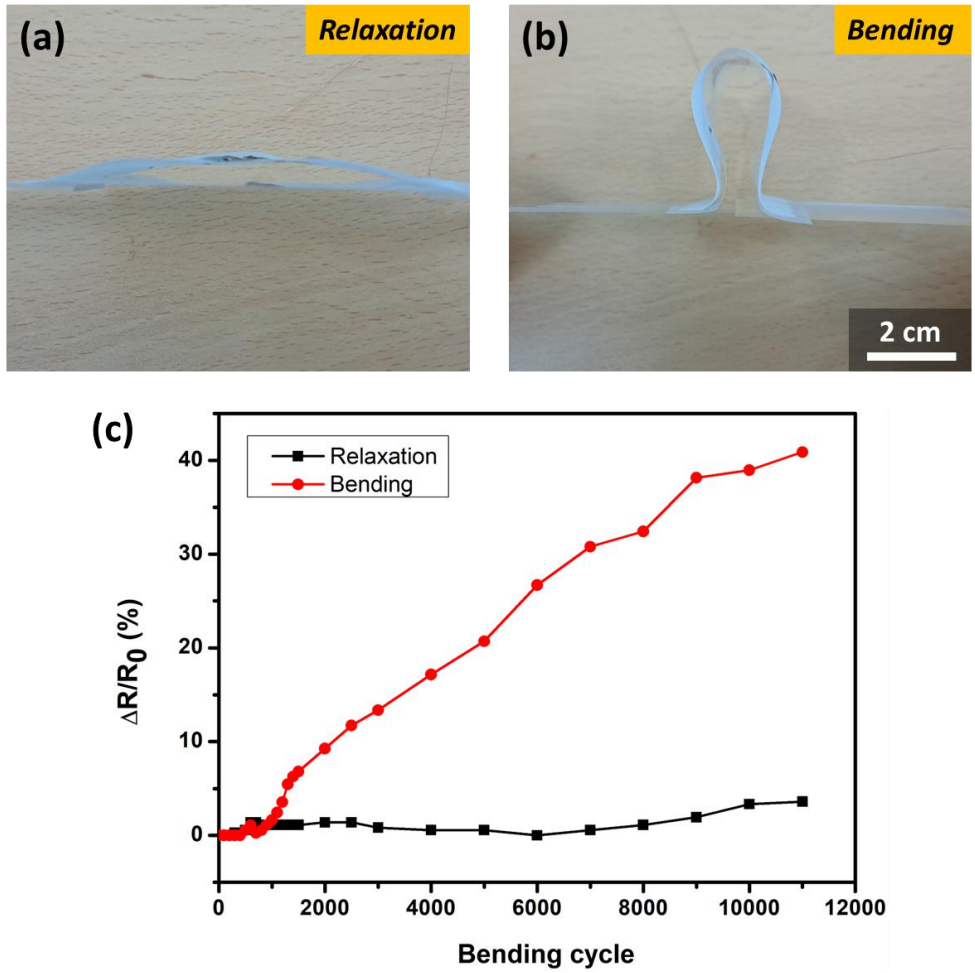


Figure 4.21. Bending test for the print mode of the nylon textile with CNT patch pressed at 40 kPa.

(a) Relaxation and (b) bending state of the nylon textile with CNT patch. The bending radius is 10 mm. (c) The graph of resistance change rate in the state of relaxation and bending according to the bending cycles.

CNT patches attached to textiles were applied to TENGs for applications in electronic textiles. Considering that it will be applied to a wearable device later, the structure of the single-electrode mode TENG was chosen, and the CNT patch was used as an electrode part of the TENG. Figure 4.22 shows the driving mechanism of single-electrode mode TENG using patch-attached textile. At this time, a PFA film was used as the counter material, and the output value was generated repeatedly by triboelectrification and electrostatic induction, as described in Chapter 4.2.1.

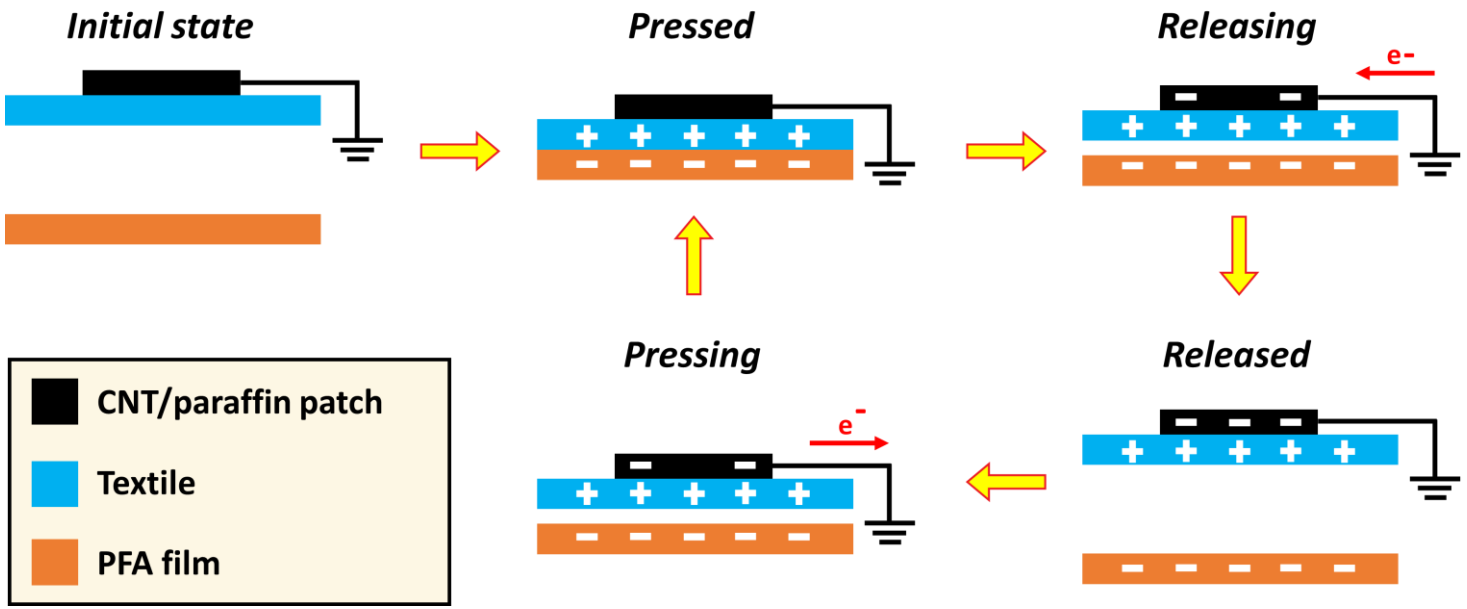


Figure 4.22. Mechanism of the TENG with CNT patch attached textile.

Figure 4.23 shows the output voltage of TENG according to the type of fabric. Cotton, polyester, and nylon fabrics with CNT patches were contacted and separated from the PFA film at 3 Hz and 0.15 N. Through the triboelectric series in Figure 4.14, it was expected that textiles with higher positive charge affinity would cause greater triboelectric output in contact with PFA film, which had very high negative charge affinity. As expected, the most significant output voltage was obtained in nylon textiles. In addition, various output values could be obtained by diversifying the contact force, like in Figure 4.24, and the stronger the force, the larger the value. The relationship between the contact force and the open-circuit voltage can be obtained from the following equation:[128]

$$V_{OC} = \frac{\left(\frac{F}{E'}\sqrt{\frac{\pi}{m_2}}\right)(\varphi_2 - \varphi_1)x}{3ex_0A}$$

where $F$ is the contact force, $E'$ is equivalent to elastic modulus, $m_2$ is a root mean square slope, $\varphi$ is the work function of the material, $x$ is separation distance, $e$ is the elementary charge, $x_0$ is critical separation distance, and $A$ is contact area, respectively. From this equation, it can be seen that the contact force affects the output value.

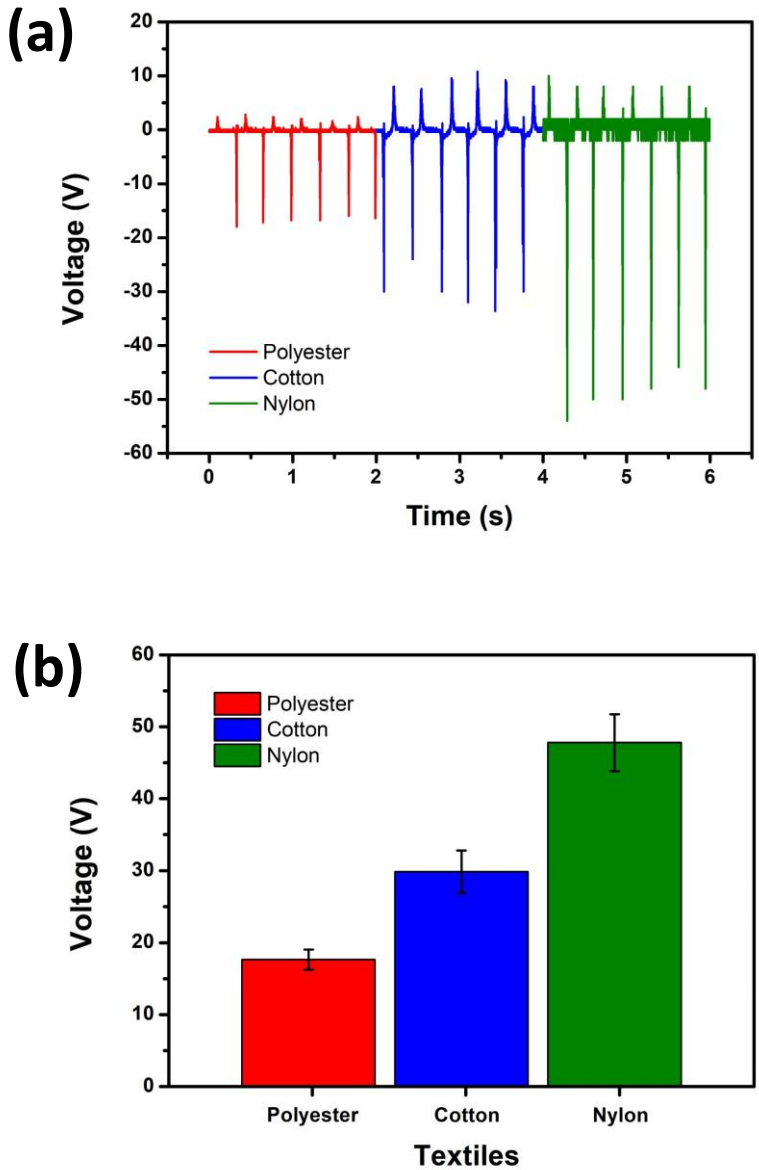


Figure 4.23. The graph of output voltage according to the fabric type at 3 Hz, 0.15 N.

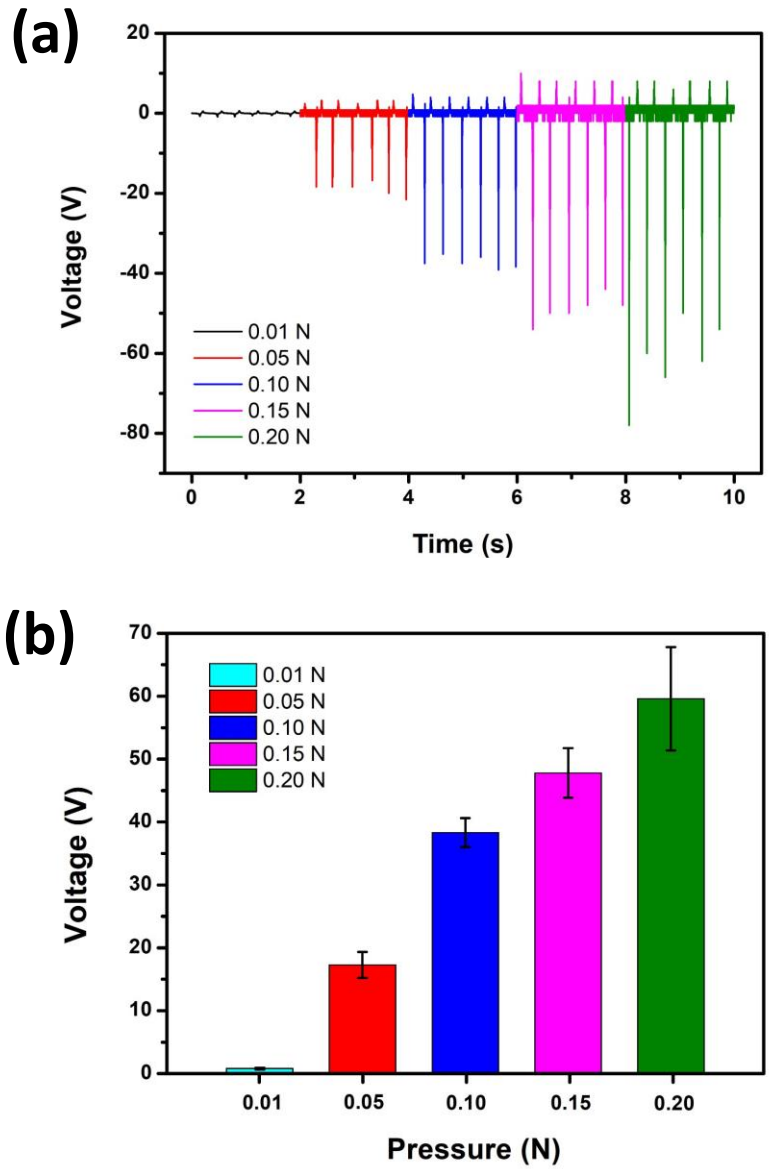


Figure 4.24. The graph of the output voltage of nylon textile with CNT patch according to the various contact force.

The effect on the area of CNT patches was also investigated. Other graphical patterns of the smaller area were prepared, which have a 107 $mm^2$, as shown in Figure 4.25. Figure 4.26 shows the output voltage according to the area of the CNT patch. Although the difference in area is more than twice, it can be seen that the output value rises slightly.

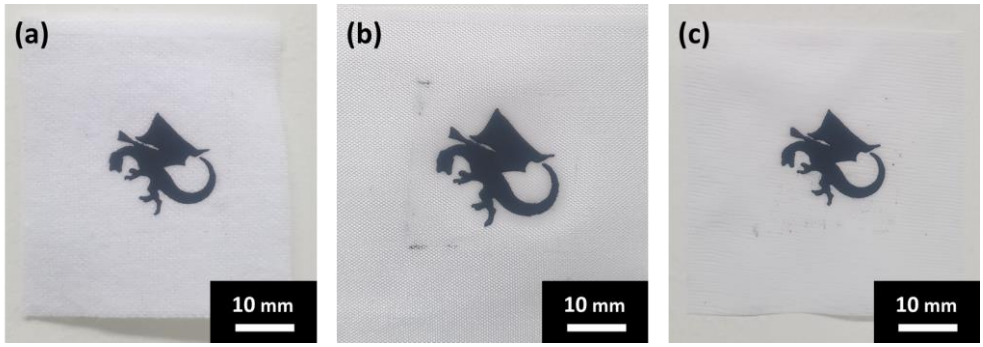


Figure 4.25. The smaller CNT/paraffin composite pattern (107 $mm^2$) printed on various textiles.

a) cotton, b) polyester, and c) nylon.

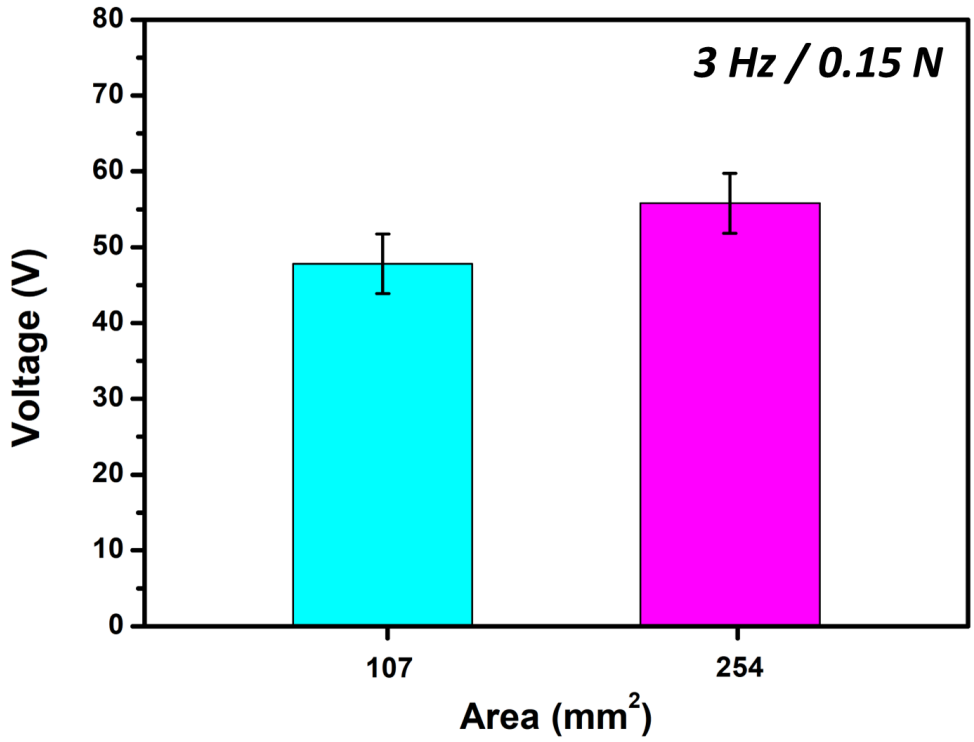


Figure 4.26. The output voltage of the CNT patch attached nylon textile according to the area of the CNT patch.

Previously, the performance of TENG was measured through friction with PFA film, but friction with the film is complex when considering actual use. Therefore, model friction with another textile was presented, such as in Figure 4.27 (a). At this time, the surface of the counter textile was coated using a commercial fluorine spray. The fluorine was sprayed on the textile for 3 s and heat-treated for 30 m on a hot plate at 120 °C. The gap in electron affinity with patch-attached textiles has been dramatically widened by functionalizing fluorine with high negative electron affinity on the surface. The graph of Figure 4.27 (b) shows the increased TENG output value by applying a commercial fluorine spray to the counter textile. This increase in the output shows the feasibility of implementing wearable electronics together with patches attached to commercial clothes, as shown in Figure 4.27 (c).

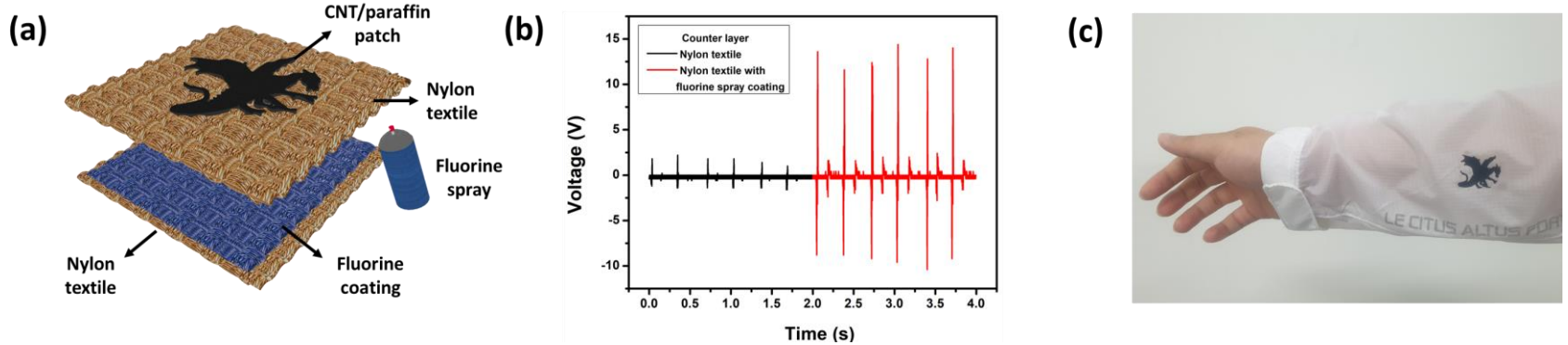


Figure 4.27. A model considering commercialization.

(a) Structure of TENG using fluorine spray. (b) The output voltage of the TENG according to the fluorine coating on the counter layer.

(c) CNT patch attached to the commercial cloth.

## 4.4. Summary

In this Chapter 4, various applications utilizing CNT/paraffin composite patterns were introduced. In particular, distinctive devices were implemented by utilizing the two advantages of the patterning method described above (i.e., high-resolution patterning and available a wide range of substrates).

The first application was a coplanar-type capacitive touch sensor. It was fabricated by printing a CNT/paraffin composite in an interdigitated pattern on PET film and then sealing it with PDMS. The sensor detected touch in both contact and non-contact modes by measuring the change in the electric field applied between the two electrodes. It was possible to increase the sensitivity of the touch sensor by reducing the electrode width and increasing the electrode number per area, which took advantage of the high-resolution patterning.

A miniaturized water-drop energy harvesting device was the subsequent application of the pattern. The interdigitated pattern was printed on a polymer film, and then a water droplet was dropped on the opposite side of the film where the electrode fingers were printed. It is of note in this application that the pattern was printed onto the FEP film, which has very low surface energy, by taking advantage of being able to print on a wide range of substrates. The FEP film has a very high negative electron affinity (15.1 mJ $m^{-2}$), so it induced a significant charge difference from friction with water droplets generating a

higher triboelectric output value than other films.

Lastly, utilizing the advantage of employing various substrates as above, the CNT/paraffin composite pattern was printed on fabric and applied as an electronic patch for wearable electronic devices. Adhesion was adjusted according to the pressure to press the patch so it could be used as a 'sticker type' or a 'print type'. CNT patches on the textile worked as an electrode for single-electrode mode TENG to produce electrical energy.

The versatility of CNT composite patterns is illustrated through various applications in this chapter. Each application could not only improve performance by using the advantages of this patterning method, but also have characteristics such as flexibility and thermal recovery. It directly suggests that this patterning method can contribute to the practical industrial applications of CNTs.

# Chapter 5. Conclusion

Since the discovery of CNTs, there have been many efforts to improve and commercialize them for about 30 years. Although it is an attractive material, the problems such as cost, mass, and uniform production have prevented the widespread adoption of CNT in industry, and difficulty in patterning is also one of the significant problems. For CNTs to be applied to electronic devices, they must be patternable, but existing CNT patterning methods suffer from many chronic problems. Conventional CNT patterning methods, divided mainly into photolithography combined approach and solvent dispersion, have problems such as being restricted by the substrate and long-time CNT pre-treatment, respectively.

This dissertation introduced a method for printing CNTs via soft-lithography by mixing them with paraffin to solve the problems of conventional methods. CNTs were mixed simply with molten paraffin to form slurry composites. The dispersion of CNTs in paraffin was easier than in organic solvents due to the molecular structure of paraffin decreasing the van der Waals force between CNTs. Also, the soft-lithography method can be employed because paraffin has low surface tension, and does not cause swelling of the elastic stamp, unlike organic solvents. In addition, since paraffin maintains its volume through a phase change, it is easy to use the μTM method, which is advantageous for expressing a high and bulky

structure that is difficult to use as a polymer composite.

Various tools analyzed CNT/paraffin composite: i) paraffin acts as a solvent and binder without chemical reaction with CNTs, ii) CNTs have clusters about several micrometers in paraffin, meaning the resolution limits of the patterning. iii) resistivity was 14.6 ± 2.8 Ω cm. iv) The CNT concentration of the composite material changes from 5 wt% to 15 wt% after the patterning process was not controllable, which is the drawback of this method.

On the other hand, the residues on the embossed part of the stamp and the difficulty of transferring the pattern from intaglio space to substrate, which are the two chronic problems of μTM, have to be solved inevitably. The pattern quality was increased by overcoming these problems through two additional processes, the 'paraffin cleaning process' and the 'minimize bending radius peeling method'. Consequently, the printed CNT patterns have two critical advantages enabling various applications that allow several micrometers of high-resolution CNT printing within a few minutes. They can print on a wide range of substrates, such as paper, leaves, and skins. In addition, it can achieve high-thickness patterns, bending durability, and heat recovery ability.

Furthermore, an experiment was conducted to use the pattern extensively to remove paraffin from the pattern. As the paraffin melts for as long as it is treated in hexane, and the CNT core is more exposed, it is thought to be more

advantageous for applications such as energy storage devices or electrochemical sensors that require interaction with CNTs. However, the removal of paraffin, which serves as a binder for CNTs, is accompanied by damage, such as pattern peeling off from the substrate; further research on stable paraffin removal is needed.

Lastly, patterned CNT/paraffin composite can be utilized in various applications such as capacitive touch sensors, water-drop energy harvesting devices, and e-textile for wearable electronics as an electrode. By utilizing the two advantages of high-resolution printing and diversity of substrates, the performance of applied devices was improved, and differentiated characteristics were demonstrated.

In this dissertation, CNTs are patterned quickly in a much simpler and cheaper way than the conventional methods and show versatility by being applied to various applications. It also can suggest a new paradigm for paraffin applications. Paraffin, which had limited use for some applications, such as energy storage, was used as an alternative to conventional solvents and polymers for CNT patterning. Furthermore, it may be possible to pattern nanowires of various materials with similar one-dimensional shapes and be used in various patterning methods since paraffin is advantageous for patterning. Finally, this soft-lithography-based CNT/paraffin composite printing method can be further developed with significant room for improvement in pattern and process, which is expected to contribute to the application of CNT in various fields.

# Bibliography


1. Madani, S. Y., Mandel, A. & Seifalian, A. M. A concise review of carbon nanotube's toxicology. *Nano Rev* **4**, 21521 (2013).
2. Iijima, S. Helical microtubles of graphitic carbon. *Nature* **354**, 56–58 (1991).
3. Mamedov, A. A. *et al.* Molecular design of strong single-wall carbon nanotube/polyelectrolyte multilayer composites. *Nat Mater* **1**, 190–194 (2002).
4. Javey, A., Wang, Q., Ural, A., Li, Y. & Dai, H. Carbon Nanotube Transistor Arrays for Multistage Complementary Logic and Ring Oscillators. *Nano Lett* **2**, 929–932 (2002).
5. Allen, B. L., Kichambare, P. D. & Star, A. Carbon nanotube field-effect-transistor-based biosensors. *Advanced Materials* **19**, 1439–1451 (2007).
6. Karousis, N., Tagmatarchis, N. & Tasis, D. Current progress on the chemical modification of carbon nanotubes. *Chem Rev* **110**, 5366–5397 (2010).
7. Arun, H. Advancements in the use of carbon nanotubes for antenna realization. *AEU - International Journal of Electronics and Communications* **136**, 153753 (2021).
8. Drissi-Habti, M., Assami, Y. el & Raman, V. Multiscale toughening of composites with carbon nanotubes—continuous multiscale reinforcement new concept. *Journal of Composites Science* **5**, 135 (2021).
9. Jiang, J. *et al.* CNT/Ni hybrid nanostructured arrays: Synthesis and application as high-performance electrode materials for pseudocapacitors. *Energy Environ Sci* **4**, 5000–5007 (2011).
10. Rowell, M. W. *et al.* Organic solar cells with carbon nanotube network electrodes. *Appl Phys Lett* **88**, 233506 (2006).
11. Tsai, T. Y., Lee, C. Y., Tai, N. H. & Tuan, W. H. Transfer of patterned vertically aligned carbon nanotubes onto plastic substrates for flexible electronics and field emission devices. *Appl Phys Lett* **95**, 013107 (2009).
12. Yang, D. *et al.* The π-π Stacking-guided supramolecular self-assembly of nanomedicine for effective delivery of antineoplastic therapies. *Nanomedicine* **13**, 3159–3177 (2018).

13. Zhuang, W. R. *et al.* Applications of π-π stacking interactions in the design of drug-delivery systems. *Journal of Controlled Release* **294**, 311–326 (2019).

14. Speight, J. G. Wax Deposition and Fouling. in *Fouling in Refineries* 155–173 (Elsevier, 2015).

15. Gunjo, D. G. *et al.* Performance of latent heat storage (LHS) systems using pure paraffin wax as working substance. *Case Studies in Thermal Engineering* **39**, 102399 (2022).

16. Halvaee, M. *et al.* Comparison of pristine and polyaniline-grafted MWCNTs as conductive sensor elements for phase change materials: Thermal conductivity trend analysis. *J Appl Polym Sci* **134**, 45389 (2017).

17. Han, L. *et al.* Effective Encapsulation of Paraffin Wax in Carbon Nanotube Agglomerates for a New Shape-Stabilized Phase Change Material with Enhanced Thermal-Storage Capacity and Stability. *Ind Eng Chem Res* **57**, 13026–13035 (2018).

18. Wang, J., Xie, H. & Xin, Z. Thermal properties of paraffin based composites containing multi-walled carbon nanotubes. *Thermochim Acta* **488**, 39–42 (2009).

19. Kumar, K., Sharma, K., Verma, S. & Upadhyay, N. Experimental Investigation of Graphene-Paraffin Wax Nanocomposites for Thermal Energy Storage. *Mater Today Proc* **18**, 5158–5163 (2019).

20. Xia, Y. & Whitesides, G. M. Soft Lithography. *Angewandte Chemie International Edition* **37**, 550–575 (1998).

21. Oren, S., Ceylan, H., Schnable, P. S. & Dong, L. High-Resolution Patterning and Transferring of Graphene-Based Nanomaterials onto Tape toward Roll-to-Roll Production of Tape-Based Wearable Sensors. *Adv Mater Technol* **2**, 1700223 (2017).

22. Hwang, J. K. *et al.* Direct nanoprinting by liquid-bridge-mediated nanotransfer moulding. *Nat Nanotechnol* **5**, 742–748 (2010).

23. Lee, J. H., Kim, C. H., Ho, K. M. & Constant, K. Two-polymer microtransfer molding for highly layered microstructures. *Advanced Materials* **17**, 2481–2485 (2005).

24. Li, Z. *et al.* Mass Transfer Printing of Metal-Halide Perovskite Films and Nanostructures. *Advanced Materials* **34**, 22003529 (2022).

25. Meitl, M. A. *et al.* Transfer printing by kinetic control of adhesion to an elastomeric stamp. *Nat Mater* **5**, 33–38 (2006).

26. Brown, H. R. THE ADHESION BETWEEN POLYMERS. *Annu.*

*Rev. Maler. Sci* **21**, 463–89 (1991).

27. Zhang, L. *et al.* Research progress of microtransfer printing technology for flexible electronic integrated manufacturing. *Micromachines* **12**, 1358 (2021).

28. Kim, T. H. *et al.* Full-colour quantum dot displays fabricated by transfer printing. *Nat Photonics* **5**, 176–182 (2011).

29. Cho, S., Kim, N., Song, K. & Lee, J. Adhesiveless Transfer Printing of Ultrathin Microscale Semiconductor Materials by Controlling the Bending Radius of an Elastomeric Stamp. *Langmuir* **32**, 7951–7957 (2016).

30. Lee, J. H. *et al.* A new method of carbon-nanotube patterning using reduction potentials. *Advanced Materials* **21**, 1257–1260 (2009).

31. Bui, M. P. N. *et al.* Electrochemical patterning of gold nanoparticles on transparent single-walled carbon nanotube films. *Chemical Communications* **37**, 5549–5551 (2009).

32. Han, K. N., Li, C. A., Bui, M. P. N. & Seong, G. H. Patterning of single-walled carbon nanotube films on flexible, transparent plastic substrates. *Langmuir* **26**, 598–602 (2010).

33. Jung, Y. J. *et al.* Aligned carbon nanotube-polymer hybrid architectures for diverse flexible electronic applications. *Nano Lett* **6**, 413–418 (2006).

34. Kholghi Eshkalak, S. *et al.* A review on inkjet printing of CNT composites for smart applications. *Appl Mater Today* **9**, 372–386 (2017).

35. Kim, D. & Yun, K. S. Patterning of carbon nanotube films on PDMS using SU-8 microstructures. *Microsystem Technologies* **19**, 743–748 (2013).

36. Kim, S. *et al.* Spin-and spray-deposited single-walled carbon-nanotube electrodes for organic solar cells. *Adv Funct Mater* **20**, 2310–2316 (2010).

37. Wang, L.-L. *et al.* Electromagnetic interference shielding effectiveness of carbon-based materials prepared by screen printing. *Carbon* **47**, 1905–1910 (2009).

38. Huang, Y. Y. & Terentjev, E. M. Dispersion of carbon nanotubes: Mixing, sonication, stabilization, and composite properties. *Polymers* **4**, 275–295 (2012).

39. Choi, J. H., Jegal, J. & Kim, W. N. Fabrication and characterization of multi-walled carbon nanotubes/polymer blend membranes. *J Memb*

*Sci* **284**, 406–415 (2006).

40. Chen, S. J. *et al.* Predicting the influence of ultrasonication energy on the reinforcing efficiency of carbon nanotubes. *Carbon* **77**, 1–10 (2014).

41. Lavagna, L., Nisticò, R., Musso, S. & Pavese, M. Functionalization as a way to enhance dispersion of carbon nanotubes in matrices: a review. *Mater Today Chem* **20**, 100477 (2021).

42. O'connell, M. J. *et al.* Reversible water-solubilization of single-walled carbon nanotubes by polymer wrapping. *Chem Phys Lett* **342**, 265–271 (2001).

43. Fredi, G., Dorigato, A., Fambri, L. & Pegoretti, A. Wax confinement with carbon nanotubes for phase changing epoxy blends. *Polymers* **9**, 405 (2017).

44. Rivadulla, F., Mateo-Mateo, C. & Correa-Duarte, M. A. Layer-by-layer polymer coating of carbon nanotubes: Tuning of electrical conductivity in random networks. *J Am Chem Soc* **132**, 3751–3755 (2010).

45. Yu, Z., Niu, X., Liu, Z. & Pei, Q. Intrinsically stretchable polymer light-emitting devices using carbon nanotube-polymer composite electrodes. *Advanced Materials* **23**, 3989–3994 (2011).

46. Luo, C. *et al.* Flexible carbon nanotube-polymer composite films with high conductivity and superhydrophobicity made by solution process. *Nano Lett* **8**, 4454–4458 (2008).

47. Liu, C. X. & Choi, J. W. Patterning conductive PDMS nanocomposite in an elastomer using microcontact printing. *Journal of Micromechanics and Microengineering* **19**, 085019 (2009).

48. Ogihara, H., Kibayashi, H. & Saji, T. Microcontact printing for patterning carbon nanotube/polymer composite films with electrical conductivity. *ACS Appl Mater Interfaces* **4**, 4891–4897 (2012).

49. Miyako, E., Nagata, H., Hirano, K. & Hirotsu, T. Carbon nanotube-polymer composite for light-driven microthermal control. *Angewandte Chemie - International Edition* **47**, 3610–3613 (2008).

50. Deng, J. *et al.* Tunable Photothermal Actuators Based on a Pre-programmed Aligned Nanostructure. *J Am Chem Soc* **138**, 225–230 (2016).

51. Joo, S. *et al.* Intaglio Contact Printing of Versatile Carbon Nanotube Composites and Its Applications for Miniaturizing High-Performance Devices. *Small* **18**, 2106174 (2022).

52. Lu, Q. *et al.* Determination of carbon nanotube density by gradient sedimentation. *Journal of Physical Chemistry B* **110**, 24371–24376 (2006).

53. Rao, Z. H. & Zhang, G. Q. Thermal properties of paraffin wax-based composites containing graphite. *Energy Sources, Part A: Recovery, Utilization and Environmental Effects* **33**, 587–593 (2011).

54. Yang, W. *et al.* Novel segregated-structure phase change materials composed of paraffin@graphene microencapsules with high latent heat and thermal conductivity. *J Mater Sci* **53**, 2566–2575 (2018).

55. Zhao, Y. *et al.* Self-assembly of carbon nanotubes in polymer melts: Simulation of structural and electrical behaviour by hybrid particle-field molecular dynamics. *Nanoscale* **8**, 15538–15552 (2016).

56. Daniel, J. & Rajasekharan, R. Organogelation of plant oils and hydrocarbons by long-chain saturated FA, fatty alcohols, wax esters, and dicarboxylic acids. *JAOCS, Journal of the American Oil Chemists' Society* **80**, 417–421 (2003).

57. Liu, W. W., Xia, B. Y., Wang, X. X. & Wang, J. N. Exfoliation and dispersion of graphene in ethanol-water mixtures. *Front Mater Sci* **6**, 176–182 (2012).

58. Jańczuk, B. & Tomasz, B. Surface Free-Energy Components of Liquids and Low Energy Solids and Contact Angles. *J Colloid Interface Sci* **127**, 189–204 (1989).

59. Lee, S., Park, J. S. & Lee, T. R. Analysis of the wettability of partially fluorinated polymers reveals the surprisingly strong acid-base character of poly(vinylidene fluoride). *Bull Korean Chem Soc* **32**, 41–48 (2011).

60. Hong, J. S. & Kim, C. Dispersion of multi-walled carbon nanotubes in PDMS/PB blend. *Rheol Acta* **50**, 955–964 (2011).

61. Ho, C. C. & Khew, M. C. Surface free energy analysis of natural and modified natural rubber latex films by contact angle method. *Langmuir* **16**, 1407–1414 (2000).

62. Toraman, M. C. Effects of Leaf Surface Energy on Pesticidal Performance. *J Agric Sci* **25**, 174–180 (2019).

63. Norhanifah, M. Y., Rohani, A. B., Asrul, M. & Amir Hashim, M. Y. Investigating High Ammonia NR Latex Concentrate Based Stationary Adhesive Formulation. *Malaysian Journal of Chemistry* **20**, 188–195 (2018).

64. Roh, S. C., Choi, E. Y., Choi, Y. S. & Kim, C. K. Characterization of the surface energies of functionalized multi-walled carbon nanotubes

and their interfacial adhesion energies with various polymers. *Polymer* **55**, 1527–1536 (2014).

65. Weng, S. C., Fuh, A. Y. G., Tang, F. C. & Cheng, K. T. Effect of surface condition on liquid crystal photoalignment by light-induced azo dye adsorption phenomena. *Liq Cryst* **43**, 1221–1229 (2016).

66. Owolabi, T. O., Akande, K. O. & Sunday, O. O. Modeling of average surface energy estimator using computational intelligence technique. *Multidiscipline Modeling in Materials and Structures* **11**, 284–296 (2015).

67. Tao, Z. *et al.* Physical model test study on shear strength characteristics of slope sliding surface in Nanfen open-pit mine. *Int J Min Sci Technol* **30**, 421–429 (2020).

68. Nurazzi, N. M. *et al.* Mechanical performance and applications of cnts reinforced polymer composites—a review. *Nanomaterials* **11**, 2186 (2021).

69. Lee, H. *et al.* A stretchable polymer-carbon nanotube composite electrode for flexible lithium-ion batteries: Porosity engineering by controlled phase separation. *Adv Energy Mater* **2**, 976–982 (2012).

70. Light, T. S., Licht, S., Bevilacqua, A. C. & Morash, K. R. The fundamental conductivity and resistivity of water. *Electrochemical and Solid-State Letters* **8**, E16–E19 (2005).

71. Wen, Z. *et al.* Self-powered textile for Wearable electronics by hybridizing fiber-shaped nanogenerators, solar cells, and supercapacitors. *Sci Adv* **2**, e1600097 (2016).

72. Zang, Y., Zhang, F., Di, C. A. & Zhu, D. Advances of flexible pressure sensors toward artificial intelligence and health care applications. *Mater Horiz* **2**, 140–156 (2015).

73. Garcia, C., Trendafilova, I., Guzman de Villoria, R. & Sanchez del Rio, J. Self-powered pressure sensor based on the triboelectric effect and its analysis using dynamic mechanical analysis. *Nano Energy* **50**, 401–409 (2018).

74. Adler, R. & Desmares, P. J. An Economical Touch Panel Using SAW Absorpbtion. *IEEE Trans Ultrason Ferroelectr Freq Control* **34**, 195–201 (1987).

75. Bae, S. H. *et al.* 14.4: Integrating Multi-Touch Function with a Large-Sized LCD. *SID Symposium Digest of Technical Papers* **39**, 178 (2008).

76. Kang, M. *et al.* Graphene-Based Three-Dimensional Capacitive Touch Sensor for Wearable Electronics. *ACS Nano* **11**, 7950–7957

(2017).

77. Kim, S. *et al.* A highly sensitive capacitive touch sensor integrated on a thin-film-encapsulated active-matrix OLED for ultrathin displays. *IEEE Trans Electron Devices* **58**, 3609–3615 (2011).

78. Ruth, S. R. A. *et al.* Flexible Fringe Effect Capacitive Sensors with Simultaneous High-Performance Contact and Non-Contact Sensing Capabilities. *Small Struct* **2**, 2000079 (2021).

79. Kim, M. G. *et al.* All-soft, battery-free, and wireless chemical sensing platform based on liquid metal for liquid- and gas-phase VOC detection. *Lab Chip* **17**, 2323–2329 (2017).

80. Mrozik, W., Rajaeifar, M. A., Heidrich, O. & Christensen, P. Environmental impacts, pollution sources and pathways of spent lithium-ion batteries. *Energy Environ Sci* **14**, 6099–6121 (2021).

81. Melin, H. E. *et al.* Global implications of the EU battery regulation. *Science* **373**, 384–387 (2021).

82. Ronco, C., Davenport, A. & Gura, V. A wearable artificial kidney: Dream or reality? *Nat Clin Pract Nephrol* **4**, 604–605 (2008).

83. Wang, C. *et al.* High dielectric barium titanate porous scaffold for efficient Li metal cycling in anode-free cells. *Nat Commun* **12**, 6536 (2021).

84. Fan, F. R., Tian, Z. Q. & Lin Wang, Z. Flexible triboelectric generator. *Nano Energy* **1**, 328–334 (2012).

85. Zhang, X. *et al.* Harvesting Multidirectional Breeze Energy and Self-Powered Intelligent Fire Detection Systems Based on Triboelectric Nanogenerator and Fluid-Dynamic Modeling. *Adv Funct Mater* **31**, 2106527 (2021).

86. Han, Y. *et al.* Fish Gelatin Based Triboelectric Nanogenerator for Harvesting Biomechanical Energy and Self-Powered Sensing of Human Physiological Signals. *ACS Appl Mater Interfaces* **12**, 16442–16450 (2020).

87. Shaukat, R. A., Saqib, Q. M., Khan, M. U., Chougale, M. Y. & Bae, J. Bio-waste sunflower husks powder based recycled triboelectric nanogenerator for energy harvesting. *Energy Reports* **7**, 724–731 (2021).

88. Sukumaran, C. *et al.* Triboelectric nanogenerators from reused plastic: An approach for vehicle security alarming and tire motion monitoring in rover. *Appl Mater Today* **19**, 100625 (2020).

89. Li, M. *et al.* Deformable, resilient, and mechanically-durable

triboelectric nanogenerator based on recycled coffee waste for wearable power and self-powered smart sensors. *Nano Energy* **79**, 105405 (2021).

90. Fu, J., Xia, K. & Xu, Z. A triboelectric nanogenerator based on human fingernail to harvest and sense body energy. *Microelectron Eng* **232**, 111408 (2020).

91. Khandelwal, G. *et al.* All edible materials derived biocompatible and biodegradable triboelectric nanogenerator. *Nano Energy* **65**, 104016 (2019).

92. Zheng, Q. *et al.* Biodegradable triboelectric nanogenerator as a life-time designed implantable power source. *Sci Adv* **2**, e1501478 (2016).

93. Singh, H. H., Kumar, D. & Khare, N. Tuning the performance of ferroelectric polymer-based triboelectric nanogenerator. *Appl Phys Lett* **119**, 053901 (2021).

94. Kim, Y. J. *et al.* Effect of the relative permittivity of oxides on the performance of triboelectric nanogenerators. *RSC Adv* **7**, 49368–49373 (2017).

95. Chen, J. & Wang, Z. L. Reviving Vibration Energy Harvesting and Self-Powered Sensing by a Triboelectric Nanogenerator. *Joule* **1**, 480–521 (2017).

96. Byun, K. E. *et al.* Control of Triboelectrification by Engineering Surface Dipole and Surface Electronic State. *ACS Appl Mater Interfaces* **8**, 18519–18525 (2016).

97. Miao, Q. *et al.* Toward self-powered inertial sensors enabled by triboelectric effect. *ACS Appl Electron Mater* **2**, 3072–3087 (2020).

98. Chen, A., Zhang, C., Zhu, G. & Wang, Z. L. Polymer Materials for High-Performance Triboelectric Nanogenerators. *Advanced Science* **7**, 2000186 (2020).

99. Choi, D. *et al.* Spontaneous electrical charging of droplets by conventional pipetting. *Sci Rep* **3**, 2037 (2013).

100. Wang, Z. L. Triboelectric nanogenerators as new energy technology and self-powered sensors - Principles, problems and perspectives. *Faraday Discuss* **176**, 447–458 (2014).

101. Kil Yun, B., Soo Kim, H., Joon Ko, Y., Murillo, G. & Hoon Jung, J. Interdigital electrode based triboelectric nanogenerator for effective energy harvesting from water. *Nano Energy* **36**, 233–240 (2017).

102. Jang, S. *et al.* Monocharged electret based liquid-solid interacting triboelectric nanogenerator for its boosted electrical output

performance. *Nano Energy* **70**, 104541 (2020).

103. Su, Y. *et al.* Hybrid triboelectric nanogenerator for harvesting water wave energy and as a self-powered distress signal emitter. *Nano Energy* **9**, 186–195 (2014).

104. Du, K. *et al.* Electronic textiles for energy, sensing, and communication. *iScience* **25**, 104174 (2022).

105. Wang, W., Yu, A., Zhai, J. & Wang, Z. L. Recent Progress of Functional Fiber and Textile Triboelectric Nanogenerators: Towards Electricity Power Generation and Intelligent Sensing. *Advanced Fiber Materials* **3**, 394–412 (2021).

106. Zhang, J. wen, Zhang, Y., Li, Y. yuan & Wang, P. Textile-Based Flexible Pressure Sensors: A Review. *Polymer Reviews* **62**, 65–94 (2022).

107. Shahood uz, Z., Tao, X., Cochrane, C. & Koncar, V. Smart E-Textile Systems: A Review for Healthcare Applications. *Electronics* **11**, 99 (2021).

108. Yang, Z. *et al.* Strain-Durable High-Conductivity Nylon-6 Fiber with 1D Nanomaterial Lamellar Cladding for Massive Production. *ACS Appl Mater Interfaces* **13**, 57759–57767 (2021).

109. Wu, R. *et al.* Silk Composite Electronic Textile Sensor for High Space Precision 2D Combo Temperature–Pressure Sensing. *Small* **15**, 1901558 (2019).

110. Ryu, C. H. *et al.* Wearable Piezoelectric Yarns with Inner Electrodes for Energy Harvesting and Signal Sensing. *Adv Mater Technol* **7**, 2101138 (2022).

111. Nechyporchuk, O., Bordes, R. & Köhnke, T. Wet Spinning of Flame-Retardant Cellulosic Fibers Supported by Interfacial Complexation of Cellulose Nanofibrils with Silica Nanoparticles. *ACS Appl Mater Interfaces* **9**, 39069–39077 (2017).

112. Ding, Y., Xu, W., Wang, W., Fong, H. & Zhu, Z. Scalable and Facile Preparation of Highly Stretchable Electrospun PEDOT:PSS@PU Fibrous Nonwovens toward Wearable Conductive Textile Applications. *ACS Appl Mater Interfaces* **9**, 30014–30023 (2017).

113. He, H. *et al.* An Ultralight Self-Powered Fire Alarm e-Textile Based on Conductive Aerogel Fiber with Repeatable Temperature Monitoring Performance Used in Firefighting Clothing. *ACS Nano* **16**, 2953–2967 (2022).

114. Castano, L. M. & Flatau, A. B. Smart fabric sensors and e-textile technologies: A review. *Smart Mater Struct* **23**, 053001 (2014).

115. Zhang, W. *et al.* Textile carbon network with enhanced areal capacitance prepared by chemical activation of cotton cloth. *J Colloid Interface Sci* **553**, 705–712 (2019).

116. Cho, G., Jeong, K., Paik, M. J., Kwun, Y. & Sung, M. Performance evaluation of textile-based electrodes and motion sensors for smart clothing. *IEEE Sens J* **11**, 3183–3193 (2011).

117. Lim, T., Zhang, H. & Lee, S. Gold and silver nanocomposite-based biostable and biocompatible electronic textile for wearable electromyographic biosensors. *APL Mater* **9**, 091113 (2021).

118. Ma, X. *et al.* Highly Permeable and Ultrastretchable Liquid Metal Micromesh for Skin-Attachable Electronics. *ACS Mater Lett* **4**, 634–641 (2022).

119. Shahariar, H., Kim, I., Soewardiman, H. & Jur, J. S. Inkjet Printing of Reactive Silver Ink on Textiles. *ACS Appl Mater Interfaces* **11**, 6208–6216 (2019).

120. Karim, N. *et al.* All inkjet-printed graphene-based conductive patterns for wearable e-textile applications. *J Mater Chem C Mater* **5**, 11640–11648 (2017).

121. Buechley, L. & Eisenberg, M. Fabric PCBs, electronic sequins, and socket buttons: Techniques for e-textile craft. *Pers Ubiquitous Comput* **13**, 133–150 (2009).

122. Yoon, J. *et al.* Robust and stretchable indium gallium zinc oxide-based electronic textiles formed by cilia-assisted transfer printing. *Nat Commun* **7**, 11477 (2016).

123. Li, B. M. *et al.* Iron-on carbon nanotube (CNT) thin films for biosensing E-Textile applications. *Carbon* **168**, 673–683 (2020).

124. Uzun, S. *et al.* Knittable and Washable Multifunctional MXene-Coated Cellulose Yarns. *Adv Funct Mater* **29**, 1905015 (2019).

125. Ojuroye, O., Torah, R. & Beeby, S. Modified PDMS packaging of sensory e-textile circuit microsystems for improved robustness with washing. *Microsystem Technologies* **28**, 1467–1484 (2022).

126. Ding, W., Wang, A. C., Wu, C., Guo, H. & Wang, Z. L. Human–Machine Interfacing Enabled by Triboelectric Nanogenerators and Tribotronics. *Adv Mater Technol* **4**, 1800487 (2019).

127. Guo, R. *et al.* Semi-Liquid-Metal-(Ni-EGaIn)-Based Ultraconformable Electronic Tattoo. *Adv Mater Technol* **4**, 1900183 (2019).

128. Vasandani, P., Mao, Z. H., Jia, W. & Sun, M. Relationship between

triboelectric charge and contact force for two triboelectric layers. *J Electrostat* **90**, 147–152 (2017).

# 국문 초록

탄소나노튜브는 높은 전기 전도도 및 기계적 강도 등의 우수한 특성들을 가진 유망한 전자 재료이다. 따라서, 탄소나노튜브를 여러 분야에 적용하기 위한 상용화 연구가 활발히 진행중이다. 하지만 이러한 우수한 물성과 노력에도 불구하고 탄소나노튜브의 상용화는 더딘데, 그 이유 중 하나로 패턴화의 어려움을 들 수 있다. 이를 극복하기 위해, 탄소나노튜브를 패터닝하는 다양한 방법들이 개발되어 왔으며, 이를 이용하여 소자를 구현하는 많은 연구들이 보고되고 있다.

본 학위 논문은 탄소나노튜브 패터닝 방법의 개발과 응용에 대해 다루고 있다. 개발된 패터닝 방법은 기존 방식의 문제점들을 해결할 뿐만 아니라 차별화된 장점을 가지고 있다. 이를 위해서 탄소나노튜브를 유기물인 파라핀과 혼합하여 탄소나노튜브 복합체를 제조하였으며, 소프트 리소그래피 기술을 통해 패터닝하였다.

첫 번째 장에서는 탄소나노튜브와 파라핀 두 물질의 배경과 본 연구에서의 의의를 설명하며, 사용된 패터닝 방법인 소프트 리소그래피 및 관련 기술에 대해서도 설명한다. 더 나아가, 기존의 탄소나노튜브 패터닝 방법을 소개함과 동시에 해결해야 할 문제점을 설명하고 향후 탄소나노튜브 패터닝의 방향을 제시한다.

두 번째 장에서는 탄소나노튜브의 패터닝 방법과 결과를 자세히 보여준다. 파라핀과 소프트 리소그래피의 사용은 비용 및 접근성을 우수하게 할 뿐만 아니라 공정과 패턴의 특성 면에서 여러 이점들을 제공한다. 특히, 여러가지

장점들 중 가장 중요한 두 가지는 고해상도(<10 μm)의 패터닝이 가능하다는 것과 다양한 종류의 기판에 인쇄될 수 있다는 것이다. 이 외에도 광학적, 전기적, 열적, 기계적 분석 등을 통해 탄소나노튜브 복합체 패턴의 다양한 특성들을 소개한다.

한편, 패턴에 남아있는 탄소나노튜브 잔류물 및 파라핀은 회로 단락과 같은 부정적인 결과를 초래할 수 있다. 뿐만 아니라, 표면 에너지가 매우 낮은 기판에서는 전사 공정이 어려울 수도 있다. 따라서, 세 번째 장에서는 패턴과 공정과정에서 발생하는 이러한 문제들에 대해 논의하고, 탄소나노튜브 패턴의 품질 및 특성을 개선하기 위한 추가 프로세스에 대해 기술한다.

마지막으로 인쇄된 탄소나노튜브 복합체 패턴을 이용하여 고성능의 유연하고 소형화된 터치 센서와 에너지 하베스팅 소자를 제작하였다. 앞서 기술한 고해상도의 패터닝이 가능하다는 것과 기판에 제약이 없다는 두 장점을 활용하여 우수한 성능의 소자들을 제작할 수 있었다. 이는 탄소나노튜브 복합체 패턴이 다양한 분야에 적용될 수 있으며, 탄소나노튜브의 상업화에 기여할 수 있는 가능성을 시사한다. 소자의 제작 및 결과는 마지막 장에서 소개될 것이다.

**학번: 2019-39958**